Technischen Universität München
Munich School of Engineering (MSE)

Multi physics simulation with high temporal range reveals new aspects of laser ablation

Jürgen Sotrop

Vollständiger Abdruck der von der promotionsführenden Einrichtung Munich School of Engineering (MSE) der Technischen Universität München zur Erlangung des akademischen Grades eines

Doktor-Ingenieurs (Dr.-Ing.)

genehmigten Dissertation.

Vorsitzender: Prof. Dr. Michael Drews

Prüfende der Dissertation:

1. Prof. Dr. Paolo Lugli
2. Prof. Dr. Thomas Hamacher

Die Dissertation wurde am 09.04.2020 bei der Technischen Universität München eingereicht und durch die promotionsführenden Einrichtung Munich School of Engineering (MSE) am 13.11.2020 angenommen.

Preliminary Remark

The present dissertation is mainly composed on two peer-reviewed accepted first author publications by the doctoral candidate (No 6. and 7.). Most of the data have already been presented in this journal papers, and unavoidable overlap between the published texts and this dissertation appears.

1. Jan Winter, Jürgen Sotrop, Stephan Borek, Heinz P. Huber, Jan Minar, "Temperature-dependent determination of electron heat capacity and electron-phonon coupling factor for $Fe_{0.72}Cr_{0.18}Ni_{0.1}$." *Phys. Rev. B.* 93, 16 (2016)

2. Jürgen Sotrop, Jan Winter, Stephan Rapp, Heinz P. Huber, "Understanding of laser ablation efficiency." *SPIE Newsroom.* DOI: 10.1117/2.1201508.006004 (2015)

3. Matthias Domke, Jürgen Sotrop, Stephan Rapp, Max Börger, Dominik Felsl, Heinz P. Huber, "Transient temperature modeling and shock wave observation in confined laser ablation of thin molybdenum films." *Proc. of SPIE* 8611 86111B-1 (2015)

4. Matthias Domke, Luigi Nobile, Stephan Rapp, Sasia Eiselen, Jürgen Sotrop, Heinz P. Huber, Michael Schmidt, "Evidence of pressure waves in confined laser ablation." *JLMN* 10, 2 (2015)

5. Matthias Domke, Luigi Nobile, Stephan Rapp, Sasia Eiselen, Jürgen Sotrop, Heinz P. Huber, Michael Schmidt, "Understanding thin film laser ablation: The role of the effective penetration depth and the film thickness." *Phys. Proc.* 56, 1007 - 1014 (2014)

6. Jürgen Sotrop, Matthias Domke, Alfred Kersch, Heinz P. Huber, "Simulation of the melting volume in thin molybdenum films as a function of the laser pulse duration." *Proc. of SPIE*, 41 520 - 523 (2013)

7. Jürgen Sotrop, Alfred Kersch, Matthias Domke, Gerhard Heise, Heinz P. Huber, "Numerical simulation of ultrafast expansion as the driving mechanism for confined laser ablation with ultra-short laser pulses." *Appl. Phys. A* 113, 2 (2013)

8. Gerhard Heise, Matthias Domke, Jan Konrad, Sebastian Sarrach, Jürgen Sotrop, Heinz P. Huber, "Laser lift-off initiated by direct induced ablation of different metal thin films with ultra short laser pulses." *J. Phys. D: Applied Physics* 45, 315303, (2012)

9. Gerhard Heise, Jan Konrad, Sebastian Sarrach, Jürgen Sotrop, Heinz P. Huber, "Directly induced ablation of metal thin films by ultrashort laser pulses." *Frontiers in Ultrafast Optics: Biomedical, Scientific, and Industrial Applications XI*, pp. 792511-1 - 792511-8, (2011)

Contents

Abstract

Ultra short laser ablation is a common technique for material processing of metal thin films on transparent substrate. Recently, a so-called "confined" laser ablation effect has been reported, where an ultra-short laser pulse (pulse duration 660 fs and wave length 1053 nm) irradiates onto a thin molybdenum (Mo) film through a transparent glass substrate, resulting in a "lift-off" of the irradiated layer in form of a thin, solid, cylindrical fragment. This effect provides a new and very energy-efficient selective structuring process for the Mo-back electrode in thin-film solar cell production. The aim of this study was to create a finite element method (FEM) simulation model to investigate the underlying mechanism of the confined laser ablation of a thin Mo-film coated on a transparent glass substrate by backside irradiation with an ultra short laser pulse. The 3D axisymmetric FEM model consists of a volume absorption for the laser pulse, a two-temperature model approach for heat diffusion in the electron and the lattice subsystem and a thermo-mechanical expansion part, which includes the expansion in the solid as well as the expansion during the phase transition of melting and evaporation. The time frame of the model ranges from the femtosecond to the microsecond regime to precisely include the involving physical mechanisms, which appear on the different time scales. The simulation reveals that irradiation of the Mo-layer with an ultra-short laser pulse causes a rapid acceleration in the direction of the surface normal within a time frame of a hundred picoseconds to a peak velocity of about 100 m/s. Then, the molybdenum layer continues to move as an oscillating membrane, and finally forms a dome after about 100 ns. The calculated strain at the edges of the dome exceeds the tensile stress limit at fluences that initiate the "lift-off" in experimental investigations. In conclusion, the simulation reveals that the driving mechanism of the "lift-off" with ultra short laser pulses is the ultra-fast expansion of the interface layer and not the generated gas pressure, which is considered to be the driving force of the "lift-off" with short laser pulses.

The model is further applied for an investigation to study the melting and vapor volume over a wide range of pulse durations from 5 fs to 100 ps. It turns out, that the maximum vapor volume is reached at a pulse duration between 10 ps to 50 ps. The results provided compelling evidence, that the electron heat transfer is predominant for the ultra-short pulse regime below 10 ps to 50 ps, while the lattice heat transfer is outbalanced for longer pulse durations. Thus, by considering the vapor volume as the ablated domain, it is supposed that an effective pulse duration exists where the heat conduction of electrons and lattice is balanced, such that the vapor volume can be maximized.

1. Introduction

1.1. Motivation

Laser material processing exceptionally with ultra-short laser pulses has enabled new possibilities of material removal and modification. The spectrum of processable materials ranges from metals, semiconductors to insolaters. Beside bulk materials, even film systems of different materials can be applied to this method. Over the last two decades the exploration of the mechanisms behind these technological laser processes has attracted increasingly interest.[1–12] Ultra short pulse laser ablation is also one of the most powerful patterning technique for thin film material processing. This method has the potential of a highly selective structuring process for a broad range of thin film materials with low thermal damage of the surrounding area.[13–15] Therefore, also raising attention has been payed in the recent years for the application of ultra short laser pulses to the processing of Copper Indium Gallium Diselenid (CIGS/CIS) thin film solar cells. Here, the major issues are the increasing of the efficiency, costs reduction and high speed production.[16] Promessing results has been shown to the patterning of the monolithic serial interconnection which divides the solar cell into sub cells to reduce ohmic losses and increase the voltage.[17–19] Three different process steps has to be performed which are labeled by P1 (pattern 1), P2 (pattern 2), and P3 (pattern 3), shown in figure 1.1.[20] Besides the P2 and P3 which are the selective opening of the active CIS layer and the galvanic separation of the ZnO front p-contact, respectively, the P1 is of special interest which is the galvanic separation of the Mo back n-contact.

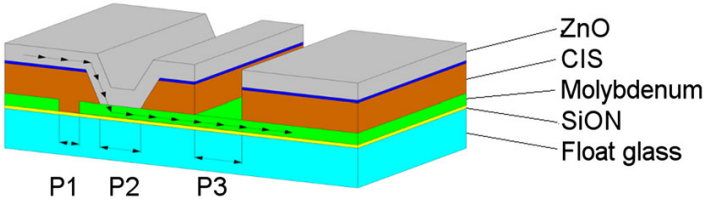

Figure 1.1.: Schematic cross section of a CIGS thin film solar cell. The monolithic serial interconnection is performed by three differnet process steps, which are labeled as P1, P2 and P3. The arrows are indicating the electron pathway through the solar cell structure. (Picture and caption obtained from Heise et. al[20]).

The state of the art monolithic serial interconnection of the Mo p-contact is produced by galvanic separation of the layer with means of direct irradiation by a nanosecond pulsed laser.[12,20] However this process shows thermal damage in form of burr formation and micro cracks of the surrounded material. Even by irradiating the layer directly with picosecond laser pulses the thin film material is still affected by thermal defects.[16] One way of eliminating these thermal side effects is enabled by a confined laser ablation or "lift-off" process with ultra-short laser pulses which is achieved by illuminating the Mo-layer through the glass substrate side. The film can be removed completely as a solid disc. Thermal side effects like burr formation and micro cracks are avoided completely.[21] Figure 1.2 compares the ablation quality of a Mo-

thin film on glass substrate for the direct nanosecond (a) and picoseond (b) laser ablation, respectively with the confined picoseond laser ablation (c).[16] Only in case of the confined picoseond laser ablation, the ablated thin film is in form of a solid disc and the surrounded material is free from thermal side effects.[16,22,23] The energy needed for this process is only ~30 J/mm^3 and far below the evaporation enthalpy of Mo (~78 J/mm^3).[24,25] In addition, the complete layer can be removed by one single pulse which enables high speed processing.[16]

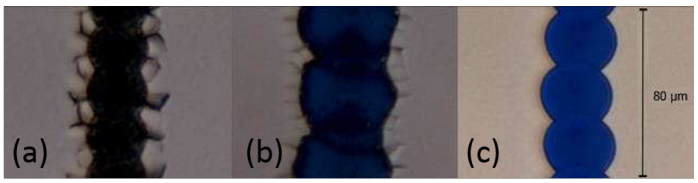

Figure 1.2.: Comparison of the ablation quality for a Mo-thin film on glass substrate. The direct nanosecond laser ablation (a) and the direct picosecond laser ablation (b) exhibit damage of the surrounded area. Only the confined picoseond laser ablation (c) shows no damage. (Picture and caption obtained from Huber et. al[16]).

For further industrial process optimization, prediction and know-how transfer to further laser processes with different materials such as laser induced forward transfer (LIFT),[26,27] blister formation,[28,29] rapid prototyping of bio sensor chips[30] or opening of dielectric layers in silicon photovoltaics,[31–33] the understanding of the physical mechanisms in detail for the confined laser ablation or "lift-off" is essential.

1.2. State of the art

The exploration of laser ablation processes are described in the literature by various groups. The mechanism of the laser "lift-off" process with laser pulse duration in the nanosecond range are reported as a generation of a vapor pressure or the pressure inside a plasma phase.

An experimental investigation of the pressure generated by nanosecond-pulses in the confined interface between transparent substrate and a thick metallic absorber for laser shock processing was performed by Fabbro et al.[34] The driving force for the shock wave formation was related to the generation of a confined plasma.

Adrian et al.[35] investigated the LIFT process, where a 15 ns laser pulse, which is irradiated through the backside of a transparent substrate, ejects a 1 μm-thick metallic film from the front side and deposits the material onto a target. A 1D simulation model was used to calculate the temperature profile with the result that the supplied laser energy was more than sufficient to melt and partially evaporate the material. It was concluded that the force for ejection should result from the vapor pressure of the partially vaporized metal.

Kattamis et al.[36] simulated a polyimide μm-film blister formation for LIFT with 40 ns pulse duration. The only driving force for the blister formation was explained by the pressure of an ideal gas and an adiabatic expansion. During the volume work, the gas was still heated by the laser energy and the pressure value was increased.

For femtosecond laser "lift-off" processing the observed effects are related to ultrafast heating or melting, which results in shock waves and leading to a delamination. The gas pressure plays only a minor role for the ablation, due to the short time interval of energy deposition and a possible vapor phase is followed by subsequent condensation.

To further explore the mechanism behind the absorption, Itina et al.[37] simulated the impact of ultra-short 100 fs pulses on a metallic bulk sample with a 1D multiphysics model including

a two-temperature model and a hydrodynamic model with a volume as a function of the pressure. The solution of the equation yielded to shock waves with velocities of several km/s. The ablation effect was explained by a compressive shock wave propagating into the bulk while the unloading rarefaction wave leads to the material expansion or removal.

That mechanical stress from thermal expansion of solid material in contrast to vapour pressure from a heated gas can be a major driving force in an ablation process was revealed by Ivanov et al.[38] in a theoretical work using a fundamental molecular dynamics simulation based on interatomic interaction. The simulation explains the formation of nanobumps in 20 nm Ni films on glass as the result of an acceleration of the thin film away from the substrate, caused by compressive stress up to 8 GPa created from thermal expansion and a subsequent plastic deformation of the material. The simulation however assumes a perfectly rigid substrate as the mechanic boundary condition implying an elastic reflection of the expanding film from the substrate and leading to a very high take-off speed of 300 m/s.

In a work by Shugaev et al.[39] the stress waves created from thermal expansion were investigated with a multiphysics continuum model including a two-temperature model and a continuum elastic model in 1D. The simulation analysed the very first stage of the LIFT processes for 200 fs pulses on 40 nm films of Au, Cr and Zn to find out why the material is ejected in different phase compositions. The result shows that with the same fluence of 0.35 J/cm^2 different electron gas and lattice temperatures are reached and that e.g. for gold the ejected material is only partially molten, which is in agreement with cited experimental work. The driving force was explained by a formation of strong pressure waves caused by instantaneous laser induced heating and subsequent unloading from the side of the free film boundary.

Zergioti et al.[40] made a comparative study of the effect of ultra-short (0.5 ps) and short (30 ns) pulses on the laser forward transfer of 40 nm Cr-films on glass. In case of fs laser pulses, a shock assisted removal was observed. An induced high pressure gradient by the fs-laser, lead to a shock wave in the direction of the Cr air-side followed by a rarefaction wave propagating in the opposite direction. When the rarefaction wave reached the substrate film interface, the Cr-layer was removed.

Previously, an analytic model was introduced by Heise et al.[20] with a description of the bulging and ablation behavior of a thin Mo-film by an ultra-short laser pulse. The laser energy is absorbed in a fraction of the layer volume defined by the optical penetration length. This irradiated volume is fully evaporated. The produced vapor pressure inside a confined volume leads to an adiabatic expansion of the film and ends in a hydrostatic pressure. Ablation occurs when the shear stress at the edges exceeds some limit. The calculated energies needed to enable these processes are four times lower than the measured ones. The complete model is based on a adiabatic expansion of a thin-film which is also the current state of the art explanation for the "lift-off" with nanosecond laser pulses.[36] However the model of a heated gas expansion was not capable to include thermal expansion and transient effects. Consequently, numerical simulation is the next step to calculate these contribution to the ablation process.

However, although the "lift-off" process with ultra short laser pulses was demonstrated in the literature, there is still a gab in the knowledge of the physical mechanism behind this ablation method.

The current dissertation is based on the research question why the Mo-layer can be removed so efficiently and the laser "lift-off" with an ultra short laser pulse is investigated by the means of numerical simulation. For this reason, a transient multiphysics and multi-time scale 3D-axisymmertic FEM-model with high temporal range is introduced which takes the

thermal expansion into account. An attempt is given which maps the complete process of the "confined" laser ablation with an ultra-short laser pulse.

In the present model, a 435 nm thin Mo-layer is irradiated through a transparent glass substrate of 3 mm thickness. The time duration ranges from femto- to microseconds to include the physical relevant time period. The following effects are taken into account: The absorption of the laser pulse in the metallic layer by the electrons; the dissipation and the heat transfer to the lattice; the heating and phase transition in the metallic film; the propagation of a melt and evaporation front; the heat dissipation inside the layer and to the adjacent material; the thermo-elastic and elasto-mechanic reaction of the material leading to a mechanical interaction with the substrate and finally an acceleration of the partially intact layer; the plastic deformation of the material under temperature and stress and, last, the motion of the layer which leads to membrane oscillations, shear forces, and strain. The space and time parameters are chosen such that it allows a comparison between this multiphysics model and experimental results of the confined laser ablation.[41–44] In these experiments a laser pulse with a pulse duration of 660 fs and 1053 nm pulse duration is irradiated through a glass substrate onto a 435nm thin Mo-layer with low fluence from 0.4 to 0.6 J/cm^2. The ablation threshold for complet layer removal is around 0.6 J/cm^2 which outperforms the processes in the cited articles[45–48] that report on direct laser ablation in terms of energy efficiency by far.

The simulation reveals that irradiation of the Mo-layer with an ultra-short laser pulse through the transparent glass substrate generates a heating rate in the order of 10^{15} K/s at the interface within the layer. As a result, acceleration of the Mo-layer is initiated by thermal expansion supported through a backward impulse from the glass substrate in the time frame of hundred picosecond. The Mo-layer then expands with a velocity of $\sim$ 100 m/s and continuous to move as an oscillating membrane. Finally a dome is formed after about 100 ns. Thanks to the plastic deformation model, the dome is stable and the layer remains finally deformed. The calculated strain at the edges of the dome exceeds the tensile stress limit at fluences that initiate the "lift-off" in experimental investigations. The complete process is thermally and mechanically in equilibrium after about 10 μs.[15] The driving mechanism of the "lift-off" is found as an ultra fast expansion and not the gas pressure, as it is mentioned in previous models.[25,35,36]

For further research the thermal part of the model is applied to a front side laser irradiation of the Mo-layer with a pulse duration range from 5 fs to 100 ps. The result showed that the vapour volume has a maximum value at a pulse duration between 10 ps and 50 ps. A pulse duration of 10 ps is observed in experimental investigation as the most efficient one for material removal.[49]

2. Methodology

Throughout this dissertation vectors, matrices and tensors are written in bold letters unless otherwise remarked.

2.1. Ultra short laser pulses

The word "Laser" is the abbreviation of "light amplification by stimulated emission of radiation". The posibility of stimulated emission was proposed by Albert Einstein in 1917.[50] The first laser was build in 1960 by Theodor H. Maiman with a cylinderical ruby made of chromium doped corundum[51] which was based on previous work from Charles Hard Townes and Arthur Leonard Schawlow.[52] Since then, the laser has found its way to a wide range of application like medicine, computer industry and material processing. The special characteristic of light emitted by a laser source is its time and space coherence. By spacial focusing a laser beam the light intensity can be increased by magnitudes onto an area in the micrometer range. Laser can be either operated as continuous wave or pulsed mode. The pulsed mode laser with a so called Q-switch are able to create pulse durations in the nanosecond range. Therefor, the losses in the resonator are increased by an electro- or acousto-optical element which allows the gain in the active median to increase. When the losses are rapidly decreased in the resonator, the laser activity is initiated and a giant short pulse is produced from the the stored energy in the gain medium with peak intensities up several gigawatts. For ultra short laser pulses with pulse durations ranging from pico- to femtoseconds, a mode-lock technique is introduced. The phase of the longitudinal laser modes are fixed which allows them to interfere constructively to a pulse train with peak intensities up several terawatt and beyond.[53]

2.2. Laser matter interaction

In principal all kind of material like metal, semiconductor and insulator can be processed by a laser beam. The key parameters affecting the laser matter interaction are the wave length and the pulse duration of the laser. By irradiating a metal surface with a continuous wave laser or a pulsed laser with a pulse duration up to the nanosecond rage, the material is mainly heated, melted and evaporated. The irradiation of a metal surface by a pico- or femtosecond pulse are additionally driven by thermally induced shock waves due to the high heating rates of $\sim 10^{12}$ - 10^{15} K/s when a material is heated up to 5000 K in a time duration in the order of 5 ps.[54]

The effective optical penetration depth $1/\alpha_{opt}$ of a material by a given laser wave length is here a crucial factor. It determinates how far the radiation penetrates into the surface of the material by a given wavelength until the peak intensity drops to a level of $1/e^2$. Typical penetration depth for a wavelength 1053 nm (1.18 eV) are shown in table 2.1 for Mo and Fused silica.

The classification of laser matter interaction with an (for the laser wave length) absorbing film on a transparent substrate can be categorized by figure 2.1.[58] The first row illustrates the condition of the laser irradiation either directly onto the (gray) absorbing layer surface

Variable	Symbol	Value	Unit
Molybdenum	$1/\alpha_{opt}$	19.1	nm
Fused silica	$1/\alpha_{opt}$	1.72	cm

Table 2.1.: Optical data of molybdenum and soda-lime glass[55–57]

(film side irradiation) or indirectly through the (blue) transparent substrate (glass substrate side irradiation). The film side can be directly irradiated while the thickness of the film is greater than the effective penetration depth (a) or comparable to the effective penetration depth (b). The film can also be irradiated through the glass substrate side with a thickness comparable to the penetration depth (c), a thickness greater than the penetration depth (d) and a thickness much greater than the effective penetration depth (e).[58]

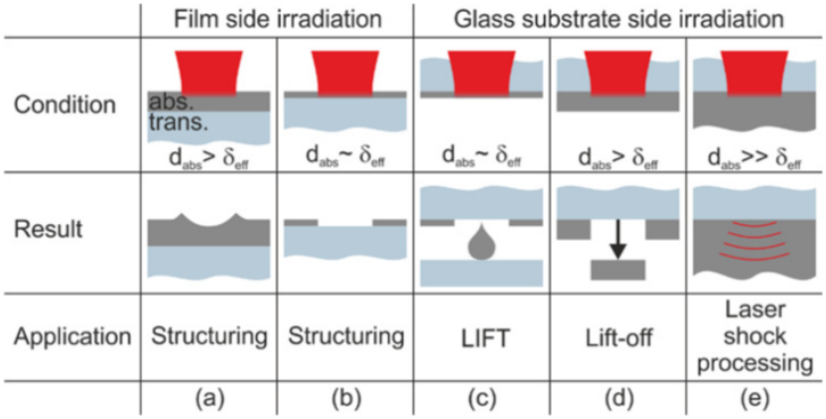

Figure 2.1.: Laser irradiation of an absorbing layer on a transparent substrate. Film side irradiation: (a) Thick and (b) thin absorbing layer. Substrate side irradiation: Thin absorbing layer with LIFT (c), "lift off" (d) and laser shock processing (e) (Picture and caption obtained from Domke et. al.[58])

In the present case a lift-off is expected with a glass as transparent layer and Mo as the absorbing laser as shown in figure 2.1(d).

2.3. Timescale

As illustrated in figure 2.2 the timescale of physical processes initiated by the interaction of an ultra-short laser pulse with matter rages over ten orders of magnited from the femtoseonds to microseconds.[59] The photon absorption happens on a time scale in the order of the pulse duration of the laser pulse and impact ionization can take up to tens of picoseconds. The carrier-carrier scattering takes place during the time scale of the photon absorption while the time duration for the carrier-phonon scattering are ranges up to tens of picoseconds. The carrier removal processes can ranges from sub-picosecond to several microseconds. Thermal and structural effects are characterized by ablation and evaporation, thermal diffusion and resodification which also can last into the microsecond range. For the present simulation study the whole time scale range was taken into account to develop a model which describes the physical processes and hence the mechanism for the driving force completely.

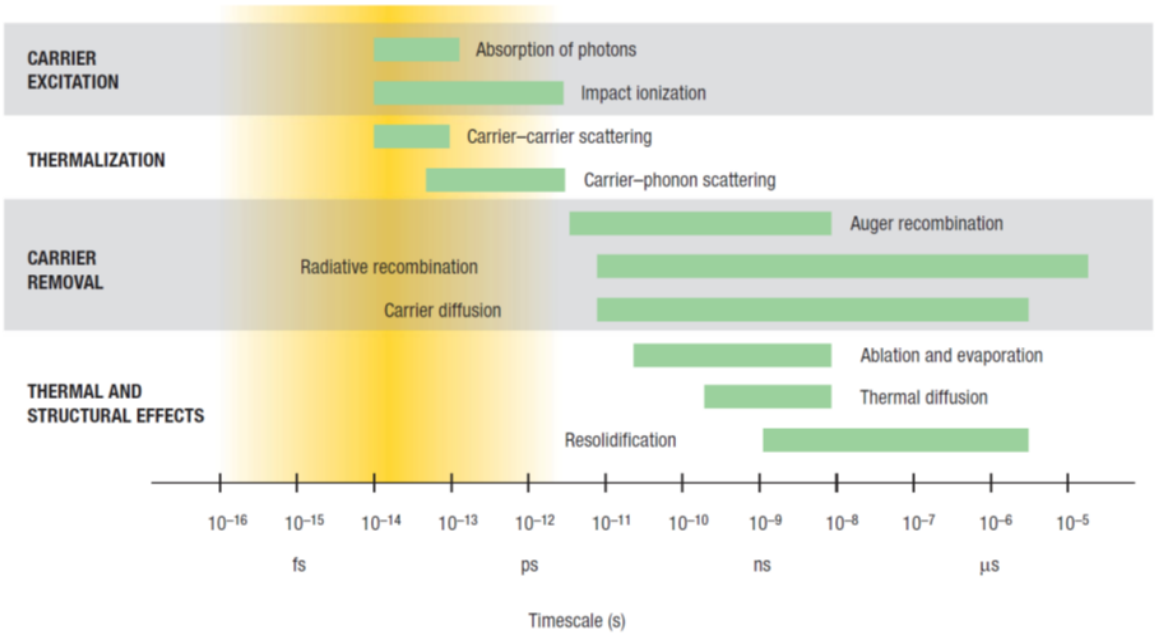

Figure 2.2.: Timescale of physical processes initiated by the interaction of a ultra short laser pulse with matter. (Picture and caption obtained from Sundaram et. al[59]).

2.4. Model assumptions

In this dissertation a FEM analysis was performed to investigate the interaction of a sample layer system based on a Mo-coated glass substrate with an ultra-short laser pulse. The simulation setup was carefully chosen, such that it is comparable to previously performed experimental work, which involves time and space resolved pump-probe microscopy studies.[41] Figure 2.3 shows a schematic cross section of this simulation setup. The ultra-short laser pulse (wavelength 1053 nm, pulse duration 660 fs) irradiates through a transparent glass substrate (∼3 mm) and is absorbed at the Mo-glass-interface by the thin Mo-layer (435 nm). No significant absorption is expected within the investigated low fluence range in the glass substrate because the glass damage threshold flunce for single pulse irradiation of the present layer system starts at 0.75 J/cm^2.[60]

It can be further seen in figure 2.3, that the geometry of the glass substrate and the Mo-layer were chosen as a cylinder. This choice of domain allows a perfect implementation of the cylindrical transverse electromagnetic modes (TEM_{00}) of the laser. Thanks to the rotational symmetry, it was possible to reduce the 3D geometry to a axisymmetric model to save computational time. Thus, cylindrical coordinates within a purely axisymmetric state was used for the entire model. The final simulation domain consisted only of a rectangle with dimensions of 435 nm height and 30 μm width which represents the Mo-layer. The Mo-layer beyond this width, the complete glass substrate and the adjacent air were all modeled with precise boundary conditions. These boundary conditions were defined on the edges by $\partial\Omega_1$, $\partial\Omega_2$, $\partial\Omega_3$ and $\partial\Omega_4$.

2.4.1. Model steps

The complete ablation process can be describe by the following eight steps (see Figure 2.4):

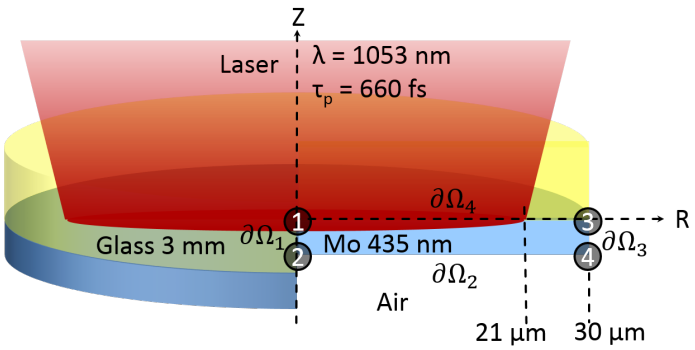

Figure 2.3.: The thin-film molybdenum layer is irradiated by a laser (wavelength 1053 nm, pulse duration 660 fs) through a transparent glass. Only the rectangular Mo-cross section is used in the axisymmetric model. Important points at the boundary of the simulation domain are numbered from 1 to 4. The maximum irradiated intensity is reached in the center at point 1. The distance from 1 to 3 is 30 μm and from 1 to 2 is 435 nm.

(a) Irradiation through the glass substrate, partial reflection and absorption by the nearly free electron gas;

(b) Heating of the electrons, thermal diffusion and heat transfer to the Mo lattice;

(c) Thermal diffusion and thermal expansion of the heated solid Mo;

(d) Additional thermal expansion at the phase transition from solid to liquid;

(e) Emergence of vapor pressure in the interface between glass and Mo-layer;

(f) Mechanical deformation of the Mo-layer;

(g) Interaction of layer and substrate leading to acceleration of layer;

(h) Radial stress from plastic deformation and shearing, if the strain limit is exceeded.

The physical assumptions to describe these steps are as follows:

Absorption, reflection and transmission

(a) The laser beam was focused with a radius of 21 μm on the Mo-surface through the glass side. Two reflections of the laser beam occurs, one at the Mo-glass interface and the other on the glass surface. The reflectivity for this layer system is measured to approx. 50 %.[25] The remaining 50 % are expected to be absorbed in the Mo-volume near the Mo-glass interface. The optical absorption depth of Mo was choosen to be about 19 nm according to table 2.2. The absorption of the ultra short laser pulse at the Mo-surface is finally modeled by Beer-Lamberts law.[61–63] This approach has the advantage, that only the intensity of the laser beam has to be considered and the wave properties can be neglected.

To obtain the precise absorbed intensity value all possible contribution form the laser beam reflections have to be considered. It turns out, that a variety of reflections can occur in the present layer system as illustrated in Figure 2.5(a). The incident laser beam is first reflected on the glass surface with a value of 4 %. The second reflection takes place at the

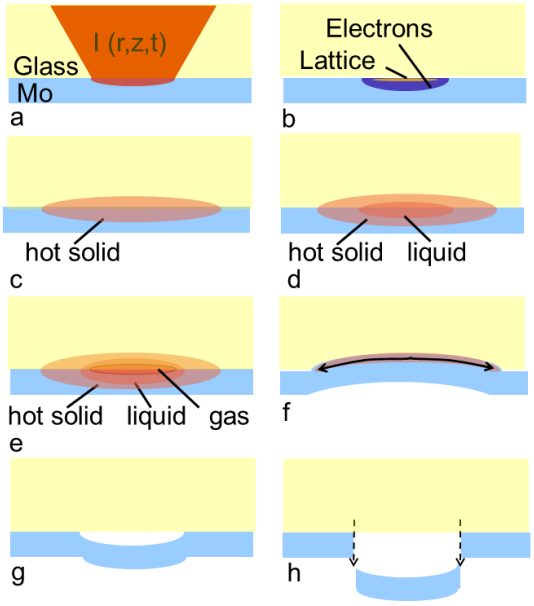

Figure 2.4.: Physical model of the ablation process. (a) A fraction of the laser pulse (660 fs, 1053 nm) energy is absorbed by the free electrons. (b) These diffuse thermally and heat up the lattice by relaxation. (c) The solid expands thermally. (d) The molybdenum is partially melted with additional thermal expansion due to melting. (e) Finally, a fraction of the melt becomes evaporated and vapor pressure rises. (f) The layer first expands in the normal direction to the glass and shock waves created from fast expansion interact with the substrate and the layer becomes accelerated. (g) The layer bulges and the material become strained in critical regions. (h) Either a dome is formed or the layer is ablated when a critical strain is exceeded.

Mo-glass interface with about 50 %. This second reflection is mainly transmitted through the glass surface back into the surrounded air and minor back reflection of about 4 % arises. Only this minor back-reflection is able to additionally contribute to the ablation process. However, the overall run-time of this back-reflection from the Mo-glass interface towards the opposite side of the glass substrate and backwards is deterined by equation 2.1 to about 30 ps (see figure 2.5(b)). Thus, the inital intensity is not enhanced since the back-reflected beam is temporally shifted from the incident beam. It is unlikely that the remaining 4 % of the back-refelcted intensity in combination with the time delay of 30 ps has a contribution to the ablation process because this value is far below the ablation threshold.[14] The incident laser beam is only expected to be absorbed inside the Mo-layer at the Mo-glass interface. Nearly complete absorption is expected during the propagation inside the Mo-layer before it reaches the opposite Mo-surface since the absorption length for Mo is about 19 nm at the chosen laser wavelength of 1053 nm (table 2.2), while the thickness of the Mo-layer is 435 nm. Only a negligible intensity fraction of $\sim 10^{-8}$ % is transmitted to the Mo-bottom surface and thus a back-reflection from this surface was also excluded in this model.

$$\Delta t = \frac{\Delta l}{v} = \frac{\Delta l}{\frac{c}{n}} = \frac{2 \cdot 3\ mm}{\frac{3 \cdot 10^8\ m/s}{1.5}} = 30\ ps \tag{2.1}$$

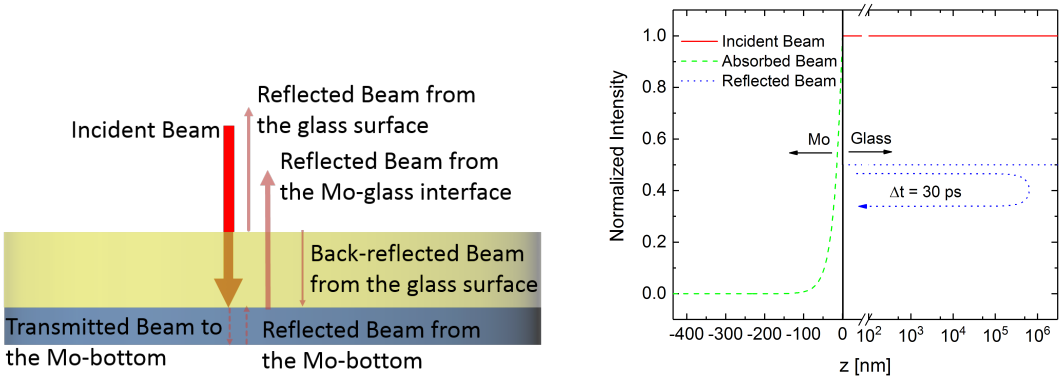

(a) (b)

Figure 2.5.: (a) All possible reflection which could contribute to the ablation process. (b) Illustration of the incident, absorbed and reflected normalized laser intensity. The intensity decreases with an exponential decay inside the Mo-layer. No contribution from the back-reflection is expected due to the time delay of 30 ps.

Electron and lattice heating

(b) The laser pulse is absorbed by a metal surface through its nearly free conduction band electrons resulting in heating of the electron gas. A equilibrium electron temperature arises through thermalization by electron-electron scattering on a femtosecond time scale.[64–66] The electron temperature, its heat capacity, the diffusion coefficient and the electron-phonon coupling are taken into account. These parameters are still under discussion, the latest value from literature were used in the presented study (table 2.3). Once the absorption of the electrons takes place, there thermal energy is immediately transferred to the solid lattice resulting in a temperature rise. The electron-phonon coupling coefficient (table 2.3) determines the amount of energy transferred per time, volume and temperature. The subsequent mechanical motion is initiated by three fundamental mechanisms with three different quantitative contributions.

Above room temperature/elevated temperature

(c) First, the linear thermal expansion is generated by the heating of the solid molybdenum above room temperature. The expansion of the volume results in a compressive stress. The respective parameter for the calculation are the well known expansion coefficient, as well as the further thermodynamic properties of the solid Mo (table 2.3).

Variable	Symbol	Value	Unit
optical absorption coefficient @1053nm	α_{opt}	$5.23 \cdot 10^7$	$1/m$
Reflectivity[14]	R_{opt}	50	%
Wavelength	λ_{opt}	1053	nm
Pulse duration	τ_p	660	fs
Beam radius @e^{-2}	w_0	21	μm
Fluence for simulation	Φ_0	$0.40 - 0.55$	J/cm^2

Table 2.2.: Data for laser pulse absorption model[67]

Above melting point

(d) Second, an additional thermal expansion during the melting of the Mo occurs if the melting temperature is exceeded. The melting temperature and heat of fusion at zero pressure for Mo are presented in table 2.3. The high compressive stress and the high heating rate of the Mo produced by the laser pulse may results in possible superheating effects.[68–70] The corresponding equation of state for Mo are not well established and so the equilibrium melt temperature was chosen. The volume expansion during the melting process was taken from experimental values obtained under equilibrium conditions.[71] The liquid interface of molten Mo reduces the adhesive force between the Mo-layer and the glass substrate. The melting temperature is hence a key parameter in this dissertation, since it defines the ablation radius by its maximum extension.

Above evaporation point

(e) Third, if the Mo is further heated above the vapor temperature, it results in a vapor phase and generates a pressure in the confined space between the Mo-layer and the glass substrate. This pressure is assumed to be the vapor pressure p_V (see table 2.3, table 2.4) which is determined by the Clausius–Clapeyron relation and depends only on the lattice temperature T_l[72,73] (equation 2.2). Again, the equilibrium data are taken into account due to the unknown equation of state (EOS) for Mo and super heating effects were neglected. The vapor pressure is the upper limit of the pressure inside the confined area between Mo-layer and glass substrate, due to the time delay while it is generated. If the pressure has a non-negligible contribution to the Mo deformation, it is overestimated. This guarantees that the question of the contribution from the gas to the ablation process can be properly answered. Figure 2.2 shows the determined vapor pressure in dependence on the lattice temperature T_l. At the vapor temperature T_V the vapor presser $p_V(T_l)$ has a value of ~110 kPa while the GPa range is reached not before ~13,000 K.

$$p_V(T_l) = p_0 \, e^{\frac{\Delta H_m}{R}\left(\frac{1}{T_V} - \frac{1}{T_l}\right)} \tag{2.2}$$

here, R is the universal gas constant.

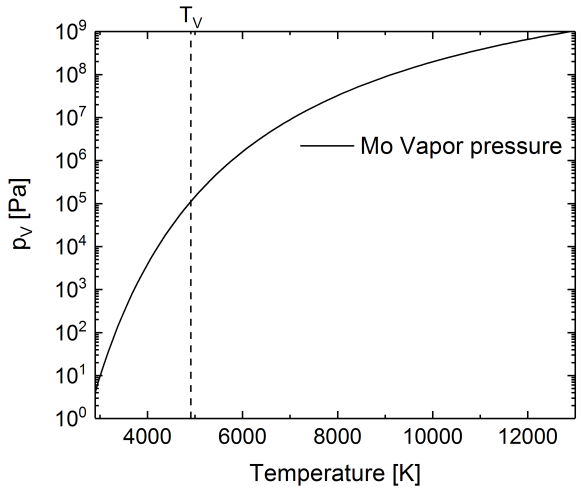

Figure 2.6.: Vapor pressure of Mo determined according to equation 2.2. The vertical dotted line denotes the vapor temperature.

Mechanical motion

(f) The creation of mechanical motion is implemented as follows. The very fast thermal Mo expansion generates very fast compressive stress at the interface that initiates stress waves which are propagate towards the normal direction. The expansion of the Mo-layer is initial expected in a thin layer close to the vicinity of the interface. The Mo-layer can be considered as a rigid plate and bend first in the direction of the glass substrate above the neutral fiber to minimize its potential energy, similar to a bimetallic strip effect. A transient continuum elastic description is necessary for the Mo-layer properties in radial direction to take this effect into account. The continuum elastic properties of the glass substrate are important to describe the momentum transfer precisely. Finally, the Mo-layer results in a vertical velocity in the opposite direction to the glass substrate. For a possible ablation, the initial velocity of the layer has to be sufficient enough to overcome the potential energy barrier of the layer under the non-uniform compression.

Layer bulging

(g) If the the layer peel away and achieve separation from the substrate, a continuous motion of the layer is expected to occur. The center of mass velocity of the layer motion is much smaller compare to the shock wave velocity, which is fast and expected in the order to the speed of sound in the Mo. During this motion the film will solidify and a nearly uniformly distributed temperature will arise. At this point, the driving forces are the radial stress originated from the thermal expansion in the radial direction and a possible remaining vapor pressure in the spacing between the Mo-layer and the glass substrate.

Layer ablation

(h) The shear stress inside the Mo-layer is created by the inertial forces, the compressive force in the radial direction and the cohesive forces outside the ablation radius. When

Variable	Symbol	Value	Unit
Heat capacity molybdenum	a	250	$J/(kgK)$
Norm factor gauss function melting	b	$(50\sqrt{2\pi})^{-1}$	1
Melting temperature	T_m	2896	K
Melting enthalpy	ΔH_M	$389 \cdot 10^3$	J/kg
Norm factor gauss function evaporating	c	$(50\sqrt{2\pi})^{-1}$	1
Vaporization temperature	T_v	4912	K
Vaporization enthalpy	ΔH_v	$6.25 \cdot 10^6$	J/kg
Width of Gaussian latent heat model (FWHM)	ΔT_l	50	K
Thermal expansion coefficient	α_{exp}	$4.8 \cdot 10^{-6}$	J/kg
Electron-phonon coupling constant	G	$13 \cdot 10^{16}$	$W/(m^3K)$
Lattice heat conductivity	k_l	135	$W/(mK)$
Specific electron heat constant	γ	$34 \cdot 10^{-3}$	$J/(kgK^2)$
Electronic heat conductivity	k_e	$k_0 \frac{T_e}{T_l}$	$W/(mK)$
Electronic heat capacity	C_e	$\gamma\, T_e$	$J/(KgK)$

Table 2.3.: Data for the thermal heat diffusion model[55, 67, 74]

Variable	Symbol	Value	Unit
Mass density	ρ	10280	kg/m^3
Young's modulus	E	321	GPa
Yield stress level	σ_{Yield}	0.3	GPa
Kinematic tangent modulus	E_{kin}	1	GPa
Vapor pressure @ 2742 K	p_0	1	Pa
Thermal expansion coefficient	α_{th}	$4.8 \cdot 10^{-6}$	m^{-1}

Table 2.4.: Material data of molybdenum[55]

some critical value is exceeded, the layer will be damaged or detached, depending on the damage. If the critical value is not exceeded, the layer keeps attached, but may be plastically deformed. Otherwise an elevated dome could not stably exist. The plastic material properties are essential to reproduce a stable dome in the simulation. The actual Mo-layer used for comparision with the experimental results[41] are produced by sputtering. Such a produced Mo-layer is less dense than the bulk Mo and its mechanical properties are anisotropic. It is worth mention that some uncertainties remain since there is a lack in literature of mechanical properties especially for the plastic behavior of thin Mo-films. In this simulation, the well-known bulk Mo material properties from literature (table 2.4) were included. For the elasto-plastic deformation model the linear elastic regime was modeled with the temperature-dependent Young's modulus and the yield stress level was chosen to 300 MPa (table 2.4). The compressibility of the liquid Mo were approximated by the Young's modulus and a liquid-like Poisson ratio of close to 0.5. Finally the shear off is expected if a critical strain is exceeded.

Overall, three sub-models were used to implement the physical mechanisms, which are the intensity absorption of the laser pulse, the heat diffusion in the electron and the lattice sub-system and finally the thermal expansion (see figure 2.7). These sub-model needed to be accurately coupled to ensure precise results. The intensity was coupled unidirectional to the electron temperature. Then, the electron temperature and the lattice temperature were bidirectional coupled. The lattice temperature was used to calculate the thermal expansion. Only the boundary condition $\partial\Omega_4$ from the thermal expansion part was couples back into the boundary condition from the lattice temperature. It is noted that on the domain level, the thermal expansion model had no feedback loop to the lattice temperature. In other words, the temperature was not affected by the structure changes in the domain, e.g. by internal friction.

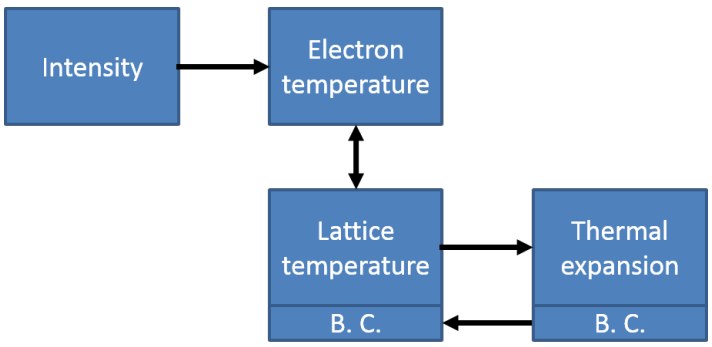

Figure 2.7.: Flow diagram for the illustration of the physical coupling in the FEM model. The abbreviation B. C. stands for boundary conditions.

2.5. Laser pulse absorption model

For the light absorption model, the propagation of light inside a material can be derived from Maxwell's equations in matter, presented here in differential form by equations 2.3.[75]

$$\boldsymbol{\nabla} \cdot \mathbf{D} = \rho_{el} \qquad \text{Gauss's law} \tag{2.3a}$$

$$\boldsymbol{\nabla} \cdot \mathbf{B} = 0 \qquad \text{Gauss's law for magnetism} \tag{2.3b}$$

$$\boldsymbol{\nabla} \times \mathbf{E} = -\frac{\partial \mathbf{B}}{\partial t} \qquad \text{Maxwell–Faraday equation} \tag{2.3c}$$

$$\boldsymbol{\nabla} \times \mathbf{H} = \mathbf{J}_{el} + \frac{\partial \mathbf{D}}{\partial t} \qquad \text{Ampère's circuital law (with Maxwell's addition)} \tag{2.3d}$$

here, $\mathbf{D}$ is the displacement field, $\mathbf{B}$ is the magnetic field, $\mathbf{E}$ is the electric field and $\mathbf{H}$ is the magnetizing field. The free charge density ρ_{el} and the free current density $\mathbf{J}_{el}$ are defined by the charge and current per volume, respectively:

$$\rho_{el} = \frac{Q}{V}; \qquad \mathbf{J}_{el} = \frac{I}{V}. \tag{2.4}$$

The material is assumed to be isotropic, which means quantities are independent from the spacial direction (full rotational symmetry), homogeneous independent of the spacial direction in translational symmetry (transnational symmetry), source free which implies that the charge density ρ_{el} is neglected.

For dielectrics like glass the conductivity σ_{el} is assumed to be zero, while in case of ohmic conductors like metals Ohm's Law can be applied:

$$\mathbf{J}_{el} = \sigma_{el}\, \mathbf{E} \qquad \text{Ohm's law} \tag{2.5}$$

2.5.1. Constitutive relations

The constitutive relations relate the displacement field (electric flux density) $\mathbf{D}$ with the electric field $\mathbf{E}$ and the magnetizing field $\mathbf{H}$ with the magnetic field (magnetic flux density) $\mathbf{B}$ trough material parameters. For a linear homogeneous isotropic medium the constitutive relation is introduced by equation 2.6:

$$\mathbf{D} = \tilde{\epsilon}\mathbf{E}; \qquad \mathbf{H} = \tilde{\mu}^{-1}\mathbf{B} \tag{2.6}$$

here, $\tilde{\epsilon}$ and $\tilde{\mu}$ is the permittivity and the permeability of the material, respectively. A linear material is considered for Mo, glass and air which means that ϵ and μ are scalar constants throughout the volume for a given frequency.

The initial free charges ρ_{el} is assumed to be zero. By combining equation 2.6 with equation 2.3a and equation 2.3d and substituting equation 2.5 into equation 2.3d one gets:

$$\nabla \cdot \mathbf{E} = 0 \tag{2.7a}$$

$$\boldsymbol{\nabla} \times \mathbf{B} = \tilde{\mu}\sigma_{el}\, \mathbf{E} + \tilde{\mu}\tilde{\epsilon}\frac{\partial \mathbf{E}}{\partial t} \tag{2.7b}$$

2.5.2. Wave equation

The well known wave equation can be derived by combining equation 2.7a and equation 2.7b with equation 2.3c and further taking its curl (see section A.1.1). For simplicity, only the electric field is written. The magnetic field exhibits a similar expression:

$$\boldsymbol{\nabla}^2\mathbf{E} - \tilde{\mu}\tilde{\epsilon}\,\frac{\partial^2\mathbf{E}}{\partial t^2} - \tilde{\mu}\sigma_{el}\,\frac{\partial\mathbf{E}}{\partial t} = 0. \tag{2.8}$$

One solution of the wave equation is a monochromatic linear polarized wave with a single frequency of ω propagating along the **Z**-direction:

$$\mathbf{E}(\mathbf{Z},t) = E_0\, e^{i(\mathbf{kZ}-\omega t)}\hat{\mathbf{e}}_y \qquad \text{linear polarized wave in y-direction,} \tag{2.9}$$

here, $\mathbf{k} = \dfrac{\omega}{c}\tilde{n}$ is the wave vector. **Z** is the propagation direction, $\hat{\mathbf{e}}_y$ the unity vector for the oscillation direction of the **E**-Field and c is the vacuum speed of light. The refractive index $\tilde{n}$ can be related to the pemittivity (dielectric function) $\tilde{\epsilon}$ which are both complex valued quantities:[76]

$$\begin{aligned}
\tilde{n}^2 &= n^2 - k^2 + i2nk = \tilde{\epsilon} = \epsilon_1 + \epsilon_2 \\
\epsilon_1 &= n^2 - k^2 = \epsilon_r \\
\epsilon_2 &= 2nk = i\,\frac{\sigma}{\omega\epsilon_0}
\end{aligned} \tag{2.10}$$

here, $\epsilon_r = \dfrac{\epsilon}{\epsilon_0}$ is the relative permittively as the real part of the dielectric function ϵ_1 and ϵ_0 is the permittively of free space. Now, equation 2.9 can be rewritten by splitting the complex refractive index into its real and imaginary part:

$$\mathbf{E}(Z,t) = E_0\, e^{i\left(\frac{\omega}{c}n\mathbf{Z}-\omega t\right)}\; e^{-\left(\frac{\omega}{c}k\mathbf{Z}\right)}\;\hat{\mathbf{e}}_y \tag{2.11}$$

By doing so, the argument of the first exponential function in equation 2.11 is complex and describes an oscillating **E**-field. The argument of the second exponential function is real negative and results in an exponential decay of the **E**-field.

The propagation of the **E**-field inside a media is manly dominated by the value of k. Insulators have typically negligible values of k whereas in conductors like metals the value of k are finite. The refractive index values of Mo is shown in table 2.5. The value for k of 4.34 will result in an immediately exponential decay of the **E**-field beneath the Mo-surface.

The **E**-field for near infrared laser light is not directly measurable due to its very fast oscillations in the order of femtoseconds. To find a measurable quantity like the average power, Pointing's theorem is applied which states that the pointing vector **S** can be expressed as:

$$\mathbf{S} = \frac{1}{\mu_0}\mathbf{E}\times\mathbf{B} = c\,\epsilon_0\mathbf{E}_0^2\, e^{i\left(\frac{\omega}{c}n\mathbf{Z}-\omega t\right)}. \tag{2.12}$$

Variable	Symbol	Value	Unit
Real part of the refractive index for Mo @1053 nm	n(Mo)	2.33	1
Imaginary part of the refractive index for Mo @1053 nm	κ(Mo)	4.34	1

Table 2.5.: Refrative index data of molybdenum[77]

The peak intensity I_0 of a monochromatic plane wave can be derived from the time average over the pointing vector $< S >$[78] and is determinable over the measurable mean laser power $\bar{P}$ in combination the beam radius w_0.

$$< \mathbf{S} >= \frac{1}{T} \int_0^T \mathbf{S}\, dt = \int_0^T e^{i\left(\frac{\omega}{c} n \mathbf{Z} - \omega t\right)}\, dt = I_0 = \frac{\bar{P}}{w_0} = \frac{c\, \epsilon_0\, n}{2} E_0^2 \tag{2.13}$$

This relationship further utilizes that the square average of any harmonic function is equal to 1/2. It is assumed that k of Mo is constant during the ablation process. This assumption is widely used for metals under the normal skin approximation[10] in contrast to a changing refractive index in semiconductor and dielectrics that is for example used for phase change materials[79,80] during the interaction of high intense laser pulse. Now, the light intensity inside the Mo-layer can be written as:

$$\mathbf{I}(Z) = I_0 e^{-2\left(\frac{\omega}{c} k \mathbf{Z}\right)}. \tag{2.14}$$

The therm $-2\left(\frac{\omega}{c} k\right)$ can be expressed as the optical absorption coefficient α_{opt}.

$$\alpha_{opt} = -2\frac{\omega}{c} k \tag{2.15}$$

By substituting equation 2.15 into equation 2.14 the Beer-Lambert Law is obtained. This approach is quite common for modelling ultra short laser pulse absorption in metals.[61–63]

$$\mathbf{I}(Z) = I_0 e^{-\alpha_{opt} \mathbf{Z}} \tag{2.16}$$

A different approach of the Beer-Lambert Law is derived from its state that the differential decay of the radiation intensity in an absorbing media is proportional to the differential propagation length. Equation 2.17 shows this relationship in form of a first order ordinary differential equation (ODE).

$$\mathrm{d}I = -\alpha_{opt}\, I\,(Z)\, \mathrm{d}Z \tag{2.17}$$

Here $I(Z)$ is the Intensity of the laser beam at the depth Z inside the Mo-layer measured from the Mo-glass interface of the incident laser beam.

2.5.3. Reflectivity, transmittance and absorption

In general, light propagating through a media can experiences reflection, absorption, transmission, scattering and re-emission. For the present study only the first three effects were taken into account. The reflectivety R_{opt}, transmittance T_{opt} and absorption A_{opt} (reflected, transmitted and absorbed power) of an normal incident plane wave can be derived by equations 2.18. In the case of normal incidence for a plane wave, the polarization has no contribution on the reflectivety, transmission and absorption.

$$R_{opt} = \left|r_{opt}\right|^2 = \frac{(n_1 - n_2)^2 + (\kappa_1 - \kappa_2)^2}{(n_1 + n_2)^2 + (\kappa_1 + \kappa_2)^2} \tag{2.18a}$$

$$T_{opt} = \frac{\tilde{n_2}}{\tilde{n_1}} \left|t_{opt}\right|^2 = k\left|\frac{4\tilde{n_1}\tilde{n_2}}{\tilde{n_1} + \tilde{n_2}}\right|^2 \tag{2.18b}$$

$$A_{opt} = \begin{cases} (1 - R) & \text{for T=0} \\ (1 - R - T) & \text{otherwise} \end{cases} \tag{2.18c}$$

where r_{opt} and t_{opt} is the reflection and transmission coefficient, respectively. The absorption value used in this model for a laser beam transmitted through the glass and absorbed by the Mo-layer is 50 % and nearly identical with measurements of a compareable Mo-glass interface reported by Heise et al.[25] obtained with a spectral photometer and a laser source with a peak fluence of 0.02 J/cm^2 in combination with a wavelength and pulse duration of 1064 nm and 10 ps, respectively (figure 2.8).

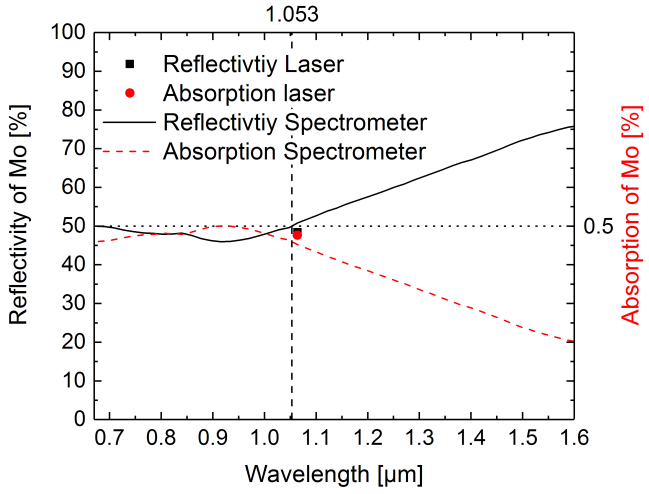

Figure 2.8.: Reflectivity and absorption of a Mo-glass sample. The solid black line and the black rectangle indicates reflectivtiy measurements with a spectral photometer and a laser source with a wavelength and pulse duration of 1064 nm and 10 ps, respectively.[14] The solid red line and red circle are the corresponding calculated absorption values in the Mo-layer. The glass substrate was assumed to be perfectly transparent.

No contributing interference effects were expected with the present layer system and the transfer matrix method is not applied for the absorption calculation.[81] All reflectivity values

Variable	Symbol	Value	Unit
Reflectivity air-glass interface @1053 nm	R_{AG}	0.04[57]	1
Reflectivity glass-Mo interface	R_{GM}	0.50 (photometer @1053 nm)[14] 0.48 (laser @1064 nm)[14]	1
Absorption Mo	A_{GM}	0.48 (photometer @1053 nm)[14] 0.48 (laser @1064 nm)[14] 0.50 (this study @1053 nm)	1

Table 2.6.: Reflectivtiy and absorption data of a Mo-glass sample

for each interface and the absorption values for Mo are summarized in in table 2.6. It is noted, that the transient absorption of the Mo-layer with 660 fs could be higher. The transient absorption of a high intens laser pulse may differ from the steady-state value depending on the choice of material.[82,83] For metals, the heating of the electronic subsystem influences the absorption behavior through electron-electron scattering and can increase and decrease the absorption during the laser pulse interaction. For semiconductor and dielectrics the transient absorption caused by an ultra short laser pulse can even be raised by magnitudes in comparison to the steady-state absorption due to the generation of free carrier by excitation over the fundamental band gab as well as avalanche or impact ionization. Due, to the lack of transient absorption model data for Mo, a steady-state absorption value was used.

2.5.4. Laser source model: Spacial and time domain

For later comparison with experimental results, performed with a mode-locked laser source with a transverse electromagnetic modes (TEM_{00}) Gaussian beam profile, the intensity distribution is assumed to be Gaussian in spacial radial direction:

$$I\left(R\right) = I_0\, e^{-\frac{2(X^2+Y^2)}{w_0^2}} = I_0\, e^{-\frac{2R^2}{w_0^2}} \tag{2.19}$$

here, w_0 is the focal beam radius at e^{-2} intensity level and R is the radial spacial cylindrical coordinate transformed from the polar coordinates X and Y .

For a precise description of the time domain a squared hyperbolic secant shaped (equation 2.20) was selected instead of a Gaussian distribution. The fixed phase relationship between the longitudinal modes in the frequency domain inside a mode-locked laser cavity, which is used for ultra short pulsed lasers produces such a pulse shape:

$$I(t) = I_0\, sech^2\left(\frac{1.76\,(30^{-12}s - t)}{\tau_p}\right) \tag{2.20}$$

here, τ_p is the pulse duration at full width half maximum (FWHM) value and t is the time parameter. The laser pulse intensity maximum is centered at 30 ps to include its rising slope.

The intensity distribution in the spacial radial direction and in the time domain is illustrated in figure 2.9. It is worth mentioning that the Guassian shape function and the Hyperbolic secant square shape function are similar, due to their relation with the Euler function (see

section A.1.2). The produced distribution in space and time differ by the fact that the Gaussian shape has a narrower slope.

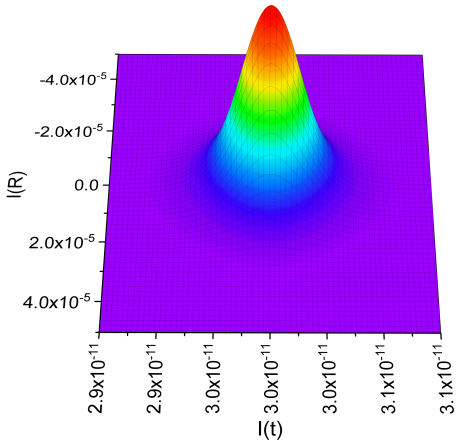

Figure 2.9.: Normalized intensity distribution of a mode-locked laser pulse with a TEM_{00} in the spacial radial I(R) and time I(t) and domain, respectively. The height of the surface is normalized to one and the color is set for better visibility.

Despite a real laser beam with a finite divergence even for a perfect Gaussian beam, the intensity distribution in spacial axial direction (towards the beam propagation) is assumed to be perfectly parallel. This assumption is carefully chosen, such that it is valid for a very small length. The beam radius distribution along the spacial Z coordinate can be calculated by equation 2.21:

$$w(z) = w_0 \sqrt{1 + \left(\frac{Z}{Z_R}\right)^2} \qquad \text{with} \quad Z_R = \frac{\pi w_0^2}{\lambda} \tag{2.21}$$

with the Rayleigh length Z_R which is defined by the propagation distance along the spacial Z coordinate from the focal beam radius w_0 to the point where the beam radius w has expanded by a factor of $\sqrt{2}$. The beam waist is illustrated in figure 2.10. For the current value of w_0 and λ (table 2.2) the Rayleigh length Z_R was calculated to $\sim$1.3 mm, which is a factor of thousand higher than the Mo-layer thickness and thus the consideration of a parallel beam is an excellent assumption.

For further comparison with experimental data, I_0 needs to be expressed in terms of measurable quantities. That is to say, the peak fluence Φ_0 and the pulse duration τ_p according to equation 2.22. The first can be derived from the mean optical laser power $\bar{P}$ calculated in section A.1.3.

$$\Phi_0 = I_0 \int_{-\infty}^{\infty} I(t)\,dt = I_0 \int_{-\infty}^{\infty} sech^2\left(\frac{1.76\,t}{\tau_p}\right) dt = I_0 \frac{2\tau}{1.76} \qquad \rightarrow \quad I_0 \quad = \frac{1.76\,\Phi_0}{2\,\tau_p} \tag{2.22}$$

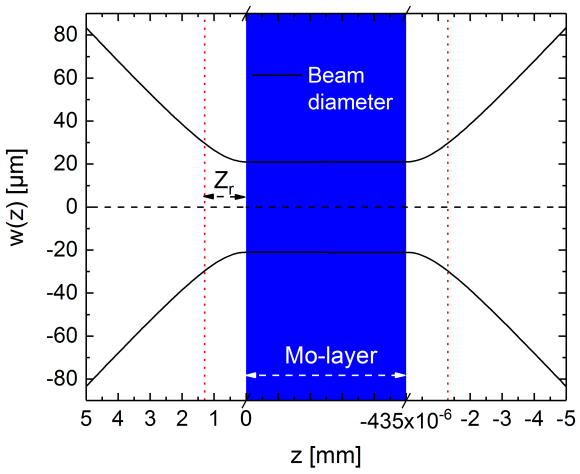

Figure 2.10.: Illustration of the beam waist along the beam propagation and inside the Mo-layer. The dimension of the Mo-layer is stretched for better visibility.

Equation 2.19, 2.20 and 2.22 can be combined to the complete laser intensity distribution, that is absorbed by the Mo at the Mo-glass interface:

$$I_4(R,t) = \underbrace{(1-R_{opt})}_{A_{opt}} \frac{1.76\,\Phi_0}{2\,\tau_p}\, e^{-\frac{2R}{w_0^2}}\, sech^2\left(\frac{1.76\,(30\cdot 10^{-12}s - t)}{\tau_p}\right) \tag{2.23}$$

here, the total optical reflectivity R_{opt} of the Mo-glass sample is included with the therm $(1-R_{opt})$ as the absorbed fraction of the laser intensity.

2.5.5. Finite element formulation

One way to initialize the finite element formulation for the Beer-Lambert law intensity distribution from Equation 2.17 is achieved by the so-called strong form of the stationary convection-diffusion equation according to equation 2.24:

$$\boldsymbol{\nabla}\cdot(\boldsymbol{\nabla}\mathbf{I} + \alpha_{opt}\mathbf{I}) = 0, \tag{2.24}$$

with the optial absorption tensor $\alpha_{\mathbf{opt}} = \begin{bmatrix} 0 & 0 \\ 0 & \alpha_{opt} \end{bmatrix}$.

The advantage of this general form is the possibility to consider also intensity dependent absorption processes, even though it was not the scope of this work. A common approach for the finite element method implementation is utilized by the so-called weak formulation.[84] The word "weak" in weak form arises from the weak requirement such that the the first derivative of $\mathbf{I}$ is integrable and $\mathbf{I}$ is continuous in contrast to the strong form where the second derivative of $\mathbf{I}$ has to be continuous. Equation 2.24 is transformed to its weak form according to equation 2.25. For this purpose equation 2.24 is multiplied by a arbitrary test

function $\mathbf{v} = \mathbf{v}(R, Z)$ which has to satisfy the requirement of continuously differentiable and is integrated over the hole domain Ω_0. The test function $\mathbf{v}$ is part of the Hilbert space. It is indicated that in general equation 2.25 is a stationary equation and the time parameter t only appears in the boundary condition of $\partial\Omega_4$.

$$\int_{\Omega_0} \mathbf{v}\boldsymbol{\nabla} \cdot (\boldsymbol{\nabla}\mathbf{I} + \alpha_{opt}\mathbf{I}) \; \mathrm{d}V_0 = 0 \tag{2.25}$$

Then, the divergence theorem is applied to equation 2.25:

$$\int_{\Omega_0} \mathbf{v}\boldsymbol{\nabla} \cdot (\boldsymbol{\nabla}\mathbf{I} + \alpha_{opt}\mathbf{I}) \; \mathrm{d}V_0 = \int_{\partial\Omega_0} \mathbf{v} \, (\boldsymbol{\nabla}\mathbf{I} + \alpha_{opt}\mathbf{I})^T \, \mathbf{n} \; \mathrm{d}A_0 - \int_{\Omega_0} (\boldsymbol{\nabla}\mathbf{v})^T \, (\boldsymbol{\nabla}\mathbf{I} + \alpha_{opt}\mathbf{I}) \; \mathrm{d}V_0 = 0. \tag{2.26}$$

This volume integral expansion is explained in section A.1.4. The volume and the surface integral is equal to the integral over the coordinate components. For a axial symmetric geometry it yields to:

$$\int_{\Omega_0} (\cdot) \; \mathrm{d}V_0 = \int_R \int_Z \int_\Theta (\cdot) \; R \; \mathrm{d}R \; \mathrm{d}Z \; \mathrm{d}\Theta \qquad \text{for the volume} \tag{2.27a}$$

$$\int_{\partial\Omega_0} (\cdot) \; \mathrm{d}A_0 = \int_R \int_Z \int_\Theta (\cdot) \; R \; \mathrm{d}R \; \mathrm{d}\Theta \qquad \text{for the surface} \tag{2.27b}$$

2.5.6. Optical boundary conditions and initial values

The optical boundary conditions were axisymmetric in the case of $\partial\Omega_1$ and "zero flux" for all other boundaries (see figure 2.11). In addition, the intensity distribution in spacial radial direction and in the time domain was defined on $\partial\Omega_4$ according to equation 2.23. The boundary conditions are summarize in table 2.7. The boundary conditions $\partial\Omega_2$, $\partial\Omega_3$ and $\partial\Omega_4$ ensures the conversation of the flux $-\mathbf{n} \cdot \boldsymbol{\nabla}\mathbf{I} = 0$ which is equal to the absence of a heat source inside the domain.

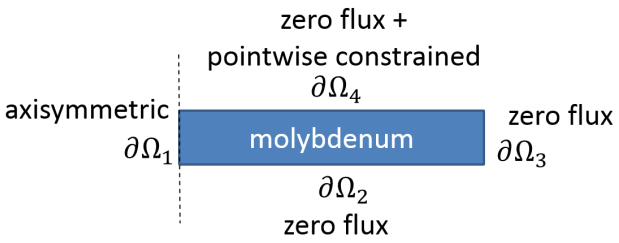

Figure 2.11.: Boundary condition for the optical absorption model.

B.C.	Intensity
$\partial\Omega_1$	Axisymmetric
$\partial\Omega_2$	$-\mathbf{n}\cdot(\boldsymbol{\nabla}\mathbf{I}+\alpha_{opt}\mathbf{I})=0$
$\partial\Omega_3$	$-\mathbf{n}\cdot(\boldsymbol{\nabla}\mathbf{I}+\alpha_{opt}\mathbf{I})=0$
$\partial\Omega_4$	$\begin{cases} \mathbf{I}_4(\mathbf{R},t)-\mathbf{I}=0 & (eq\ 2.23) \\ -\mathbf{n}\cdot(\boldsymbol{\nabla}\mathbf{I}+\alpha_{opt}\mathbf{I})=0 & \end{cases}$

Table 2.7.: Optical boundary conditions (b.c.)

The initial values were set as follows. The Intensity at time zero had a negligible but infinite value of one for convergence reasons. The initial intensity time derivative was zero (see equation 2.28).

$$\mathbf{I}(t=0)=1; \qquad \frac{\partial\mathbf{I}}{\partial t}(t=0)=0 \tag{2.28}$$

2.5.7. Analytic formulation

Basically, an ultra short laser pulse are able to provide photon densities which are sufficient for nonlinear (multi-photon) absorption and thus the absorption may depends on the intensity. Multi-photon absorption occurs typically in semiconductor and insulators where the band gab is greater than the photon energy of the laser beam. If an electron is excited from the valence to the conduction band a hole is produced in the valence band. Equation 2.29 describes the intensity decay during the absorption from the surface into the material.

$$I\left(z\right)=I_0\left(e^{-\alpha_{opt}\,Z}+e^{-\beta_{opt}\,Z\,I}+e^{-\gamma_{opt}\,Z\,I^2}+...\right) \tag{2.29}$$

Metals, initially provides a very high free-like electron density in the conduction band. These electrons are able to absorb photons by linear absorption (single-photon) resulting in higher electron energies and subsequent higher electron temperature. Only single photon absorption is considered in this study. The absorption is considered to be linear and independent from the intensity. For this special case equation 2.17 can be further solved to its analytic solution:

$$I\left(z\right)=I_0\,e^{-\alpha_{opt}\,Z}. \tag{2.30}$$

Equation 2.23 and equation 2.30 can be combined to the complete laser intensity distribution inside the Mo-layer:

$$I(R,Z,t) = \underbrace{(1-R_{opt})}_{A_{opt}} \frac{1.76\,\Phi_0}{2\,\tau_p}\, e^{-\alpha_{opt}\,Z}\, e^{-\frac{2R}{w_0^2}}\, sech^2\left(\frac{1.76\,(30^{-12}s - t)}{\tau_p}\right). \tag{2.31}$$

2.6. Thermal heat diffusion and phase change model

2.6.1. Thermal heat transfer

In the present subsection the heat transfer initiated by the laser intensity distribution (equation 2.31) is described. Heat transfer in a solid matter can occurs in form of radiation and diffusion. At first a calculation is introduced to estimate the contribution from each of the both physical mechanisms. In case of heat transfer by radiation the heat flux can be described by the Stefan-Boltzmann equation.

$$q_l = \epsilon_{th}\sigma_{th}(T_l^4 - T_{ref}^4) \tag{2.32}$$

where q_l is the heat flux, T_l and T_{ref} is the actual temperature and the ambient temperature, respectively, ϵ_{th} is the emissivity and σ_{th} is the Stefan–Boltzmann constant. With an estimated temperature difference of $\Delta T = 5000$ K (above Mo evaporation) the heat flux in the radiation case is in the order of 35 MW/m^2. In case of heat transfer by diffusion in solid matter the heat flux can be described by Fourier's law:

$$q = k_l \boldsymbol{\nabla} T_l = k_l \frac{\partial T_l}{\partial Z} \approx k_l \frac{\Delta T_l}{\Delta Z} \tag{2.33}$$

here k_l is the thermal conductivity and $\boldsymbol{\nabla} T_l$ is the temperature gradient which can be written in cylinder coordinates as:

$$\boldsymbol{\nabla} T_l = \frac{\partial T_l}{\partial R}\mathbf{E}_R + \frac{1}{R}\frac{\partial T_l}{\partial \Theta}\mathbf{E}_\Theta + \frac{\partial T_l}{\partial Z}\mathbf{E}_Z \tag{2.34}$$

Here, $\mathbf{E}_{R,\Theta,Z}$ is the unity vector in the radial, azimuthal and axial direction, respectively. With the same estimated temperature difference of $\Delta T = 5000\ K$ (above Mo evaporation) as in the radiation case and the Mo-layer thickness as the length difference Δz the heat flux by diffusion is in the order of 1.5 TW/m^2. This value for the heat flux is five orders of magnitude higher than in the radiation case. Thanks to the result of this estimation it was possible to take only heat transfer by conduction into account and neglect the contribution for the heat transfer by radiation.

The heat transfer by conduction in solid matter can be described by the heat equation in form of a second order parabolic partial differential equation (PDE):

$$\rho\, C_l \left(\frac{\partial T_l}{\partial t}\right) - \boldsymbol{\nabla} \cdot (k_l \boldsymbol{\nabla} T_l) - Q = 0 \tag{2.35}$$

here, ρ is the mass density, C_l is the heat capacity, T_l is the Temperature, t is the time parameter, k_l is the thermal conductivity and Q is a volumetric heat source.

The divergence of the temperature gradient in cylindrical coordinates is introduced in section A.2.1.

2.6.2. Two temperature model

By optically exiting a metal with an ultra-short laser pulse, the electrons are initially in non-equilibrium distribution for a very short time duration. This time duration is in the order of a few fs as illustrated in figure 2.12 (a),[85] the electron transport is considered as ballistic. Subsequent, electron-electron equilibrium is achieved by thermalization and a Fermi distribution is formed (see figure 2.12 (b)[85]). At this time an electron temperature can be defined and the heat diffusion inside the electron sub-system is ascribed.[61,62,64,85–90]

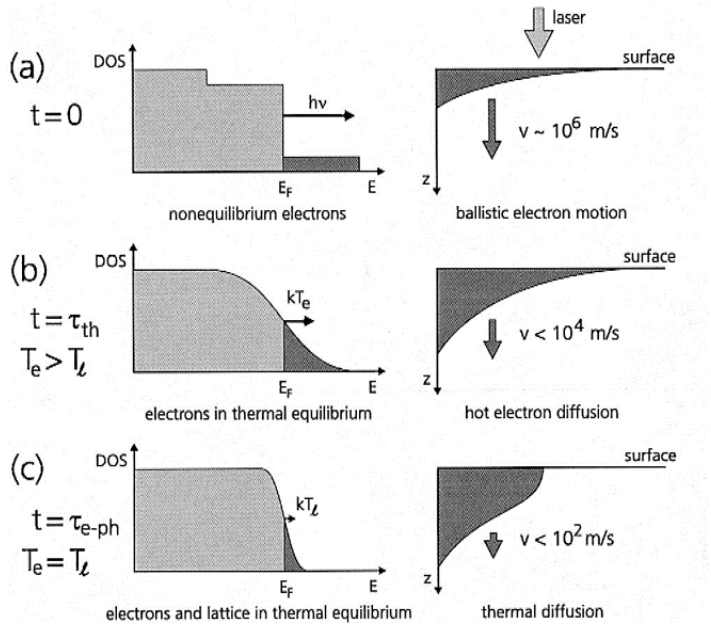

Figure 2.12.: Relaxation phases of optical excited electron in metals. (a) nonequilibrium electron distribution which may results in ballistic electron motion. (b) Electons are relaxed to thermal equilibrium and a Fermi distribution. The electron diffusion is driven by a temperature gradient. (c) Electrons and lattice are in equilibrium.(Picture and caption obtained from Hohlfeld et. al.[85])

The effect of ballistic electron distribution for different metals are still under debate.[61,74,91–93] Thus, in this study only the thermalized electrons with a defined Fermi distributed temperature was taken into account, which is a common approach for laser material processing simulation.

For ultra-short pulse laser heating the heating rate τ_h is comparable to or shorter than the electron-phonon collision frequency τ_{ep} ($\tau_h \leqslant \tau_{ep}$).[64,88,94–96] In the present case with a heating rate of about 10^{15} K/s the classical one temperature Fourier law needs to be extended to a two temperature approach, where the electron and lattice subsystem are described by two coupled heat diffusion equations:[64]

$$\rho C_e(T_e)\frac{\partial T_e}{\partial t} - \boldsymbol{\nabla}(k_e(T_e,T_l)\boldsymbol{\nabla}T_e) - G(T_e - T_l) - Q = 0 \tag{2.36a}$$

$$\rho C_l(T_l)\frac{\partial T_l}{\partial t} - \boldsymbol{\nabla}(k_l\ \boldsymbol{\nabla}T_l) + G(T_e - T_l) = 0. \tag{2.36b}$$

where, T is the temperature, ρ is the mass density, C are the heat capacity at constant pressure, k are the specific thermal conductivity and G is the electron–phonon coupling constant. The subscripts e and l label electron and lattice, respectively. The electron and lattice temperature are typically attain equilibrium on a time scale of tens of picoseconds (see figure 2.12(c)).[85]

Heating of the Mo-layer was initiated by a volumetric heat source Q, which is exclusively introduced in the electron subsystem. The implementation of Q can be achieved by taking the derivative of I (equation 2.31) with respect to Z:

$$Q\left(r,z,t\right) = \frac{\partial I\left(R,Z,t\right)}{\partial Z}. \tag{2.37}$$

Finally, the heat source exhibits the following form:

$$Q\left(R,Z,t\right) = \underbrace{\left(1-R_{opt}\right)}_{A_{opt}} \frac{1.76\,\Phi_0}{2\tau_p} e^{-\frac{2\,R}{w_0^2}}\ \alpha_{opt}\ e^{-\alpha_{opt}\,Z}\ sech^2\left(\frac{1.76\left(30\cdot 10^{-12}s - t\right)}{\tau_p}\right). \tag{2.38}$$

2.6.3. Phase change model

During laser pulse heating a material can undergo phase changes if the melting and evaporation point is exceeded. A phase change model was applied to the tow-temperature model (see equation system 2.36) which is exclusively implemented into the lattice subsystem equation 2.36b by the lattice heat capacity with the heat of melting and evaporation:

$$C_l(T_l) = a + \Delta H_M\ b\ e^{-\frac{1}{2}\left(\frac{T_l - T_M}{\Delta T_l}\right)^2} + \Delta H_V\ c\ e^{-\frac{1}{2}\left(\frac{T_l - T_V}{\Delta T_l}\right)^2}. \tag{2.39}$$

All included parameters are described in table 2.3. Two Gaussian functions of finite width ΔT_l were centered around the melting temperature T_M and the evaporation temperature T_V. This approach is an approximation in contrast to a delta function which gives the mathematical exact solution but it was unavoidable to make the model numerically solvable. Figure 2.13 illustrates the function of the lattice heat capacity in dependence on the lattice temperature. The enthalphy is also plotted in this figure to demonstrate the rise in internal energy during the phase transitions. The heat of evaporation for molybdenum ΔH_V is approximately 16 times higher than the heat of melting ΔH_M. For the liquid specific heat the same value is chosen than for the solid material.

2.6.4. Finite element formulation

The implementation of the heat diffusion equation into the FEM formulation leads to a nonlinear problem, since the heat capacity $C_{p;e,l}$ and the thermal conductivity k_e depends on the Temperature $T_{e,l}$. The equation system 2.36 is converted to its weak form with an arbitrary test function $\mathbf{v}$, like in the intensity case:

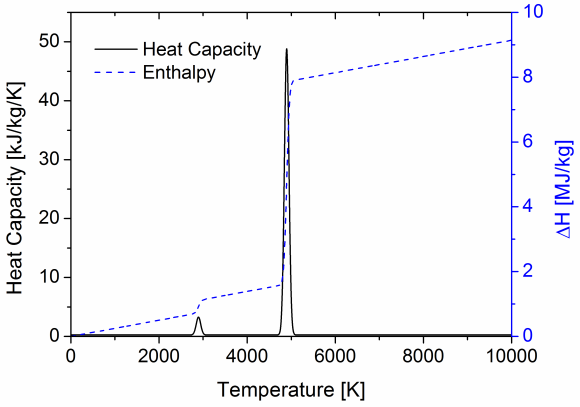

Figure 2.13.: Heat capacity and enthalpy vs. temperature. The latent heat for melting and evaporation is modelled by a Gaussian distribution.

$$\int_{\Omega_0} \mathbf{v}\ \rho\ C_{p;e}(\mathbf{T}_e)\ \dot{\mathbf{T}}_e\ \mathrm{d}V_0 - \int_{\Omega_0} \mathbf{v}\boldsymbol{\nabla} \cdot \overbrace{(-\mathbf{k}_e(\mathbf{T}_e, \mathbf{T}_l)\boldsymbol{\nabla}\mathbf{T}_e)}^{\mathbf{q}_e(\mathbf{T}_e,\mathbf{T}_l)}\ \mathrm{d}V_0 - \int_{\Omega_0} \mathbf{v}\left(\mathbf{Q} - G\left(\mathbf{T}_e - \mathbf{T}_l\right)\right)\ \mathrm{d}V_0 = 0 \tag{2.40a}$$

$$\int_{\Omega_0} \mathbf{v}\ \rho\ C_{p;l}(\mathbf{T}_l)\ \dot{\mathbf{T}}_l\ \mathrm{d}V_0 - \int_{\Omega_0} \mathbf{v}\boldsymbol{\nabla} \cdot \underbrace{(-\mathbf{k}_l\boldsymbol{\nabla}\mathbf{T}_l)}_{\mathbf{q}_l(\mathbf{T}_l)}\ \mathrm{d}V_0 - \int_{\Omega_0} \mathbf{v}\left(G\left(\mathbf{T}_e - \mathbf{T}_l\right)\right)\ \mathrm{d}V_0 = 0. \tag{2.40b}$$

The thermal conductivity matrix for the electron and lattice sub-system, respectively is defined by

$$\mathbf{q}_{e,l} = \mathbf{k}_{e,l}\ \boldsymbol{\nabla}\ \mathbf{T}e, l = \begin{bmatrix} q_{R;e,l} \\ q_{Z;e,l} \end{bmatrix} = - \begin{bmatrix} k_{RR;e,l} & 0 \\ 0 & k_{ZZ;e,l} \end{bmatrix} \begin{bmatrix} \dfrac{\partial}{\partial R} \\ \dfrac{\partial}{\partial Z} \end{bmatrix} \mathbf{T}_{e,l} \tag{2.41}$$

.

For an isotropic material $k_{RR;e,l} = k_{ZZ;e,l}$ can be assumed.

The divergence theorem is applied to the second therm of equation 2.40a and 2.40b. For simplicity only one equation is used for the formulation with subscripts denoting the electron or lattice heat equation.

$$\int_{\Omega_0} \mathbf{v}\boldsymbol{\nabla} \cdot (-\mathbf{k}_{e,l}(\mathbf{T}_{e,l})\boldsymbol{\nabla}\mathbf{T}_{e,l})\ \mathrm{d}V_0 = \int_{\partial\Omega_0} \mathbf{v}\left(\mathbf{k}_{e,l}(\mathbf{T}_{e,l})\boldsymbol{\nabla}\mathbf{T}_{e,l}\right)^T \mathbf{n}\ \mathrm{d}A_0 - \int_{\Omega_0} (\boldsymbol{\nabla}\mathbf{v})^T \mathbf{k}_{e,l}(\mathbf{T}_{e,l})\boldsymbol{\nabla}\mathbf{T}_{e,l}\ \mathrm{d}V_0 \tag{2.42}$$

By inserting equation 2.42 into equation 2.40a and 2.40b it yields to:

$$\int_{\Omega_0} \mathbf{v}\ \rho\ C_{p;e}(\mathbf{T}_e)\ \dot{\mathbf{T}}_e\ \mathrm{d}V_0 + \int_{\Omega_0} (\boldsymbol{\nabla}\mathbf{v})^T \mathbf{k}_e(\mathbf{T}_e, \mathbf{T}_l)\boldsymbol{\nabla}\mathbf{T}_e\ \mathrm{d}V_0 =$$

$$\int_{\Omega_0} \mathbf{v}\left(\mathbf{Q} - G\left(\mathbf{T}_e - \mathbf{T}_l\right)\right)\ \mathrm{d}V_0 - \int_{\partial\Omega_0} \mathbf{v}\underbrace{\left(\mathbf{k_e}(\mathbf{T}_e, \mathbf{T}_l)\boldsymbol{\nabla}\mathbf{T}_e\right)^T \mathbf{n}}_{\mathbf{q}_e(\mathbf{T}_e, \mathbf{T}_l)}\ \mathrm{d}A_0 \tag{2.43a}$$

$$\int_{\Omega_0} \mathbf{v}\ \rho\ C_{p;l}(\mathbf{T}_l)\ \dot{\mathbf{T}}_l\ \mathrm{d}V_0 + \int_{\Omega_0} (\boldsymbol{\nabla}\mathbf{v})^T \mathbf{k}_l\boldsymbol{\nabla}\mathbf{T}_l\ \mathrm{d}V_0 =$$

$$\int_{\Omega_0} \mathbf{v}\left(G\left(\mathbf{T}_e - \mathbf{T}_l\right)\right)\ \mathrm{d}V_0 - \int_{\partial\Omega_0} \mathbf{v}\underbrace{\left(\mathbf{k_l}\boldsymbol{\nabla}\mathbf{T}_l\right)^T \mathbf{n}}_{\mathbf{q}_e(\mathbf{T}_l)}\ \mathrm{d}A_0. \tag{2.43b}$$

By rearranging equation 2.43a and 2.43b the electron and lattice temperature can be separated in each therm of the equations:

$$\int_{\Omega_0} \mathbf{v}\ \rho\ C_{p;e}(\mathbf{T}_e)\ \dot{\mathbf{T}}_e\ \mathrm{d}V_0 + \int_{\Omega_0} (\boldsymbol{\nabla}\mathbf{v})^T \mathbf{k}_e(\mathbf{T}_e, \mathbf{T}_l)\boldsymbol{\nabla}\mathbf{T}_e - G\ \mathbf{T}_e\ \mathrm{d}V_0$$

$$-\int_{\Omega_0} \mathbf{v}\ G\ \mathbf{T}_l\ \mathrm{d}V_0 = -\int_{\Omega_0} \mathbf{v}\ \mathbf{Q}\ \mathbf{T}_l\ \mathrm{d}V_0 + \int_{\partial\Omega_0} \mathbf{v}\underbrace{\left(\mathbf{k_e}(\mathbf{T}_e, \mathbf{T}_l)\boldsymbol{\nabla}\mathbf{T}_e\right)^T \mathbf{n}}_{\mathbf{q}_e(\mathbf{T}_e, \mathbf{T}_l)}\ \mathrm{d}A_0 \tag{2.44a}$$

$$\int_{\Omega_0} \mathbf{v}\ \rho\ C_{p;l}(\mathbf{T}_l)\ \dot{\mathbf{T}}_l\ \mathrm{d}V_0 + \int_{\Omega_0} (\boldsymbol{\nabla}\mathbf{v})^T \mathbf{k}_l\boldsymbol{\nabla}\mathbf{T}_l\ - G\ \mathbf{T}_l\ \mathrm{d}V_0$$

$$+\int_{\Omega_0} \mathbf{v}\ G\ \mathbf{T}_e\ \mathrm{d}V_0 = \int_{\partial\Omega_0} \mathbf{v}\underbrace{\left(\mathbf{k_l}\boldsymbol{\nabla}\mathbf{T}_l\right)^T \mathbf{n}}_{\mathbf{q}_e(\mathbf{T}_l)}\ \mathrm{d}A_0. \tag{2.44b}$$

2.6.5. Thermal boundary conditions and initial values

For the electron heat diffusion subsystem, all boundaries were modeled as thermally insulated, such that the heat is completely transferred to the lattice inside the domain. For the lattice heat diffusion sub-equation, figure 2.14 and table 2.8 gives an overview of the selected thermal boundary conditions.

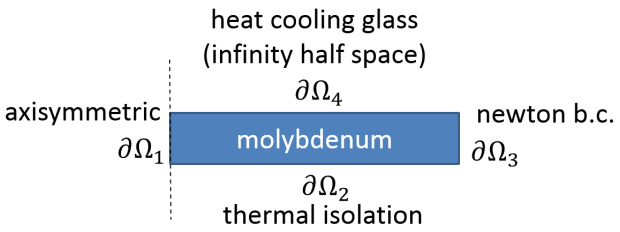

Figure 2.14.: Boundary conditions for the thermal model.

The boundary condition $\partial\Omega_1$ was modeled as axisymmetric. The boundary towards the air side $\partial\Omega_2$ are treated as insulated. The boundary conditions for the interface to the continuous Mo $\partial\Omega_3$ and towards the glass substrate $\partial\Omega_4$, however, were carefully selected to model the temperature evolution precisely, after the large temperature inhomogeneity within the film thickness has decreased. Then, after about a nanosecond, the radial temperature distribution in the layer and the resulting forces depend predominately on the heat losses to the outside region. $\partial\Omega_3$ to the radially continuing metal layer was modeled as a Newton boundary condition. This is sufficient because the radial extension of the simulation domain is sufficiently large, such that the major fraction of the heat loss is to the glass. $\partial\Omega_4$ to the glass substrate is derived from the Green function of the heat equation with heat loss to an infinite half space defined by the thermal conductivity k_{gl} and heat capacity $C_{p;gl}$ of the glass. The thermal state of the half space was implemented in the temperature gradient along the boundary. Additionally, a gap of width u between the bulging metal and the glass had been taken into account in the effective conductivity λ_{eff}. The accuracy of this boundary condition has been confirmed with a variety of test calculations containing the glass substrate in an extended domain instead of the boundary condition.

B.C.	Lattice temperature	Electron temperature
$\partial\Omega_1$	Axisymmetric	Axisymmetric
$\partial\Omega_2$	$-\mathbf{n}(k_l\nabla T_l) = 0$	$-\mathbf{n}(k_l\nabla T_e) = 0$
$\partial\Omega_3$	$-\mathbf{n}(k_l\nabla T_l) = q_0$, $q_0 = h(T_{l;ext} - T_l)$	
$\partial\Omega_4$	$-\mathbf{n}(k_l\nabla T_l) = -\lambda_{eff}\left(T_l\sqrt{\frac{\rho C_{p;gl}}{k_{gl}\pi t}} + \frac{\mathrm{d}T_l}{\mathrm{d}t}\sqrt{\frac{\rho C_{p;gl}t}{k\pi}}\right)$	

Table 2.8.: Boundary conditions (B.C.) for the lattice and electron heat diffusion sub-equation.

Variable	Symbol	Value	Unit
Effective heat conductivity	λ_{eff}	$\frac{0.5\cdot 10^{-6} - u}{\left(\frac{0.5\cdot 10^{-6} - u}{1.4}\right) + \left(\frac{-u}{0.03}\right)}$	$W/(mK)$
Heat transfer coefficient	q_0	$70\ 10^6$	W/m^2

Table 2.9.: Parameters for the boundary condition models

The initial values are set as follows. The electron and lattice temperature at time zero was set to room temperature, respectively.

$$\mathbf{T}_{e,l}(t=0) = 273.14\ K \tag{2.45}$$

2.7. Thermal expansion model

The lattice temperature $\mathbf{T}_l$ calculated in the previous section 2.6 is able to initiate a thermal expansion in the Mo-layer. This thermal expansion may causes mechanical motion of the Mo-layer which is subjected to inertia forces, thermal and deformation stress in the volume, pressure and adhesion forces at the boundary. It may leads to large and possibly nonlinear deformation. Moreover, plastic deformation can occur and damping effects are introduced on oscillatory motion. For large displacements, tow coordinate systems are required. The first is the reference material frame which is the fixed in space and the second is the so called current spacial frame which is fixed to the moving and deformed body. The implementation of the equations in structural mechanics were based on the principle of virtual work. A total Lagrangian description was used exclusively for the structural analysis. In this description all variables from the equations of virtual work are used in the material configuration. The description for solid mechanics presented here can be found in many textbooks e.g.[97–100] All materials were assumed to be isotropic. This assumption provides a sufficient good representation of the poly-crystalline Mo and the amorphous glass substrate.

2.7.1. Kinematics

Initially the body (a cylindrical disc) is in a stress free un-deformed reference configuration and its geometry is described by cylindrical coordinated R, Θ and Z:

$$0 \leqslant R \leqslant A; \qquad 0 \leqslant \Theta \leqslant 2\pi; \qquad 0 \leqslant Z \leqslant B \tag{2.46}$$

here, A and B is the radius and the height of the cylinder, respectively. During deformation the geometry in the un-deformed material configuration is mapped to the spacial configuration which can be described by a nonlinear mapping function φ. The domain Ω_0 and the boundary $\partial\Omega_0$ were defined in the reference domain, while Ω and $\partial\Omega$ were implemented in the current domain, respectively. All domains and boundaries are a subset of the three dimensional real number space $\mathbb{R}^3$. Figure 2.15 illustrates a mapping of a point P to a point p via φ.

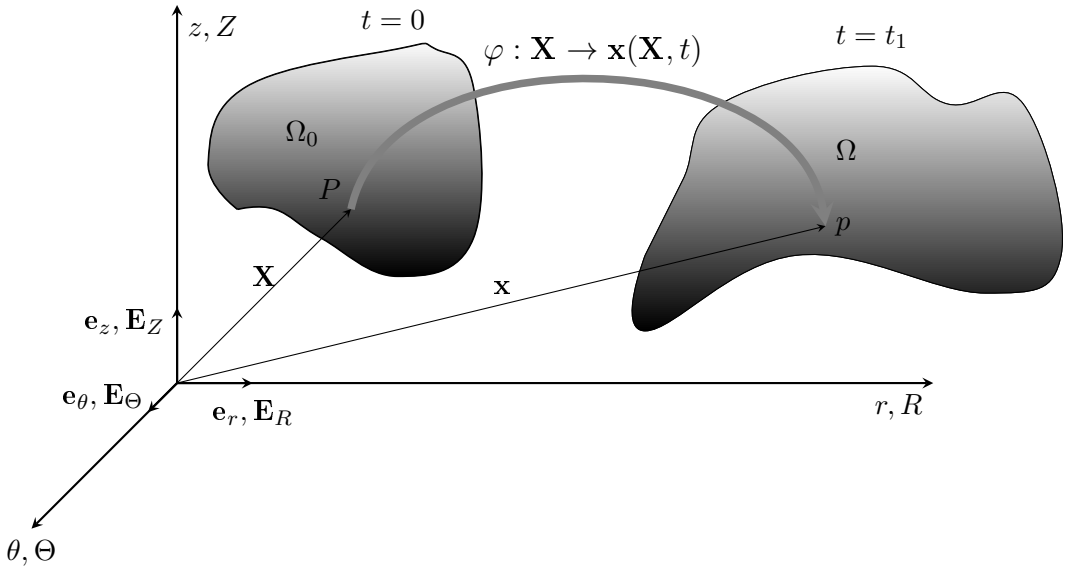

Figure 2.15.: Mapping from the material to the spacial frame.

$$\begin{aligned} &\varphi : \Omega_0 \to \Omega; && \Omega_0, \Omega \subseteq \mathbb{R}^3 \\ &\varphi : \mathbf{X} \to \mathbf{x}(\mathbf{X}, t) \end{aligned} \tag{2.47}$$

$\mathbf{X} = \left[R, \Theta, Z\right]^T$ are points in the material coordinate system which are mapped via φ to points $\mathbf{x} = \left[r, \theta, z\right]^T$ in the spacial coordinate system. The basis vectors of the un-deformed material geometry are written in upper case letters $\mathbf{E}_R$, $\mathbf{E}_\Theta$ and $\mathbf{E}_Z$ while its spacial geometry are written in lower case letters $\mathbf{e}_r$, $\mathbf{e}_\theta$ and $\mathbf{e}_z$.

$$\mathbf{X} = R\mathbf{E}_r + \Theta\mathbf{E}_\Theta + Z\mathbf{E}_z \tag{2.48a}$$
$$\mathbf{x} = r\mathbf{e}_r + \theta\mathbf{e}_\theta + z\mathbf{e}_z \tag{2.48b}$$

The displacement of the points from the material configuration to points in the spacial configurations is described by:

$$\mathbf{u}(\mathbf{X}, t) = \mathbf{x}(\mathbf{X}, t) - \mathbf{X}, \tag{2.49}$$
$$\tag{2.50}$$

with the displacement vector $\mathbf{u}$ which is a function of space and time. For the present axisymmetric geometry $\mathbf{u}$ is presented in cylindrical coordinates and only depends spatially on the R and Z coordinate, while the Θ coordinate vanishes due to the rotational symmetry:

$$\mathbf{u}(\mathbf{X}, t) = u(R, Z, t)\mathbf{E}_r + w(R, Z, t)\mathbf{E}_z = \begin{bmatrix} u(R, Z, t) \\ w(R, Z, t) \end{bmatrix}. \tag{2.51}$$

The radial displacement coordinate u was replaced by a new dependent variable $uor = \frac{u}{r}$ to avoid singularities for inverse values near the rotation axis.[101, 102] It is worth mentioning that the displacement field $\mathbf{u}$ is the solution vector which need to be solved by the finite element method.

Two forms of the gradient-operators are introduced. One is the spacial gradient for the current frame and the other is the material gradient for the reference frame.

$$\nabla(\cdot) = \frac{\partial \cdot}{\partial \mathbf{x}} E_r \frac{\partial(\cdot)}{\partial r} + E_\theta \frac{\partial(\cdot)}{\partial \theta} + E_z \frac{\partial(\cdot)}{\partial z} \qquad \text{for the spacial frame} \tag{2.52a}$$

$$\boldsymbol{\nabla}(\cdot) = \frac{\partial \cdot}{\partial \mathbf{X}} E_R \frac{\partial(\cdot)}{\partial R} + E_\Theta \frac{\partial(\cdot)}{\partial \Theta} + E_Z \frac{\partial(\cdot)}{\partial Z} \qquad \text{for the material frame,} \tag{2.52b}$$

here, $(\cdot)$ represents an arbitrary diffentiable variable.

The deformation gradient

The deformation gradient $\mathbf{F}$ is introduced with the general property of mapping tensors form the reference configuration to the current configuration. It has the from of a non symmetric second-order tensor. For body changes of a line, the deformation gradient $\mathbf{F}$ has the property to map a infinitesimal line element dX from the initial configuration to a infinitesimal line element dx in the current configuration: $\mathbf{F} := d\mathbf{X} \rightarrow d\mathbf{x}$

$$\mathbf{F} = \frac{\partial \mathbf{x}(\mathbf{X}, t)}{\partial \mathbf{X}} = \frac{\partial(\mathbf{X} + \mathbf{u})}{\partial \mathbf{X}} = \mathbf{I} + \frac{\partial \mathbf{u}(\mathbf{X}, t)}{\partial \mathbf{X}} = \mathbf{I} + \boldsymbol{\nabla} \mathbf{X}, \tag{2.53}$$

with $\mathbf{I}$ as the second order identity tensor (see section A.2.2). A complete description of the deformation gradient in cylindrical coordinates can be found in section A.3.1.

The determinant of the deformation gradient is called the Jacobian-determinant $\mathbf{J}$ of the deformation. It has to be non-singular and positive, to preserve the orientation.

$$\mathbf{J} := det\mathbf{F} > 0 \tag{2.54}$$

The Jacobi-determinant can map a infinitesimal surface element dA from the current configuration to the reference configuration dA_0 and vice versa:

$$d\mathbf{A}\mathbf{n} = d\mathbf{x} \times d\mathbf{y} = (\mathbf{F}d\mathbf{X}) \times (\mathbf{F}d\mathbf{Y}) = (\underbrace{\mathbf{J}}_{det\mathbf{F}} \mathbf{F}^{-T})(d\mathbf{X} \times d\mathbf{Y}) = (\mathbf{J}\mathbf{F}^{-T}) d\mathbf{A}_0 \mathbf{n}_0, \tag{2.55}$$

here, $\mathbf{n} = \dfrac{d\mathbf{x} \times d\mathbf{y}}{\parallel d\mathbf{x} \times d\mathbf{y} \parallel}$ and $\mathbf{n}_0 = \dfrac{d\mathbf{X} \times d\mathbf{Y}}{\parallel d\mathbf{X} \times d\mathbf{Y} \parallel}$ are the unit normal vector pointing from a surface element $\mathbf{A}$ and $\mathbf{A}_0$ in outward direction from its surface for the spacial and material version, respectively and $|| \cdot ||$ is the $L^2 - norm$.

The Jacobian-determinant can be further used for mapping a volume element dV from the current to the reference configuration dV_0 and vice versa:

$$d\mathbf{V} = (d\mathbf{x} \times d\mathbf{y}) \cdot dz = (\mathbf{F}d\mathbf{X}) \times (\mathbf{F}d\mathbf{Y}) \cdot \mathbf{F}d\mathbf{Z} = \mathbf{J}\underbrace{(d\mathbf{X} \times d\mathbf{Y}) \cdot d\mathbf{Z}}_{d\mathbf{V}_0}$$

$$\Rightarrow \frac{\mathrm{d}V}{\mathrm{d}V_0} = \frac{\rho_0}{\rho} = det(\mathbf{F}) = \mathbf{J} \tag{2.56}$$

In the case of $J = 1$ the deformation state can be considered as incompressible.

Polar decomposition

By spliting $\mathbf{F}$ into a rotational part $\mathbf{R}$ and stretch part $\mathbf{U}$ and $\mathbf{V}$ for material and spatial frame respectively, it yields to:

$$\mathbf{F} = \mathbf{RU} = \mathbf{VR}. \tag{2.57}$$

This splinting is called the polar decomposition of the deformation gradient. $\mathbf{R}$ performs a rotation, while $\mathbf{U}$ and $\mathbf{V}$ lead to a stretch of the geometry.

The stretch is in general defined as the ratio of the current length and the initial length:

$$\lambda = \frac{L}{L_0} \tag{2.58}$$

The stretches λ_i in principle directions is defined as the ratio of a length element dl_i in the spacial frame with a length element dL_i in the material frame:

$$\lambda_i = \frac{dl_i}{dL_i} \tag{2.59}$$

This formulation can be extended to a change in volume by the ratio of the current volume and the initial volume:

$$\frac{V}{V}_0 = \lambda_1\lambda_2\lambda_3 \tag{2.60}$$

λ_1, λ_2 and λ_3 are the three eigenvalues of $\mathbf{U}$ and introduced as principal stretches.

The right Cauchy-Green deformation tensor $\mathbf{C}$ is defined by:

$$\mathbf{C} = \mathbf{F}^T\mathbf{F} \tag{2.61}$$

A fully description of $\mathbf{C}$ in cylindrical coordinates is found in section A.3.2. One useful property of the right Cauchy-Green deformation tensor is the determination of the deformation in the material frame without knowing the rotation. This is can be very helpful for stress determination in which only the deformation is required and not the rotation.

$$\mathbf{C} = \mathbf{U}^T \underbrace{\mathbf{R}^T \mathbf{R}}_{\mathbf{I}} \mathbf{U} = \mathbf{U}\mathbf{U} = \mathbf{U}^2 \tag{2.62}$$

$\mathbf{U}^T = \mathbf{U}$ since $\mathbf{U}$ is a symmetric matrix. Further $\mathbf{C}$ and $\mathbf{U}$ can be expressed as:

$$\mathbf{C} = \sum_{i=1}^{3} \lambda_i^2 \, \mathbf{N}_i \otimes \mathbf{N}_i; \qquad \mathbf{U} = \sum_{i=1}^{3} \lambda_i \, \mathbf{N}_i \otimes \mathbf{N}_i \tag{2.63}$$

with, the eigenvectors N_1, N_2 and N_3 of $\mathbf{C}$ in the principle directions and their corresponding eigenvalues λ_1, λ_2 and λ_3, respectively. The tensor product $\otimes$ is expalined in section A.3.7.

The left Cauchy-Green deformation tensor $\mathbf{B}$ can be used for the determination of the deformation in the spacial frame without knowing the rotation.

$$\mathbf{B} = \mathbf{F}\mathbf{F}^T \tag{2.64}$$

$$\mathbf{B} = \mathbf{V} \underbrace{\mathbf{R}^T \mathbf{R}}_{\mathbf{I}} \mathbf{V}^T = \mathbf{V}\mathbf{V} = \mathbf{V}^2 \tag{2.65}$$

as in the case of $\mathbf{U}$ also $\mathbf{V}^T = \mathbf{V}$ since $\mathbf{V}$ is a symmetric matrix. Finally, $\mathbf{B}$ and $\mathbf{V}$ can be expressed as:

$$\mathbf{B} = \sum_{i=1}^{3} \bar{\lambda}_i^2 \, \mathbf{n}_i \otimes \mathbf{n}_i; \qquad \mathbf{V} = \sum_{i=1}^{3} \bar{\lambda}_i \, \mathbf{n}_i \otimes \mathbf{n}_i = \sum_{i=1}^{3} \lambda_i \, (\mathbf{R}\mathbf{N}_i) \otimes (\mathbf{R}\mathbf{N}_i) \tag{2.66}$$

with, the eigenvectors n_1, n_2 and n_3 of $\mathbf{B}$ in the principle directions and their corresponding eigenvalues $\bar{\lambda}_1, \bar{\lambda}_2$ and $\bar{\lambda}_3$, respectively. The eigenvectors and eigenvalues exhibit the following relation:

$$\bar{\lambda}_i = \lambda_i; \qquad \mathbf{n}_i = \mathbf{R}\mathbf{N}_i; \qquad \text{with i=1,2,3} \tag{2.67}$$

The rotational part $\mathbf{R}$ rotates N_1, N_2 and N_3 into n_1, n_2 and n_3, respectively.

The strain tensor

The engineering strain (Cauchy strain) in general is defined as relative change in length L of a body:

$$\epsilon = \frac{\Delta L}{L_0}. \tag{2.68}$$

Here, the ΔL is used for an absolute change in the length $L - L_0$ and L_0 is the initial length. The true strain ϵ_{true} can be defined with the stretch λ:

$$\epsilon_{true} = \log \frac{L}{L_0} = \log \lambda. \tag{2.69}$$

For a three dimensional disc, as used in the present model, the strain becomes a second order tensor with cylindrical coordinates.

$$\epsilon = \begin{bmatrix} \epsilon_{rr} & \epsilon_{r\theta} & \epsilon_{rz} \\ \epsilon_{\theta r} & \epsilon_{\theta\theta} & \epsilon_{\theta z} \\ \epsilon_{zr} & \epsilon_{z\theta} & \epsilon_{zz} \end{bmatrix}. \tag{2.70}$$

The components $\epsilon_{r\theta}$ and $\epsilon_{z\theta}$ are zero due to the axisymmetry and equation 2.70 reduces to:

$$\epsilon = \begin{bmatrix} \epsilon_{rr} & 0 & \epsilon_{rz} \\ 0 & \epsilon_{\theta\theta} & 0 \\ \epsilon_{zr} & 0 & \epsilon_{zz} \end{bmatrix}. \tag{2.71}$$

With $\gamma_{rz} = \epsilon_{rz} + \epsilon_{zr} = 2\epsilon_{rz}$ the stress tensor can be further reduced to a vector by Voigt's notation (see section A.3.3):

$$\epsilon = \begin{bmatrix} \epsilon_{rr} & \epsilon_{zz} & \epsilon_{\theta\theta} & \gamma_{rz} \end{bmatrix}^T \tag{2.72}$$

The Green-Lagrange strain tensor for material configuration is defined by:

$$\begin{aligned} \mathbf{E}_{GL} &= \frac{1}{2}\left(\mathbf{F}^T\mathbf{F} - \mathbf{I}\right) = \frac{1}{2}\left(\mathbf{C} - \mathbf{I}\right) = \frac{1}{2}\left(\mathbf{U}^2 - \mathbf{I}\right) = \sum_{i=1}^{3} \frac{1}{2}(\lambda_i^2 - 1)\, \mathbf{N}_i \otimes \mathbf{N}_i \\ &= \frac{1}{2}\left[(\boldsymbol{\nabla}\, \mathbf{u})^T + \boldsymbol{\nabla}\, \mathbf{u} + (\boldsymbol{\nabla}\, \mathbf{u})^T \ \boldsymbol{\nabla}\, \mathbf{u}\right]. \end{aligned} \tag{2.73}$$

For small stains the Green-Lagrange strain $\mathbf{E}_{GL}$ relaxes to the engineering strain ϵ:

$$\lim_{\boldsymbol{\nabla}\mathbf{u}\to 0} \mathbf{E}_{GL} := \epsilon = \frac{1}{2}\left[(\boldsymbol{\nabla}\, \mathbf{u})^T + \boldsymbol{\nabla}\, \mathbf{u}\right]. \tag{2.74}$$

The variation of the Green-Lagrange strain tensor reads

$$\delta\mathbf{E}_{GL} = \frac{1}{2}\delta\left(\mathbf{F}^T\mathbf{F} - \mathbf{I}\right) = \frac{1}{2}\left(\delta\mathbf{F}^T\mathbf{F} - \mathbf{F}^T\delta\mathbf{F}\right). \tag{2.75}$$

The Euler-Almansi strain tensor is defined in the spacial configuration:

$$\mathbf{E}_{EA} = \frac{1}{2}\left(\mathbf{I} - \left(\mathbf{F}\mathbf{F}^T\right)^{-1}\right) = \frac{1}{2}\mathbf{I} - \mathbf{B}^{-1} = \frac{1}{2}\mathbf{I} - \mathbf{V}^{-2} = \sum_{i=1}^{3} \frac{1}{2}(1 - \lambda_i^{-2})\, \mathbf{n}_i \otimes \mathbf{n}_i. \tag{2.76}$$

The thermal strain is defined by:

$$\mathbf{E_{th}} = \alpha_{\mathbf{th}}\theta_{th} \tag{2.77}$$

with $\theta_{th} = (T_l - T_{ref})$ is the difference between the current temperature T_l and the initial reference Temperature T_{ref} and $\alpha_{\mathbf{th}}$ is the thermal expansion tensor which is defined by:

$$\alpha_{\mathbf{th}} = \begin{bmatrix} \alpha_{th;rr} & \alpha_{th;rz} & \alpha_{th;r\theta} \\ \alpha_{th;\theta r} & \alpha_{th;\theta z} & \alpha_{th;\theta\theta} \\ \alpha_{th;zr} & \alpha_{th;zz} & \alpha_{th;z\theta}, \end{bmatrix} \tag{2.78}$$

or in Voigt's notation:

$$\alpha_{\mathbf{th}} = \begin{bmatrix} \alpha_R & \alpha_Z & \alpha_\Theta & \alpha_{RZ} \end{bmatrix}^T. \tag{2.79}$$

For a linear isotropic material the thermal strain can be written with the scalar thermal expansion coefficient α_{th}:

$$\mathbf{E_{th}} = \alpha_{th}\theta_{th} \begin{bmatrix} 1 & 1 & 1 & 0 \end{bmatrix}^T. \tag{2.80}$$

The volume change due to the thermal expansion can be calculated by:

$$V_{th} = (1 + \alpha_{th}(T - T_{ref}))^3. \tag{2.81}$$

Velocity, acceleration and rate of deformation

The velocity and acceleration can be derived from the first and second time derivative of the displacement field $\mathbf{u}(\mathbf{X}, t)$ at the position $\mathbf{x}$.

$$\mathbf{v}(\mathbf{X}, t) = \dot{\mathbf{u}}(\mathbf{X}, t) = \frac{\partial u(\mathbf{X}, t)}{\partial t} = \left.\frac{\partial \mathbf{u}(\mathbf{X}, t)}{\partial t}\right|_x \tag{2.82a}$$

$$\mathbf{a}(\mathbf{X}, t) = \dot{\mathbf{v}}(\mathbf{X}, t) = \frac{\partial^2 u(\mathbf{X}, t)}{\partial t^2} = \left.\frac{\partial^2 \mathbf{u}(\mathbf{X}, t)}{\partial t^2}\right|_x \tag{2.82b}$$

The rate of the materiel deformation can be expressed through the velocity gradient. The material velocity gradient can be written as the first time derivative of the deformation gradient.

$$\dot{\mathbf{F}} = \frac{\partial \mathbf{F}}{\partial t} = \frac{\partial \mathbf{x}}{\partial t} = \frac{\partial \mathbf{u}}{\partial t} = \nabla\dot{\mathbf{x}} = \nabla\dot{\mathbf{u}} \tag{2.83}$$

And the spacial velocity gradient has the form:

$$\mathbf{L} = \frac{\partial \mathbf{v}(\mathbf{x}, t)}{\partial x} = \boldsymbol{\nabla}\mathbf{v} = \dot{\mathbf{F}}\mathbf{F}^{-1} \tag{2.84}$$

with its decomposed form of the symmetric tensor $\mathbf{L}_D = sym(\mathbf{L})$ (rate of stretching tensor) and the skew-symmetric tensor $\mathbf{L}_W = skew(\mathbf{L})$ (rate of rotation):

$$\mathbf{L} = \mathbf{L}_D + \mathbf{L}_W = \frac{1}{2}\left(\mathbf{L} + \mathbf{L}^T\right) + \frac{1}{2}\left(\mathbf{L} - \mathbf{L}^T\right) \tag{2.85}$$

The Green-Lagrange strain rate can be expressed as:

$$\dot{\mathbf{E}}_{GL} = \mathbf{F}^T\, \mathbf{L}_D\, \mathbf{F} \tag{2.86}$$

The stress tensor

The Cauchy stress (true stress) in general can be considered as the internal resistance forces of a body resulting from a deformation. For a three dimensional disc, the stress can be expressed as a second order tensor in cylindrical coordinates. The first index is subjected to the force direction and the second index is subjected to the surface normal on which the force acts (figure 2.16).

$$\sigma = \begin{bmatrix} \sigma_{rr} & \sigma_{r\theta} & \sigma_{rz} \\ \sigma_{\theta r} & \sigma_{\theta\theta} & \sigma_{\theta z} \\ \sigma_{zr} & \sigma_{z\theta} & \sigma_{zz} \end{bmatrix} \tag{2.87}$$

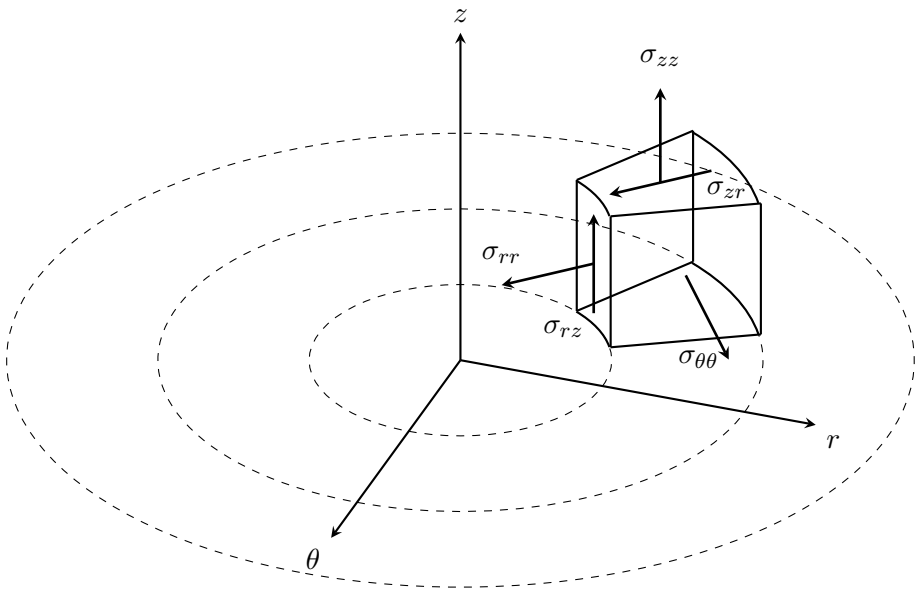

Figure 2.16.: Axisymmetric element for the illustration of the Cauchy stress components.

The components $\sigma_{r\theta}$, $\sigma_{\theta r}$, $\sigma_{z\theta}$ and $\sigma_{\theta z}$ are zero due to the axisymmetry and equation 2.87 reduces to:

$$\sigma = \begin{bmatrix} \sigma_{rr} & 0 & \sigma_{rz} \\ 0 & \sigma_{\theta\theta} & 0 \\ \sigma_{zr} & 0 & \sigma_{zz} \end{bmatrix} \tag{2.88}$$

with $\sigma_{rz} = \sigma_{zr}$ the stress tensor has only four independent components (see figure 2.16) and can be further reduced to a vector, according to Voigt's notation (see section A.3.3):

$$\sigma = \begin{bmatrix} \sigma_{rr} & \sigma_{zz} & \sigma_{\theta\theta} & \sigma_{rz} \end{bmatrix}^T \tag{2.89}$$

The traction vector $\mathbf{t}$ and $\mathbf{T}$ for the material and spacial frame can be defined as an infinitesimal force $d\mathbf{f}$ and $d\mathbf{F}$ per infinitesimal area $d\mathbf{A}$ and $d\mathbf{A}_0$ where the force is acting in the current configuration or initial configuration, respectively.

$$\mathbf{t}(\mathbf{r}, \theta, \mathbf{z}, \mathbf{n}, t) = \frac{d\mathbf{f}}{d\mathbf{A}} \tag{2.90a}$$

$$\mathbf{T}(\mathbf{R}, \boldsymbol{\Theta}, \mathbf{Z}, \mathbf{n}_0, t) = \frac{d\mathbf{F}}{d\mathbf{A}_0} \tag{2.90b}$$

here, $\mathbf{n}$ and $\mathbf{n}_0$ is the surface normal vector in the spacial and material configuration, respectively. Cauchy's theorem states a relation between the Cauchy stress tensor and the traction vector in the current configuration.

$$\mathbf{n} \cdot \sigma(\mathbf{r}, \theta, \mathbf{z}, t) = \mathbf{t}(\mathbf{r}, \theta, \mathbf{z}, t) \tag{2.91}$$

Subsequently, a formulation for the initial configuration can be established with the first Piola-Kirchhoff stress $\mathbf{P}$ (PK1).

$$\mathbf{n}_0 \cdot \mathbf{P}(\mathbf{R}, \boldsymbol{\Theta}, \mathbf{Z}, t) = \mathbf{T}(\mathbf{R}, \boldsymbol{\Theta}, \mathbf{Z}, t) \tag{2.92}$$

The Kirchhoff stress and the first and second Piola-Kirchhoff stress are introduced by:

$$\tau = J\sigma \qquad \text{Kirchhoff stress} \tag{2.93a}$$

$$\mathbf{P} = J\sigma\mathbf{F}^T \qquad 1^{st} \text{ Piola-Kirchhoff stress (nominal stress, PK1)} \tag{2.93b}$$

$$\mathbf{S} = J\mathbf{F}^{-1}\sigma\mathbf{F}^T \qquad 2^{st} \text{ Piola-Kirchhoff stress (material stress, PK2)} \tag{2.93c}$$

The Cauchy stress tensor can be easily transformed into the first and second Piola-Kirhoff stress by:

$$\sigma = J^{-1}\mathbf{P} = J^{-1}\mathbf{F}\mathbf{S}\mathbf{F}^T. \tag{2.94}$$

For a chosen stress measure, a particular strain measure has to be selected. These pairs are called energy-conjugated stress-strain pair and are listen in table 2.10.

Stress	Strain	Volume integration
σ	$\epsilon, \mathbf{E}_{EA}$	Spacial
τ	$\epsilon, \mathbf{E}_{EA}$	Matrial
$\mathbf{P}$	$\mathbf{F}$	Matrial
$\mathbf{S}$	$\mathbf{E}_{GL}$	Matrial

Table 2.10.: Energy-conjugated stress-strain pairs

2.7.2. Balance equations and equilibrium

The balance relation used in coniuum mechnics are the balance laws for mass, linear and angular momentum, energy and entropy.[100] The spacial form can be expressed as:

$$\begin{aligned}
\dot{\rho} + \rho \boldsymbol{\nabla} \dot{\mathbf{u}} = 0 \qquad & \text{Conservation of mass} \\
\rho \ddot{\mathbf{u}}(\mathbf{x}, t) - \nabla \cdot \sigma(\mathbf{x}, t) - \mathbf{f}_V(\mathbf{x}, t) = 0 \qquad & \text{Conservation of linear momentum} \\
\sigma = \sigma^T \qquad & \text{Conservation of angular momentum} \\
\rho \frac{\partial \mathbf{W}_{int}}{\partial t} = \sigma : \mathbf{L}_D - \boldsymbol{\nabla} \cdot \mathbf{q} + \rho \mathbf{Q} \qquad & \text{Conservation of energy.}
\end{aligned} \tag{2.95}$$

The material form then reads:

$$\begin{aligned}
\dot{\rho}_0 = 0 \qquad & \text{Conservation of mass} \\
\rho_0 \ddot{\mathbf{u}}(\mathbf{X}, t) - \boldsymbol{\nabla} \cdot \mathbf{P}(\mathbf{X}, t) - \mathbf{F}_V(\mathbf{X}, t) = 0 \qquad & \text{Conservation of linear momentum} \\
\mathbf{S} = \mathbf{S}^T \qquad & \text{Conservation of angular momentum} \\
\rho_0 \frac{\partial \mathbf{W}_{int}}{\partial t} = \mathbf{S} : \dot{\mathbf{E}}_{GL} - \boldsymbol{\nabla} \cdot \mathbf{q}_0 + \rho_0 \mathbf{Q} \qquad & \text{Conservation of energy.}
\end{aligned} \tag{2.96}$$

For an elasto-plastic material, the deformation state is irreversible due to energy dissipation and the Clausius-Duhem inequality is introduced:

$$\sigma : \mathbf{L}_D - \rho \left(\dot{\psi} + \dot{T} \eta \right) - \frac{\mathbf{q}}{T} \boldsymbol{\nabla} T \geq 0, \tag{2.97}$$

here, η is the specific entropy per unit mass and ψ is the Helmholtz free energy. Equation 2.97 can also be written in a purely mechanical form by

$$\sigma : \mathbf{L}_D - \rho\, \dot{\psi} \geq 0. \tag{2.98}$$

The balance law for linear momentum was used to derive the master equation for the FEM formulation. It can be derived from Newton's second law with the material time derivative $\dot{\mathbf{L}}$ which is equal to all external forces $\mathbf{F}_{ext}$ acting onto a body. These external forces are the sum of the volume and surface forces.

$$\underbrace{\frac{d}{dt}\left[\int_{\Omega_0} \rho_0 \dot{\mathbf{u}}(\mathbf{X},t)\, dV_0\right]}_{\sum_{i=1}^{n} \dot{\mathbf{L}}} = \underbrace{\int_{\Omega_0} \mathbf{F}_V(\mathbf{X},t)\, dV_0 + \int_{\partial\Omega_0} \mathbf{T}(\mathbf{X},t)\, dA_0}_{\sum_{i=1}^{n} \mathbf{F}_{ext}}. \tag{2.99}$$

According to equation 2.92, the last therm is equal to the product of the the first Piola-Kirchhoff stress and the normal material vector $\mathbf{P} \cdot \mathbf{n}_0$. Then, the divergence theorem is applied:

$$\int_{\partial\Omega_0} \mathbf{T}(\mathbf{X},t)\, dA_0 = \int_{\partial\Omega_0} \mathbf{P}(\mathbf{X},t)\, \mathbf{n}_0\, dA_0 = \int_{\Omega_0} \nabla \cdot \mathbf{P}(\mathbf{X},t)\, dV_0. \tag{2.100}$$

Now, the global formulation of the Cauchy equation of equilibrium can be derived:

$$\int_{\Omega_0} \rho_0 \ddot{\mathbf{u}}(\mathbf{X},t)\, dV_0 - \int_{\Omega_0} \underbrace{\nabla \cdot \mathbf{P}(\mathbf{X},t)}_{\mathbf{T}(\mathbf{X},t)}\, dV_0 - \int_{\Omega_0} \mathbf{F}_V(\mathbf{X},t)\, dV_0 = 0. \tag{2.101}$$

Equation 2.101 must hold for any arbitrary dV_0. Thus, a local material form can be obtained together with a spacial form which can be derived in the same way:

$$\rho_0 \ddot{\mathbf{u}}(\mathbf{X},t) - \boldsymbol{\nabla} \cdot \mathbf{P}(\mathbf{X},t) - \mathbf{F}_V(\mathbf{X},t) = 0 \tag{2.102a}$$

$$\rho \ddot{\mathbf{u}}(\mathbf{x},t) - \nabla \cdot \sigma(\mathbf{x},t) - \mathbf{f}_V(\mathbf{x},t) = 0. \tag{2.102b}$$

2.7.3. Damping

A Rayleight damping model is introduced that is characterized by a velocity-dependent friction which was chosen to damp oscillations on the nanosecond time scale.[103] This model can be introduced by the equation of motion with a single degree of freedom:

$$m\ddot{u} + \underbrace{(\alpha_{dM} m + \beta_{dK} k)}_{c}\, \dot{u} + ku = f(t), \tag{2.103}$$

here, m ist the mass, u is the displacement, k is the stiffness, $f(t)$ is a time dependent external force and c is the damping coefficient. The so-called damping parameter α_{dM} and

β_{dK} was set to zero and 10^{12} $1/s$, respectively. The relative damping $\xi(\omega)$ is introduced to illustrate the effect on frequency damping:

$$\xi(\omega) = \frac{1}{2}\left(\frac{\alpha_{dM}}{\omega} + \beta_{dK}\omega\right). \tag{2.104}$$

Figure 2.17 shows the relative damping in dependence on the angular frequency ω for α_{dM}, β_{dK} and the sum of both. The relative damping for α_{dM} is characterized by high damping for low frequencies while the relative damping for β_{dK} predominantly affects higher frequencies. A superposition of both would lead to a damped frequency range in between. The present choice of parameters provides an efficient damping model for high frequencies, while low frequencies are able to occur. This allows a very realistic model of the material where the computational time consuming high frequencies vanishes within a certain time scale while the Mo-layer can still develop low frequency modes during the expansion as it is expected.

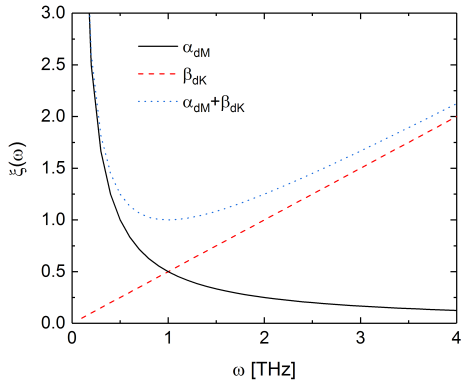

Figure 2.17.: Illustration of the relative damping in dependence on the angular frequency ω for α_{dM}, β_{dK} and the sum of both.

2.7.4. Thermal expansion at the phase transition

At the phase transition from solid to liquid, the molybdenum gets an additional volume change of ∼5 %, according to data of Hixson and Winkler.[71] This volume change occurs in a small temperature interval around the melting temperature. The direct implementation of this effect into a numerical model leads to volume expansion in a small spatial interval around the melt front. To avoid numerical instability and convergence problems the thermal strain is implemented in Comsol Multiphysics™ effectively by using a volume force model in which the expansion is smeared out over the whole melting zone. The melting zone is divided into two segments (rectangular in the axisymmetric projection). In the upper segment the force is adjusted in the direction to the glass and in the bottom segment the force is directed in the opposite direction. Equation 2.105 gives the magnitude of the volume forces, which cause a change of 5 % in the length and figure 2.18 shows the corresponding geometry. E is the Young's modulus of molybdenum and $z_m/2$ is the height of each segment.

$$\mathbf{F}_V = \pm \frac{2\frac{\Delta l}{l} E}{\frac{z_m}{2}} \tag{2.105}$$

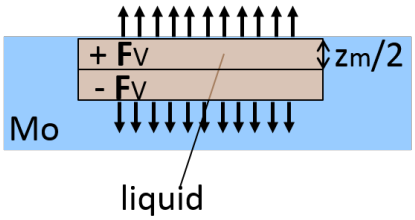

Figure 2.18.: The liquid area is divided in two segments, in which positive and negative volume forces are generated by the phase transition from solid to liquid.

2.7.5. Constitutive model

Equation 2.102a and 2.102b holds for any arbitrary material. Thus, a constitutive law has to be included which relates physical quantities with material parameters. Finally, the constitutive equations in combination with the kinematic relations and balance laws can give a complete desrciption of the mechanical motion and the deformation of the body. To finally solve equation 2.102a and 2.102b the stress has to be computed. For linear materials Hook's law as a tensor equation can be applied which relates the stress with the strain in a linear dependency through the 4^{th} order linear elastic material tensor $\mathbf{C}_{el}$.

$$\sigma = \mathbf{C}_{el} : \epsilon_{el} = \mathbf{C}_{el} : (\epsilon - \epsilon_{inel}) \tag{2.106}$$

here, (:) is the double dot tensor product (see section A.3.5). $\mathbf{C}_{el}$ exhibits the following symmetry property:

$$C_{el;ijkl} = C_{el;jikl} = C_{el;klij} \tag{2.107}$$

which yields to a reduction of maximum components from 81 to 21. For axisymmetric geometry Hook's law can be defined in the following form:

$$\begin{bmatrix} \sigma_{rr} \\ \sigma_{zz} \\ \sigma_{\theta\theta} \\ \tau_{rz} \end{bmatrix} = \mathbf{C_{el}} \begin{bmatrix} \epsilon_{rr} \\ \epsilon_{zz} \\ \epsilon_{\theta\theta} \\ \gamma_{rz} \end{bmatrix} \tag{2.108}$$

The Lamé constants λ and μ are introduced as material parameters to define the stiffness tensor $\mathbf{C}_{el}$:

$$\mathbf{C}_{el} = \lambda \mathbf{1} \otimes \mathbf{1} + 2\mu \mathbf{I}. \tag{2.109}$$

Here, $\mathbf{1}$ is the second-order identity tensor and $\mathbf{I}$ is the fourth-order identity tensor (see section A.2.2 and A.3.6).

The Lamé constants λ and μ can be expressed in terms of the Young's modulus E and the Poisson ratio ν and vice versa:

$$\lambda = \frac{E\nu}{(1+\nu)(1-2\nu)}; \qquad \mu = \frac{E}{2(1+\nu)};$$

$$E = \frac{\mu(3\lambda + 2\mu)}{\lambda + \mu}; \qquad \nu = \frac{\lambda}{2(\lambda + \mu)}. \tag{2.110}$$

.

Further, the shear modulus G and the bulk modulus K can be written as a function of E and ν:

$$G = \frac{E}{2(1+\nu)}; \qquad K = \frac{E}{3(1-2\nu)}. \tag{2.111}$$

.

For an isotropic material with an axisymmetric geometry, $\mathbf{C}_{el}$ can be reduced to a 4-by-4 matrix and the constitutive equation has the following form:

$$\underbrace{\begin{bmatrix} \sigma_{rr} \\ \sigma_{zz} \\ \sigma_{\theta\theta} \\ \tau_{rz} \end{bmatrix}}_{\sigma} = \underbrace{\left[\frac{E}{(1+\nu)(1-2\nu)}\right] \begin{bmatrix} 1-\nu & \nu & 0 & 0 \\ \nu & 1-\nu & 0 & 0 \\ 0 & 0 & 1-\nu & 0 \\ 0 & 0 & 0 & \dfrac{1-2\nu}{2} \end{bmatrix}}_{\mathbf{C}_{el}} \underbrace{\begin{bmatrix} \epsilon_{rr} \\ \epsilon_{zz} \\ \epsilon_{\theta\theta} \\ \gamma_{rz} \end{bmatrix}}_{\epsilon}. \tag{2.112}$$

The linear elastic material tensor $\mathbf{C}_{el}$ can be further decomposed into a deviatoric part $\mathbf{D}_d$ (volume preserving) and a volumetric part $\mathbf{D}_v$ (volume changing):

$$\mathbf{C}_{el} = \begin{bmatrix} \frac{4}{3}G+K & -\frac{2}{3}G+K & 0 & 0 \\ -\frac{2}{3}G+K & \frac{4}{3}G+K & 0 & 0 \\ 0 & 0 & \frac{4}{3}G+K & 0 \\ 0 & 0 & 0 & 2G+K \end{bmatrix}$$
$$= 2G \underbrace{\begin{bmatrix} \frac{1}{3} & -\frac{1}{3} & 0 & 0 \\ -\frac{1}{3} & \frac{2}{3} & 0 & 0 \\ 0 & 0 & \frac{2}{3} & 0 \\ 0 & 0 & 0 & 1 \end{bmatrix}}_{\mathbf{D}_d} + \underbrace{\begin{bmatrix} K & 0 & 0 & 0 \\ 0 & K & 0 & 0 \\ 0 & 0 & K & 0 \\ 0 & 0 & 0 & 0 \end{bmatrix}}_{\mathbf{D}_v} \tag{2.113}$$

which yields to:

$$\mathbf{C}_{el} = 2G\left(\mathbf{I} - \frac{1}{3}\mathbf{1}\otimes\mathbf{1}\right) + K\left(\mathbf{1}\otimes\mathbf{1}\right). \tag{2.114}$$

The material form (total Lagrangian formulation) of the constitutive equation can be written with the PK2 and the Green-Lagrange strain as corresponding conjugate stress-strain pairs.[104]

$$\mathbf{S} = \mathbf{C}_{el} : \mathbf{E}_{GL} \tag{2.115}$$

The thermal stress in the material frame can be written as:

$$\mathbf{S}_{th} = \mathbf{C}_{el} : \mathbf{E}_{th} \tag{2.116}$$

The Young's modulus E and the Poisson ratio ν are modeled as temperature dependent which is shown in figure 2.19. E decreases while ν increases from room temperature to the melting region. Thus, the bulk modulus is at a nearly constant value. Above the melting point, the Young's modulus becomes small, while the Poisson ratio approaches nearly 0.5. This approximation transforms the solid Mo into a liquid phase in the framework of continuum mechanics.

2.7.6. Plasticity

Uniaxial plasticity

The theroy for the plastic model used here can be found in many textbooks by e.g.[99,100]

The data for a plasticity model are normally obtained from the uniaxial tension experiment. In this experiment, typically a force is applied to the ends of a rod, while the change in length is measured. For plastic materials like ductile metals, this results in a stress strain curve with

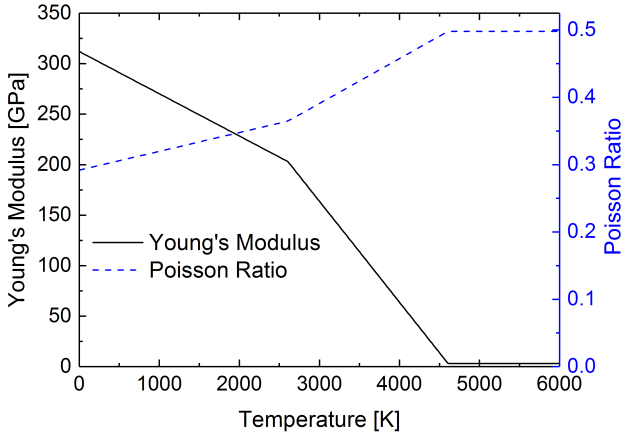

Figure 2.19.: Temperature-dependent Young's modulus and the Poisson ratio.[105]

an elastic and a plastic part (see figure 2.20). Uniaxial tension plasticity is described by an one dimensional model. The total strain ϵ can be obtained by the additive decomposition of the elastic strain ϵ_e and the plastic strain ϵ_p.

$$\epsilon = \epsilon_{el} + \epsilon_p \qquad \Leftrightarrow \qquad \epsilon_{el} = \epsilon - \epsilon_p \tag{2.117}$$

The constitutive law for the uniaxial stress can be defined as

$$\sigma = E\ \epsilon_{el} = E(\epsilon - \epsilon_p). \tag{2.118}$$

The yield function Φ is introduced to define the elasic domain $\mathcal{E}$:

$$\mathcal{E} = \{\sigma | \Phi(\sigma, \sigma_{ys}) < 0\} \qquad \text{with} \quad \Phi(\sigma, \sigma_{ys}) = |\sigma| - \sigma_{ys}. \tag{2.119}$$

The plastic flow rule determines whether the plastic strain rate $\dot{\epsilon}_p$ indicates stretching (positive) or compression (negative) which is the case under tensile stress (positive) or compressive stress (negative), respectively.

$$\dot{\epsilon}_p = \dot{\gamma} sgn(\sigma) \tag{2.120}$$

Here sgn is the signum function which is basically defined as $+1$ if the argument is greater or equal than zero and -1 if the argument is smaller than zero. The plastic multiplier is defined as a non negative scalar value $\dot{\gamma} \geq 0$ with the so-called complementary condition $\Phi\ \dot{\gamma} = 0$.

If the yield function Φ is smaller than zero, a purely elastic deformation state is considered. If the yield function is zero, then the yield stress level is reached and the deformation is considered as either elastic unloading or plastic loading. Stress values above the yield stress level are not admissible and the yield function do not exceed values greater than zero.

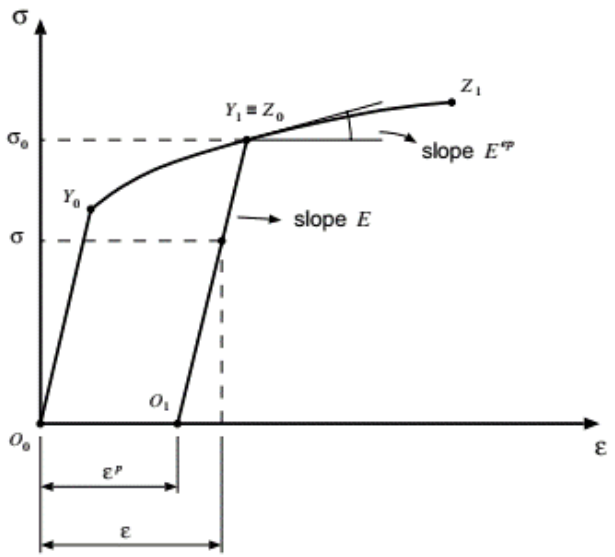

Figure 2.20.: A typical stress strain curve is illustrated with elastoplastic material behaviour. (Picture and caption obtained from Neto et. al.[100])

$$\Phi(\sigma,\sigma_{ys})\begin{cases} <0 & \Rightarrow \quad \dot{\gamma} = 0 \quad \Rightarrow \quad \dot{\epsilon}_p = 0 & \text{elastic} \\ =0 \begin{cases} & \Rightarrow \quad \dot{\gamma} = 0 \quad \Rightarrow \quad \dot{\epsilon}_p = 0 & \text{for elastic unloading} \\ & \Rightarrow \quad \dot{\gamma} \geq 0 \quad \Rightarrow \quad \dot{\epsilon}_p \neq 0 & \text{for plastic loading} \end{cases} \\ >0 & & \text{not admissible} \end{cases} \tag{2.121}$$

The loading/ unloading conditions for the occurence of platic flow (Karush-Kuhn-Tucker conditions)[106] are defined by:

$$\Phi(\sigma,\sigma_{ys}) \leq 0; \qquad \dot{\gamma} \geq 0; \qquad \Phi(\sigma,\sigma_{ys})\dot{\gamma} = 0. \tag{2.122}$$

The hardening law implies that the yield stress level σ_{ys} in equation 2.119 is a function of the accumulated axial plastic strain $\bar{\epsilon}_p$. The yield stress level σ_{ys} is the sum of an initial yield stress level σ_{ys0} and the isotropic hardening modulus σ_h.

$$\sigma_{ys} = \sigma_{ys}(\bar{\epsilon}_p) = \sigma_{ys0} + \sigma_h(\bar{\epsilon}_p). \tag{2.123}$$

The accumulated axial plastic strain $\bar{\epsilon}_p$ is defined by:

$$\bar{\epsilon}_p = \int_0^t |\dot{\epsilon}_p| dt; \qquad \frac{d\bar{\epsilon}_p}{dt} = \dot{\bar{\epsilon}}_p = |\dot{\epsilon}_p|; \qquad \dot{\bar{\epsilon}}_p = \dot{\gamma}. \tag{2.124}$$

During plastic flow $\dot{\gamma} \neq 0$ the consistency condition can be established:

$$\Phi = 0; \quad \Rightarrow \quad \dot{\Phi}\dot{\gamma} = 0 \quad \Rightarrow \quad \dot{\Phi} = 0. \tag{2.125}$$

The time derivative of the yield function in equation 2.119 can be derived from:

$$\dot{\Phi} = sgn(\sigma)\dot{\sigma} - H_T\dot{\bar{\epsilon}}_p, \qquad \text{with} \quad H_T = H_T(\bar{\epsilon}_p) = \frac{d\sigma_{ys}}{d\bar{\epsilon}_p}. \tag{2.126}$$

The stress rate in case of plastic yielding can be deduced with equation 2.125:

$$sgn(\sigma)\dot{\sigma} = H_T\dot{\bar{\epsilon}}_p \tag{2.127}$$

The plastic multiplier can now be derived from 2.118 and equation 2.127:

$$\dot{\gamma} = \frac{E}{E + H_T} sgn(\sigma)\dot{\epsilon} = \frac{E}{E + H_T}|\dot{\epsilon}| \tag{2.128}$$

The slope of the plastic regime in figure 2.20 can be expressed by the following stress strain relation ship:

$$\dot{\sigma} = E_{ep}\dot{\epsilon}. \tag{2.129}$$

The elastoplastic tangent modulus E_{ep} and hardening modulus H_T can be defined by combining equation 2.118, 2.120, 2.128 and 2.129.

$$E_{ep} = \frac{EH_T}{E + H_T}; \qquad H_T = \frac{E_{ep}}{1 - \dfrac{E_{ep}}{E}} \tag{2.130}$$

Three dimensional plasticity

For the three dimensional or multiaxial strained case the same additive decomposition was assumed than in the uniaxial case. This is a good assumption for small strains like in the present case. The stresses and strains are now replaced by tensors.

$$\begin{aligned} \epsilon &= \epsilon_e + \epsilon_p \\ \dot{\epsilon} &= \dot{\epsilon_e} + \dot{\epsilon_p} \end{aligned} \tag{2.131}$$

The free energy potential ψ is introduced as a function of the strain tensor ϵ, the plastic strain component ϵ_p and an internal hardening variable $\alpha = \{\bar{\epsilon}_p\}$.

$$\psi(\epsilon, \epsilon_p, \alpha) \tag{2.132}$$

The free energy can be splitted into an elastic component ψ_e which is the contribution to the elastic strain and a plastic component ψ_p which is dedicated to the hardening.

$$\psi(\epsilon, \epsilon_p, \alpha) = \psi_e \underbrace{(\epsilon - \epsilon_p)}_{\epsilon_{el}} + \psi_p(\alpha) \tag{2.133}$$

The purely mechanical Clausius–Duhem inequality 2.98 can than be splitted into an elastic and a plastic part.

$$\underbrace{\left(\sigma - \rho_0 \frac{\partial \psi_e}{\partial \epsilon_e}\right) : \dot{\epsilon}_e}_{elastic} + \underbrace{\sigma : \dot{\epsilon_p} - \mathbf{A}\dot{\alpha}}_{plastic} \geq 0 \qquad \text{with} \quad \mathbf{A} \equiv \rho_0 \frac{\partial \psi_p}{\partial \alpha} \tag{2.134}$$

$\mathbf{A}$ is a set of hardening thermodynamic forces. The so-called dissipation function Υ_p is formulated as:

$$\Upsilon_p(\sigma, \mathbf{A}, \dot{\epsilon}_p, \dot{\alpha}) \equiv \sigma : \dot{\epsilon}_p - \mathbf{A}\dot{\alpha} \geq 0. \tag{2.135}$$

In the case of an isotropic linear elastic material, the elastic contribution to the free energy ψ_e can be written based on the mechanical kinetic energy as:

$$\rho_0 \psi_e(\epsilon_e) = \frac{1}{2} \epsilon_e : \mathbf{C}_{el} : \epsilon_e = G\, \epsilon_{e;d} : \epsilon_{e;d} + \frac{1}{2} K (\epsilon_{e;v})^2 \tag{2.136}$$

where $\epsilon_{e;d}$ and $\epsilon_{e;v}$ are the deviatoric and volumetric part of the elastic strain. Now, the general stress strain law can be formulated by considering that the plastic contribution of equation 2.134 vanishes and the elastic contribution is set to zero.

$$\sigma = \rho_0 \frac{\partial \psi_e}{\partial \mathbf{E}_e} = \mathbf{C}_{el} : \epsilon_e = 2\, G\, \epsilon_{e;d} + K\, \epsilon_{e;v}\, \mathbf{I} \tag{2.137}$$

In the three dimensional case the plastic flow is initiated when the yield function Φ is zero.

$$\Phi(\sigma, \mathbf{A}) = 0 \tag{2.138}$$

The elastic domain $\mathcal{E}$ can then be defined such that the yield function is smaller than zero.

$$\mathcal{E} = \{\sigma | \Phi(\sigma, \mathbf{A}) < 0) \qquad \text{Elastic domain.} \tag{2.139}$$

A yield surface $\mathcal{Y}$ can be defined when the yield function is zero:

$$\mathcal{Y} = \{\sigma | \Phi(\sigma, \mathbf{A}) = 0) \qquad \text{Yield surfac} \tag{2.140}$$

The internal parameter for the plastic flow rule and the hardening law need to be defined:

$$\begin{aligned} \dot{\epsilon}_p &= \dot{\gamma}\,\mathbf{N}; & \mathbf{N} &= \mathbf{N}(\sigma, \mathbf{A}) \\ \dot{\alpha} &= \dot{\gamma}\,\mathbf{H}; & \mathbf{H} &= \mathbf{H}(\sigma, \mathbf{A}), \end{aligned} \tag{2.141}$$

with the flow vector $\mathbf{N}$ and the generalised hardening modulus $\mathbf{H}$. The loading/ unloading conditions for the occurence of platic flow (Karush-Kuhn-Tucker conditions)[106] are defined identical to the uniaxial case:

$$\Phi \leq 0; \qquad \dot{\gamma} \geq 0; \qquad \Phi\dot{\gamma} = 0. \tag{2.142}$$

The plastic flow rule can also be defined by a so-called flow potential $\mathbf{\Psi}$:

$$\mathbf{\Psi} = \mathbf{\Psi}(\sigma, \mathbf{A}); \tag{2.143}$$

both, the flow vector $\mathbf{N}$ and the hardening modulus $\mathbf{H}$ may than be derived from this potential:

$$\mathbf{N} \equiv \frac{\partial \mathbf{\Psi}}{\partial \sigma}; \qquad \mathbf{H} \equiv \frac{\partial \mathbf{\Psi}}{\partial \mathbf{A}}. \tag{2.144}$$

To satisfy the dissipation inequality 2.135, the requirements for the flow potential $\mathbf{\Psi}$ are that it is a non-negative convex function of σ and $\mathbf{A}$ with zero values at the origin:

$$\mathbf{\Psi}(\sigma = \mathbf{0}, \mathbf{A} = \mathbf{0}) = 0 \tag{2.145}$$

For the present model the same yield function $\mathbf{\Phi}$ and flow potential $\mathbf{\Psi}$ can be assumed:

$$\mathbf{\Psi} \equiv \mathbf{\Phi} \tag{2.146}$$

The determination of the plastic multiplier can be achieved by the so-called additional complementarity equation and the consistency condition:

$$\dot{\Phi}\,\dot{\gamma} = 0; \qquad \dot{\Phi} = 0. \tag{2.147}$$

In case of plastic yielding ($\dot{\gamma} \neq 0$) the time derivative of the yield function can be written as:

$$\dot{\Phi} = \frac{\partial \Phi}{\partial \sigma} : \dot{\sigma} + \frac{\partial \Phi}{\partial \mathbf{A}} : \dot{\mathbf{A}}. \tag{2.148}$$

By insertin the stress-strain rate relationship,

$$\dot{\sigma} = \mathbf{C}_{el} : (\dot{\epsilon} - \dot{\epsilon}_p) = \mathbf{C}_{el} : (\dot{\epsilon} - \dot{\gamma}\,\mathbf{N}) \tag{2.149}$$

into equation 2.148 the time derivative of the the yield function reads:

$$\begin{aligned}\dot{\Phi} &= \frac{\partial \Phi}{\partial \sigma} : \mathbf{C}_{el} : (\dot{\epsilon} - \dot{\epsilon}_p) + \frac{\partial \Phi}{\partial \mathbf{A}} * \rho_0 \frac{\partial^2 \Psi_p}{\partial \alpha^2} * \dot{\alpha} \\ &= \frac{\partial \Phi}{\partial \sigma} : \mathbf{C}_{el} : (\dot{\epsilon} - \dot{\gamma}\,\mathbf{N}) + \frac{\partial \Phi}{\partial \mathbf{A}} * \rho_0 \frac{\partial^2 \Psi_p}{\partial \alpha^2} * \mathbf{H}.\end{aligned} \tag{2.150}$$

The plastic multiplier can be established by rearranging the above equation:

$$\dot{\gamma} = \frac{\dfrac{\partial \Phi}{\partial \sigma} : \mathbf{C}_{el} : \dot{\epsilon}}{\dfrac{\partial \Phi}{\partial \sigma} : \mathbf{C}_{el} : \mathbf{N} - \dfrac{\partial \Phi}{\partial \mathbf{A}} * \rho_0 \dfrac{\partial^2 \Psi_p}{\partial \alpha^2} * \mathbf{H}} \tag{2.151}$$

During purely elastic deformation, the stress rate can be computed with the elastoplastic stiffness tensor $\mathbf{C}_{el}$:

$$\dot{\sigma} = \mathbf{C}_{el} : \dot{\epsilon} \tag{2.152}$$

During plastic flow, the stress rate can be computed with the elastoplastic stiffness tensor $\mathbf{C}_{ep}$:

$$\dot{\sigma} = \mathbf{C}_{el} : (\dot{\epsilon} - \dot{\epsilon}_p) = \mathbf{C}_{ep} : \dot{\epsilon}, \tag{2.153}$$

which can be written as:

$$\mathbf{C}_{ep} = \mathbf{C}_{el} - \frac{(\mathbf{C}_{el} : \mathbf{N}) \otimes \left(\mathbf{C}_{el} : \dfrac{\partial \Phi}{\partial \sigma} \right)}{\dfrac{\partial \Phi}{\partial \sigma} : \mathbf{C}_{el} : \mathbf{N} - \dfrac{\partial \Phi}{\partial \mathbf{A}} * \rho_0 \dfrac{\partial^2 \Psi_p}{\partial \alpha^2} * \mathbf{H}} \tag{2.154}$$

here $\dot{\epsilon}_p$ is substituted with equation 2.141 and with the plastic multiplier of equation 2.151.

Von Mises plasticity with kinematic hardening

In the present model von Mises plasticity with kinematic hardening was applied to the elasto-plastic material model. In the plastic regime, σ depends linearly on ϵ, but the strain freezes with an isotropic hardening model. Since σ increases only weakly in the plastic regime, the strain is considered as the quantity to monitor shearing. This kinematic, plastic material model is a compromise between the need to have stress in the vertical direction and the need to have stress relaxation in the radial direction.

The von Mises yield criterion is defines when plastic yielding is initiated by a critical value of the so-called J_2 stress deviator invariant:[107]

$$\Phi(\sigma) = \sqrt{3\ J_2(\mathbf{s}(\sigma))} - \sigma_{ys}. \tag{2.155}$$

Kinematic hardening is characterized by a resistance to plastic yielding in the opposite direction to prior loading. The yield function for kinematic hardening is defined by the relative stress tensor η which is defined by the difference of the stress deviator $\mathbf{s}$ and the so-called back-stress tensor β:

$$\Phi(\sigma,\beta) = \underbrace{\sqrt{3\ J_2(\eta(\sigma,\beta))}}_{\sigma_{mises}} - \sigma_{ys}; \qquad \text{with} \quad \eta(\sigma,\beta) \equiv \mathbf{s}(\sigma) - \beta; \qquad \mathbf{s}(\sigma) = \sigma - \frac{1}{3} tr\sigma \mathbf{1} \tag{2.156}$$

here, σ_{ys} is the yield stress level. The plastic flow rule for kinematic hardening is defined by the flow vector and the plastic strain rate:

$$\begin{aligned} \mathbf{N} &\equiv \frac{\partial \Phi}{\partial \sigma} = \sqrt{\frac{3}{2}} \frac{\eta}{||\eta||} \\ \dot{\epsilon_p} &= \dot{\gamma}\, \mathbf{N} = \dot{\gamma} \sqrt{\frac{3}{2}} \frac{\eta}{||\eta||} \end{aligned} \tag{2.157a}$$

The back stress in linear kinematic hardening can be assumed as:[108]

$$\dot{\beta} = \frac{2}{3} H_T \dot{\epsilon_p} = \dot{\gamma} \sqrt{\frac{2}{3}} H_T \frac{\eta}{||\eta||} \tag{2.158}$$

A plastic deformation model was used when the von Mises stress σ_{mises} initially exceeded a yield stress level σ_{ys0}. The yield stress level was set to 300 MPa only for the solid molybdenum. No plasticity appeared in the liquid phase. The yield stress function σ_{ys} is defined by the sum of the initial yield stress function σ_{ys0} and the kinematic hardening function σ_h.

$$\sigma_{ys}(\epsilon_{\mathbf{p}}) = \sigma_{ys0} + \underbrace{\frac{2}{3} \frac{\overbrace{E_{TKin}}^{\mathrm{H}_T}}{1 - \dfrac{E_{TKin}}{E}} \epsilon_{\mathbf{p}}}_{\sigma_h(\epsilon_{\mathbf{p}})} \qquad \text{for } \Phi(\sigma, \sigma_{ys}) = 0 \tag{2.159}$$

The plasitc strain variable ϵ_p is not directly accessible and the computation requires an iterative elastic predictor/plastic corrector return mapping algorithm.[109,110] All conditions for the rate independent associative linear kinematic hardening model with von Mises-yield criteria are summarized in table 2.11.

2.7.7. Stress-strain computation

An additive decomposition of the strain tensor was assumed which was proposed by Green and Naghdi.[111] For small strain but large deformation study, the Green-Lagrange strain tensor is

Condition	Function
1. Linear elastic law:	$\sigma = \mathbf{C}_{el} : \epsilon_{\mathbf{el}} = \mathbf{C}_{el} : (\epsilon - \epsilon_{\mathbf{pl}})$
2. Yield function:	$\begin{cases} \Phi(\sigma, \beta) = \sqrt{3\, J_2(\eta(\sigma, \beta))} - \sigma_{ys} \\ \eta(\sigma, \beta) \equiv s(\sigma) - \beta \end{cases}$
3. Plastic flow rule:	$\dot{\epsilon}_p = \dot{\gamma}\, \mathbf{N} = \dot{\gamma} \sqrt{\frac{2}{3}} \frac{\eta}{\|\|\eta\|\|}$
4. Hardening law:	$\dot{\beta} = \frac{2}{3} H_T \dot{\epsilon_p} = \dot{\gamma} \sqrt{\frac{2}{3}} H_T \frac{\eta}{\|\|\eta\|\|}$
5. Kuhn-Tucker conditions:	$\Phi(\sigma, \sigma_{ys}) \leq 0; \qquad \dot{\gamma} \geq 0; \qquad \Phi(\sigma, \sigma_{ys}) \dot{\gamma} = 0$

Table 2.11.: Conditions for the rate independent associative linear kinematic hardening model with von Mises-yield criteria

applied and splitted into the sum of an elastic and an inelastic component which is the sum of the plastic and the thermal strain, respectively.

$$\begin{aligned} \mathbf{E}_{GL} &= \mathbf{E}_{el} + \underbrace{\mathbf{E}_{th} + \mathbf{E}_{pl}}_{\mathbf{E}_{inel}} \\ \mathbf{E}_{el} &= \mathbf{E}_{GL} - \underbrace{\mathbf{E}_{th} - \mathbf{E}_{pl}}_{\mathbf{E}_{inel}} \end{aligned} \tag{2.160}$$

For extension of finite strain elastoplasticity the interested reader is referred to further literature.[112, 113] This approach is based on multiplicative decomposition of the deformation gradient:

$$\mathbf{F} = \mathbf{F}_e\, \mathbf{F}_{pl}\, \mathbf{F}_{th} \tag{2.161}$$

Since in the present work large displacements and small strains are expected, the engineering stress σ and strain ϵ were substituted by the energy conjugated second Piola-Kirchhoff stress $\mathbf{S}$ and the Green-Lagrange strain $\mathbf{E}_{GL}$, respectively. As mentioned in section c the Mo liquifies above the melting point. The liquid phase is implemented through the elastic constants in the mechanical constivitive model in section 2.7.5. Part of the domain is formed into a liquid like Mo-phase by modifying the Poisson's ratio to values close to 0.5. This may results in numerical instabilities because the trace of the strain in the liquid Mo-phase vanishes. A nearly incompresible approach was necessary to avoid numerical instabilities. The software Comsol Multiphysics™ uses a mixed formulation for the nearly incompressible approach, where the pressure is implemented as a new dependent variable.[101] The final stress strain relation for a nearly incompressible material reads:[101]

$$\mathbf{S} = \mathbf{D}_d : (\mathbf{E}_{GL} - \mathbf{E}_p - \mathbf{E}_{th}) - \mathbf{D}_v : \mathbf{pI}$$
$$\mathbf{S} = \mathbf{D}_d : (\mathbf{E}_{GL} - \mathbf{E}_p - \mathbf{E}_{th}) - \left(\frac{1}{3} tr(\mathbf{D}_v : \mathbf{E}_{GL} - \mathbf{E}_{th})\right) \mathbf{I} \tag{2.162}$$

As mentioned before, the implementation of the plasticity model is may obtained by an Euler time discretization of the plastic strain rate and a solution scheme of a elastic predictor/plastic corrector algorithm with a return mapping algorithm. For more details on this method the interested reader is referred to e.g.[100]

2.7.8. Finite element formulation

In this section the equation for solving the deformation is presented with the necessary boundary conditions. The three forms of boundary conditions are called Dirichlet, Neumann and mixed boundary condition. The Dirichlet boundary condition prescribes the displacement, while the Neumann boundary condition specifies the traction vector. All equations are presented in the strong form first as a so-called boundary value problem:

$$\rho \ddot{\mathbf{u}} = \nabla \cdot \sigma + \mathbf{F_v} \qquad \text{on } \Omega \tag{2.163a}$$
$$\mathbf{u} = \tilde{\mathbf{u}} \qquad \text{on } \partial\Omega_D \quad \text{(Dirichlet B.C.)} \tag{2.163b}$$
$$\mathbf{t} = \sigma \mathbf{n} = \tilde{\mathbf{t}} \qquad \text{on } \partial\Omega_N \quad \text{(Neumann B.C.)} \tag{2.163c}$$

Equation 2.163a is a hyperbolic PDE known as the balacne of linear momentum (equation 2.102a). Equation 2.163b and 2.163c are the Dirichlet and Neumann boundary condition, respectively.

The weak form of equation 2.163a is obtained by appling the principle of virtual work.[97,114] In a first step the spacial description is introduced:

$$\delta W(\mathbf{u}, \delta\mathbf{u}) = \int_{\Omega_0} (\rho_0 \ddot{\mathbf{u}} - \nabla \cdot \sigma - \mathbf{F}_V)\, \delta\mathbf{u}^T \, \mathrm{d}V_0 = 0 \tag{2.164}$$

here, $\delta\mathbf{u}$ is the test function $\mathbf{v}$ which is the so-called virtual displacement. This function has to be smooth and zero at the boundary surfaces $\partial\Omega$. The final weak form can be derived from equations 2.164 by using integration by parts and the divergence theorem (see section A.3.8):

$$\int_\Omega \left(\rho\ \ddot{\mathbf{u}}\ \delta\mathbf{u}^T - \nabla\cdot\sigma\ \delta\mathbf{u} - \mathbf{F}_V\delta\mathbf{u}\right)\ \mathrm{d}V = 0$$

$$\int_\Omega \left(\rho\ddot{\mathbf{u}}\delta\mathbf{u} - \nabla\cdot(\sigma\delta\mathbf{u}) + \sigma : \nabla\delta\mathbf{u} - \mathbf{F}_V\delta\mathbf{u}\right)\ \mathrm{d}V = 0$$

$$\int_\Omega \rho\ddot{\mathbf{u}}\delta\mathbf{u}\ \mathrm{d}V + \int_\Omega \sigma : \nabla\delta\mathbf{u}\ \mathrm{d}V - \int_\Omega \mathbf{F}_V\delta\mathbf{u}\ \mathrm{d}V - \int_{\delta\Omega} \sigma\delta\mathbf{u}\cdot\mathbf{n}\ \mathrm{d}A = 0$$

$$\int_\Omega \rho\ddot{\mathbf{u}}\delta\mathbf{u}\ \mathrm{d}V + \int_\Omega \sigma : \nabla\delta\mathbf{u}\ \mathrm{d}V - \int_\Omega \mathbf{F}_V\delta\mathbf{u}\ \mathrm{d}V - \int_{\delta\Omega} \tilde{\mathbf{t}}\delta\mathbf{u}\cdot\mathbf{n}\ \mathrm{d}A = 0$$

$$\underbrace{\int_\Omega \rho\ddot{\mathbf{u}}\delta\mathbf{u}\ \mathrm{d}V}_{\delta W_{kin}} + \underbrace{\int_\Omega \sigma : \delta\epsilon\ \mathrm{d}V}_{\delta W_{int}} - \underbrace{\int_\Omega \mathbf{F}_V\delta\mathbf{u}\ \mathrm{d}V - \int_{\delta\Omega} \tilde{\mathbf{t}}\delta\mathbf{u}\cdot\mathbf{n}\ \mathrm{d}A}_{\delta W_{ext}} = 0. \tag{2.165}$$

The equation for virtual work can be divided into three sub-equations. It consists of a kinetic part δW_{kin} and internal part δW_{int} and an external part δW_{ext}. The kinetic part consists of virtual work done by inertia forces, the internal part consists of work done by internal forces and the external part consists of work done by volume and boundary forces. The internal virtual work is now transformed from the spacial to the material domain by

$$\begin{aligned}\int_\Omega \sigma : \nabla\delta\mathbf{u}\ \mathrm{d}V &= \int_\Omega (J\sigma) : \boldsymbol{\nabla}\delta\mathbf{u}\mathbf{F}^{-1}\ \mathrm{d}V = \int_\Omega \mathbf{P} : \delta\mathbf{F}\ \mathrm{d}V \\ &= \int_\Omega \mathbf{P} : \boldsymbol{\nabla}\mathbf{u}\ \mathrm{d}V = \int_{\Omega_0} \mathbf{FS} : \boldsymbol{\nabla}\mathbf{u}\ \mathrm{d}V_0.\end{aligned} \tag{2.166}$$

Similar, the inertia and the external vital work is transformed from the spacial into the material domain by:

$$\int_\Omega \mathbf{f_V}\delta\mathbf{u}\ \mathrm{d}V + \int_{\delta\Omega} \tilde{\mathbf{t}}\delta\mathbf{u}\ \mathrm{d}S = \int_{\Omega_0} \mathbf{F_V}\delta\mathbf{u}\ \mathrm{d}V_0 + \int_{\delta\Omega_0} \tilde{\mathbf{F}}\delta\mathbf{u}\ \mathrm{d}S_0 \tag{2.167a}$$

$$\int_\Omega \rho\ \ddot{\mathbf{u}}\mathrm{d}V = \int_{\Omega_0} \rho_0\ \ddot{\mathbf{u}}\ \mathrm{d}V_0 \tag{2.167b}$$

with the relation of the body force $\mathbf{f}_V = J^{-1}\mathbf{F}_V$, the volume change $\mathrm{d}V = J\mathrm{d}V_0$ and $\rho = J^{-1}\rho_0$. Consequently, the material form of equation 2.165 reads:

$$\underbrace{\int_{\Omega_0} \rho_0\ \ddot{\mathbf{u}}\ \delta\mathbf{u}\ \mathrm{d}V_0}_{\delta W_{kin}} + \underbrace{\int_{\Omega_0} \mathbf{S} : \delta\mathbf{E}_{GL}\ \mathrm{d}V_0}_{\delta W_{int}} - \underbrace{\int_{\Omega_0} \mathbf{F}_V\delta\mathbf{u}\ \mathrm{d}V_0 - \int_{\delta\Omega_0} \tilde{\mathbf{T}}\delta\mathbf{u}\ \mathrm{d}S_0}_{\delta W_{ext}} = 0 \tag{2.168}$$

with $\delta\mathbf{E}_{GL}$ as the the variation of the Green-Lagrange strain tensor which is obtained by equation 2.75.

To compute the solid and the liquid Mo-phase in the framework of continuum mechanics a mixed formulation is assumed for the nearly incompressible material.[101,115] This mixed formulation consists of two weak form equations. Besides the originally only independent displacement variable $\mathbf{u}$ with the virtual displacement $\delta\mathbf{u}$, the pressure $\mathbf{p}$ is now introduced as a second new independent variable with the virtual pressure $\delta\mathbf{p}$.

$$\underbrace{\int_{\Omega_0} \rho_0 \, \ddot{\mathbf{u}} \, \delta\mathbf{u} \, \mathrm{d}V_0}_{\delta W_{kin}} + \underbrace{\int_{\Omega_0} \mathbf{S}_d : \delta\mathbf{E} \, \mathrm{d}V_0 + \int_{\Omega_0} \mathbf{I}\mathbf{p} : \delta\mathbf{E}^T \, \mathrm{d}V_0}_{\delta W_{int}} - \underbrace{\int_{\Omega_0} \mathbf{F}_V \delta\mathbf{u} \, \mathrm{d}V_0 - \int_{\delta\Omega_0} \tilde{\mathbf{T}} \delta\mathbf{u} \, \mathrm{d}S_0}_{\delta W_{ext}} = 0 \tag{2.169a}$$

$$\underbrace{\int_{\Omega_0} \delta\mathbf{p} \left[\mathbf{I}^T\mathbf{E} - \frac{\mathbf{p}}{K} \right] \mathrm{d}V_0}_{\delta W_{int}} = 0 \tag{2.169b}$$

2.7.9. Mechanical boundary conditions and initial values

The mechanical boundary conditions (figure 2.21) are a crucial point of the model since it contains the interaction between the expanding Mo-layer and the glass substrate, in other words, the recoil pressure. It introduces the dependence of the ablation process on the substrate's elastic properties.

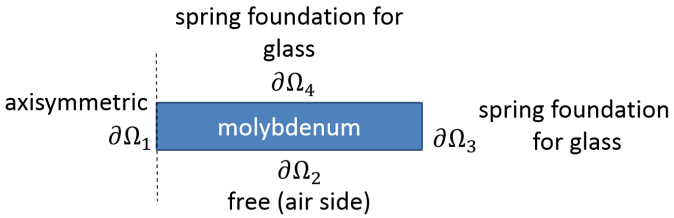

Figure 2.21.: Boundary conditions for the elasto-mechanical model.

Since the Young's modulus of the glass substrate is smaller than of the metal layer, the substrate can not be modeled as a rigid boundary condition and a shock-wave will not be reflected completely. The counteraction back from the substrate to the layer may be weak. The substrate in the boundary condition $\partial\Omega_4$ was chosen with a spring model where the parameters of mass, spring constant and damping constant were calibrated carefully. The spring model describes the response of the substrate to the layer material moving in substrate direction. The spring continuum obtains a value for deformation and velocity in every point along the boundary. A second spring model was used to describe the adhesion force of the layer outside the melt region. No further spring modeling was applied inside the melt region; the layer is allowed to move away, when the velocity is sufficient to overcome a possible potential energy barrier in the stressed layer.

B.c.	Displacement
$\partial\Omega_1$	Axisymmetric
$\partial\Omega_2$	Free
$\partial\Omega_3$	$\sigma\mathbf{n} = -\mathbf{k}_{Mo}\ (\mathbf{u} - \mathbf{u}_0)$
$\partial\Omega_4$	$\sigma\mathbf{n} = -\mathbf{k}_{glass}(\mathbf{u} - \mathbf{u}_0) - \mathbf{d}_{glass}\dfrac{\partial\mathbf{u}}{\partial t}$

Table 2.12.: Elasto-mechanical boundary conditions (b.c.)

The accuracy of the boundary condition $\partial\Omega_4$ had been confirmed by a variety of test calculations. Therefor $\partial\Omega_4$ was replaced by an extended domain which represented the glass substrate. Figure 2.22 illustrates the result from this prior simulations. The temperature rises with a step function from 0 to ∼4000 K in a time interval of about 50 ps which was very similar to the final simulation conditions. By comparing the displacement from point 1 and 2 of the spring boundary with the glass domain it turns out, that the deviations are very small. Thus, the spring boundary represent an excellent substitution for the glass domain in the thermal expansion model.

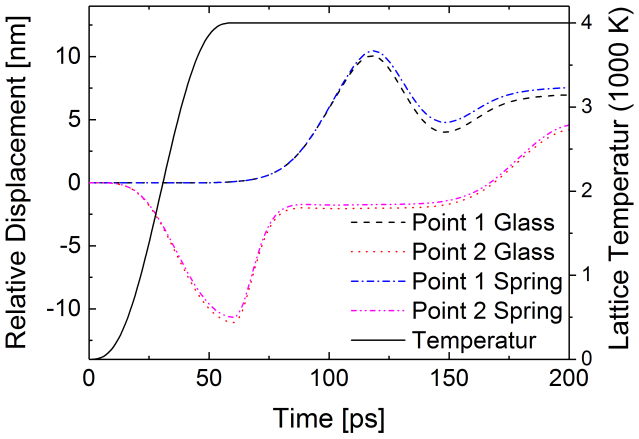

Figure 2.22.: Displacement of point 1 and 2 initiated by a temperature step function. The displacement is shown with a spring foundation boundary condition in comparison with an adjacent glass domain.

The mechanical boundary $\partial\Omega_3$ to the radial outside was also described by a spring model with the purpose to tolerate some radial deformation. $\partial\Omega_1$ and $\partial\Omega_2$ were modeled as axisymmetric and free, respectively. Table 2.12 summarizes all boundary conditions with the used values of table 2.13.

The complete boundary value problem requires the initial values of $\mathbf{u}$ and its first time derivative $\dot{\mathbf{u}}$ at time zero.

$$\mathbf{u}(t=0) = \mathbf{u}_0; \qquad \dot{\mathbf{u}}(t=0) = \dot{\mathbf{u}}_0 \tag{2.170}$$

Variable	Symbol	Value	Unit
Spring constant glass	k_{glass}	$1.6\ 10^{-6}$	N/m
Damping factor glass	d_{glass}	$1.5\ 10^{7}$	$Ns/(mm^2)$
Spring constant molybdenum	k_{Mo}	10^{18}	$Ns/(mm^2)$
External temperature	T_{ext}	293.14	K

Table 2.13.: Parameters for the boundary condition models

2.8. Space and time discretization

The FEM-equation 2.26, 2.43 and 2.169 are continuous in space and time. To make them numerically solvable a discretization is necessary. The following subsections show the space and time discretization, including the assembly, equation coupling and the numerical integration method.

2.8.1. Space discretisation

FEM is based on the concept to approximate a continuous solution of a PDE on a domain by an approximated discrete solution. For this reason, the complete material domain Ω_0 is divided into non overlapping subdomains $\Omega_{0;e}$ which consists of finite elements forming a mesh:

$$\Omega_0 \approx \Omega_{0;h} = \bigcup_{e=1}^{n_{el}} \Omega_{0;e}, \tag{2.171}$$

here, $\Omega_{0;h}$ is the approximated discrete version of Ω_0, n_{el} is the number of mesh elements in the domain Ω_0 and $\Omega_{0;e}$ is a set of element domains. The solution is computed only at discrete points, the so-called nodes on the finite elements by a set of algebraic finite element equations for a steady state problem and a set of ordinary differential equations for a transient problem. The discretization is explained in many FEM textbooks e.g.[97,115–117]

Thanks to the rectangular geometry of the cross section for the Mo-disc, the complete domain could be represented by a 2 dimensional mesh. All mesh elements were chosen to be rectangular. The advantage of rectangular elements is that they may improves convergence for a deformed mesh since the angle during deformation gets not such acute in comparison to triangular elements.[118] The mesh element size was decreased towards the center point to precisely resolve the strong physical gradients. For a fluence of 0.40 J/cm^2 the mesh consists of 2500 elements with an element ratio growth rate of 0.1 in axial and radial direction, shown in figure 2.23. For higher fluence of 0.50 J/cm^2 and 0.55 J/cm^2, the mesh was refined to 10,000 elements with the same element ratio.

Shape functions

Any dependent variable $\mathbf{u}(R, Z, t)$ and the weight function $\mathbf{v}(R, Z, t)$ can be approximated by a linear combination of functions $\Phi(R, Z)$ and $\Psi(R, Z)$ with coefficients $\mathbf{a}_i(t)$ and $\mathbf{b}_j$, respectively within one elements with n_{nodes} number of nodes, by

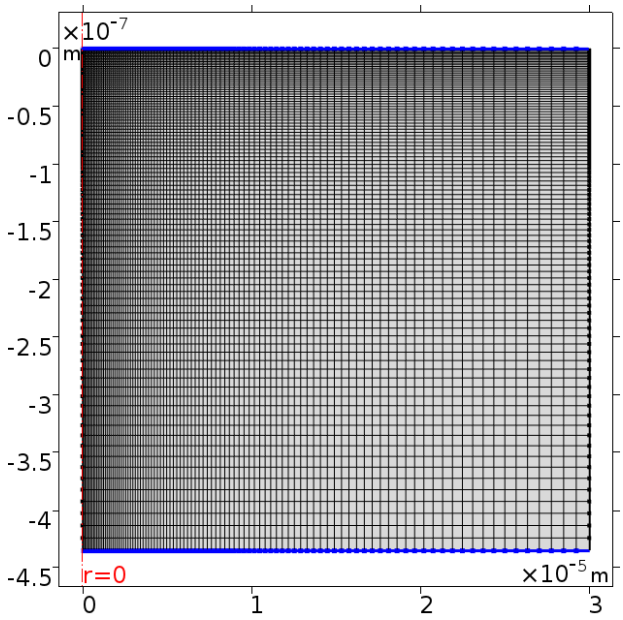

Figure 2.23.: The mesh for a fluence of 0.40 J/cm^2 with 2500 elements and an element ration growth rate of 0.1 in axial and radial direction, respectively. The aspect ratio is not preserved for better visibility such that it has equal length in vertical and horizontal direction.

$$\mathbf{u}(R,Z,t) \approx \mathbf{u}_h(R,Z,t) = \sum_{i=1}^{n_{nodes}} \Phi_i(R,Z)\,\mathbf{a}_i(t)$$
$$\mathbf{v}(R,Z) \approx \mathbf{v}_h(R,Z) = \sum_{j=1}^{n_{nodes}} \Psi_j(R,Z)\,\mathbf{b}_j. \tag{2.172}$$

A local coordinate system (R',Z') is introduced for each finite element of the mesh. The coordinate transformation can be achieved by:

$$R' = R - R_0; \qquad Z' = Z - Z_0, \tag{2.173}$$

here, the coordinate origin is located at the center of the element (R_0,Z_0) as shown in figure 2.24.

Accroding to the Galerkin method, the same function for the discretization may be used for the dependent variable $\mathbf{u}(R,Z,t)$ and the weight function $\mathbf{v}(R,Z)$.

$$\Phi(R,Z) = \Psi(R,Z) \tag{2.174}$$

A new coordinate system which is called the natural coordinate system (ξ,η) in the so called parent domain is introduced for the shape function. This approach has the advantage to map a shape function with triangular or quadratic shape to any arbitrary shape in the original coordinate system within the so called global domain where the geometry is defined. The coordinates $\mathbf{X}(\xi,\eta)$ and the dependent variable $\mathbf{u}(\xi,\eta)$ as well as the weight function

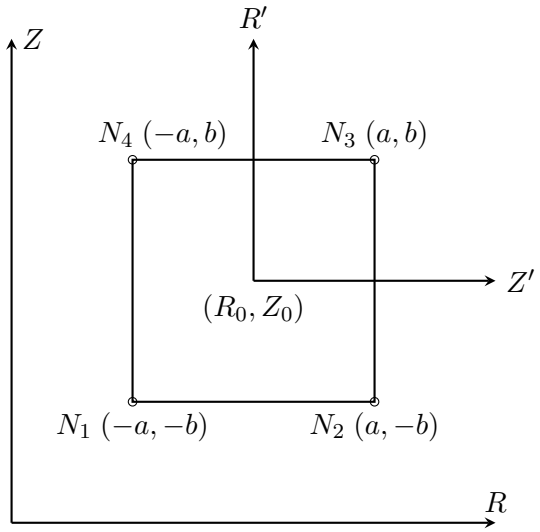

Figure 2.24.: Picture of linear quadrilateral element in the R-Z-plane. The coordinate R' and Z' are the local element coordinates, respectively. The four nodes are at the edges of the rectangle at node one (-a,-b), node two (a,-b), node three (a,b) and node four (-a,b).

$\mathbf{v}(\xi, \eta)$ may be transformed by a shape function within one finite element. If the same shape function $\mathbf{N}(\xi, \eta)$ is used for the coordinate and the field variable, the approach is called isoparametric.[119] If the shape functions are different than it is known as sub- or super-parametric formulation, depending on the order of interpolation function. The coordinate $\mathbf{X}(\xi, \eta)$, the displacement field $\mathbf{u}(\xi, \eta, t)$ and the weight function $\mathbf{v}(\xi, \eta, t)$ are defined within an arbitrary point of one finite element as a linear combination of shape functions $N_{i;e}$ at the node i with coefficients (R_i, Z_i), $(u_{i;r}, u_{i;z})$ and $(\tilde{v}_{j;r}, \tilde{v}_{j;z})$, respectively.

$$\mathbf{X}(\xi, \eta) \approx \begin{bmatrix} R(\xi, \eta) \\ Z(\xi, \eta) \end{bmatrix} = \sum_{i=1}^{n_{nodes}} \begin{bmatrix} R_i \\ Z_i \end{bmatrix} N_{i;e}(\xi, \eta) \tag{2.175}$$

$$\mathbf{u}(\xi, \eta, t) \approx \begin{bmatrix} u(\xi, \eta, t) \\ w(\xi, \eta, t) \end{bmatrix} = \sum_{i=1}^{n_{nodes}} \begin{bmatrix} u_{i;r}(t) \\ u_{i;z}(t) \end{bmatrix} N_{i;e}(\xi, \eta) \tag{2.176}$$

$$\mathbf{v}(\xi, \eta, t) \approx \begin{bmatrix} \tilde{v}(\xi, \eta, t) \\ \tilde{v}(\xi, \eta, t) \end{bmatrix} = \sum_{j=1}^{n_{nodes}} \begin{bmatrix} \tilde{v}_{j;r}(t) \\ \tilde{v}_{j;z}(t) \end{bmatrix} N_{j;e}(\xi, \eta) \tag{2.177}$$

The shape functions were chosen as Lagrangian and are defined in the form of polynomials:

$$N_{i;e}(\xi,\eta) = \sum_{i=1}^{n} \frac{1}{4}\,(1+\xi\xi_i)\,(1+\eta\eta_i)\,; \qquad \text{4-node linear} \tag{2.178}$$

$$N_{i;e}(\xi,\eta) = \sum_{i=1}^{n} \frac{1}{4}\,(1+\xi\xi_i)\,(1+\eta\eta_i)\,(\xi\xi_i+\eta_i\eta-1) \qquad \text{9-node quadratic,} \tag{2.179}$$

with $(\xi_i,\ \eta_i)$ denotes the natural coordinates at the node i which are defined in the range $(\pm 1,\ \pm 1)$. The linear and quadratic shape functions are listed in details in table 2.14.

In the present case, the form of isoparametric quadrilateral elements is always square with an edge length of two and the coordinate origin is in the center (see figure 2.25). Isoparametric mapping between the global and the natural coordinate system within one finite element is achieved by:

$$\begin{aligned} R = R(\xi,\eta) &= \sum_{i=1}^{n_{nodes}} R_i\ N_{i;e}(\xi,\eta) \\ Z = Z(\xi,\eta) &= \sum_{i=1}^{n_{nodes}} Z_i\ N_{i;e}(\xi,\eta). \end{aligned} \tag{2.180}$$

Then, an arbitrary function $f(R,Z)$ can be mapped from the global and the natural coordinate system by:

$$f(R,Z) = f\left(R(\xi,\eta), Z(\xi,\eta)\right) = \hat{f}(\xi,\eta). \tag{2.181}$$

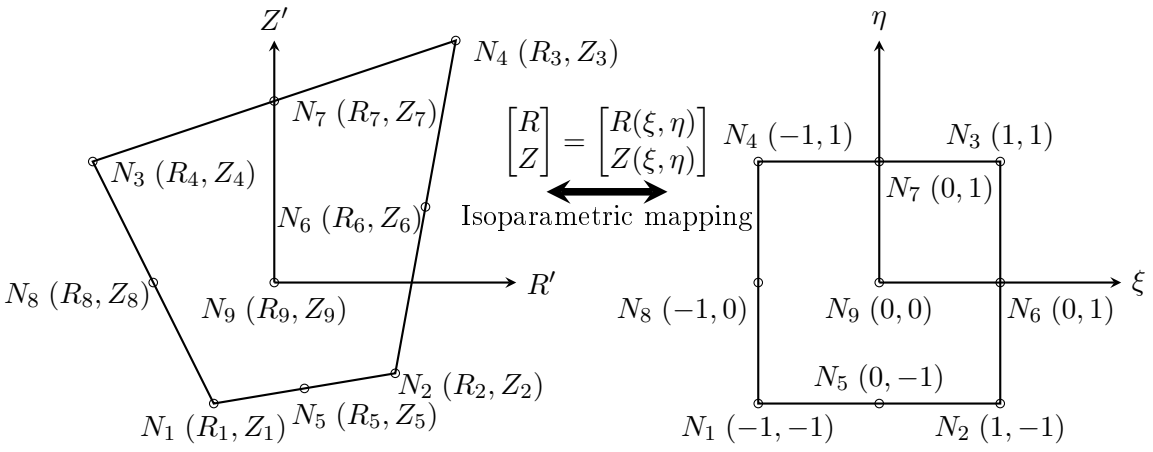

Figure 2.25.: Picture of a quadrilateral isoparametric Lagrangian element in the R'-Z'-plane which is isoparametrically mapped into the η-ξ-plane.

For the intensity and the temperature computation, the element-type was selected as second-order quadrilateral Lagrangian which consisted of nine nodes per element. The nodes are located at the element-vertexes, the midpoints of the edges and in the center. For the thermal expansion computation, the element-type was selected as first-order quadrilateral

linear	quadratic
	$N_1(\xi,\eta) = \frac{1}{4}(1-\xi)(1-\eta)\xi\eta$
	$N_2(\xi,\eta) = \frac{1}{4}(1+\xi)(-1+\eta)\xi\eta$
$N_1(\xi,\eta) = \frac{1}{4}(1-\xi)(1-\eta)$	$N_3(\xi,\eta) = \frac{1}{4}(-1+\xi)(1+\eta)\xi\eta$
$N_2(\xi,\eta) = \frac{1}{4}(1+\xi)(1-\eta)$	$N_4(\xi,\eta) = \frac{1}{4}(1+\xi)(1+\eta)\xi\eta$
$N_3(\xi,\eta) = \frac{1}{4}(1+\xi)(1+\eta)$	$N_2(\xi,\eta) = -\frac{1}{2}(-1+\xi)(1+\xi)(-1+\eta)\eta$
$N_4(\xi,\eta) = \frac{1}{4}(1-\xi)(1+\eta)$	$N_2(\xi,\eta) = -\frac{1}{2}(-1+\xi)(-1+\eta)(1+\eta)\xi$
	$N_2(\xi,\eta) = -\frac{1}{2}(1+\xi)(-1+\eta)(1+\eta)\xi$
	$N_2(\xi,\eta) = -\frac{1}{2}(-1+\xi)(1+\xi)(1+\eta)\eta$
	$N_9(\xi,\eta) = (-1+\xi)(1+\xi)(-1+\eta)(1+\eta)$
$\left[\mathbf{N}(\xi,\eta) = N_1 \quad N_2 \quad N_3 \quad N_4\right]$	$\mathbf{N}(\xi,\eta) = \left[N_1 \quad N_2 \quad N_3 \quad N_4 \quad N_5 \quad N_6 \quad N_7 \quad N_8 \quad N_9\right]$

Table 2.14.: First and second order Lagrangian shape function with four and nine nodes.

Lagrangian which consisted of four nodes per element. The nodes are only located at the element-vertexes. Figure 2.26(a) sketches the 4 linear and Figure 2.26(b) to 2.26(d) the 9 quadratic shape functions in the natural coordinate system, respectively.

The complete FEM computation is conducted in the natural coordinate system. Thus, the computation of the semi-discrete weak form requires the computation of derivatives with respect to the natural coordinates ξ and η. The Jacobian matrix $\mathbf{J}$ and its inverse $\mathbf{J}^{-1}$ can be used to transform derivative quantities from the the natural to the global coordinate system and reverse:

$$\begin{bmatrix} \frac{\partial(\cdot)}{\partial\xi} \\ \frac{\partial(\cdot)}{\partial\eta} \end{bmatrix} = \underbrace{\begin{bmatrix} \overbrace{\frac{\partial R}{\partial\xi}}^{J_{11}} & \overbrace{\frac{\partial Z}{\partial\xi}}^{J_{12}} \\ \underbrace{\frac{\partial R}{\partial\eta}}_{J_{21}} & \underbrace{\frac{\partial Z}{\partial\eta}}_{J_{22}} \end{bmatrix}}_{\mathbf{J}} \begin{bmatrix} \frac{\partial(\cdot)}{\partial R} \\ \frac{\partial(\cdot)}{\partial Z} \end{bmatrix}; \qquad \begin{bmatrix} \frac{\partial(\cdot)}{\partial R} \\ \frac{\partial(\cdot)}{\partial Z} \end{bmatrix} = \underbrace{\frac{1}{det\mathbf{J}} \begin{bmatrix} \frac{\partial Z}{\partial\eta} & -\frac{\partial Z}{\partial\xi} \\ -\frac{\partial R}{\partial\eta} & \frac{\partial R}{\partial\xi} \end{bmatrix}}_{\mathbf{J}^{-1}} \begin{bmatrix} \frac{\partial(\cdot)}{\partial\xi} \\ \frac{\partial(\cdot)}{\partial\eta} \end{bmatrix} \tag{2.182}$$

$$\text{with} \quad det\mathbf{J} = \left|J\right| = J_{11}J_{22} - J_{21}J_{12}. \tag{2.183}$$

The Jacobian matrix elements (here, e.g. first-order square quadrilateral Lagrangian) can be computed as follows:

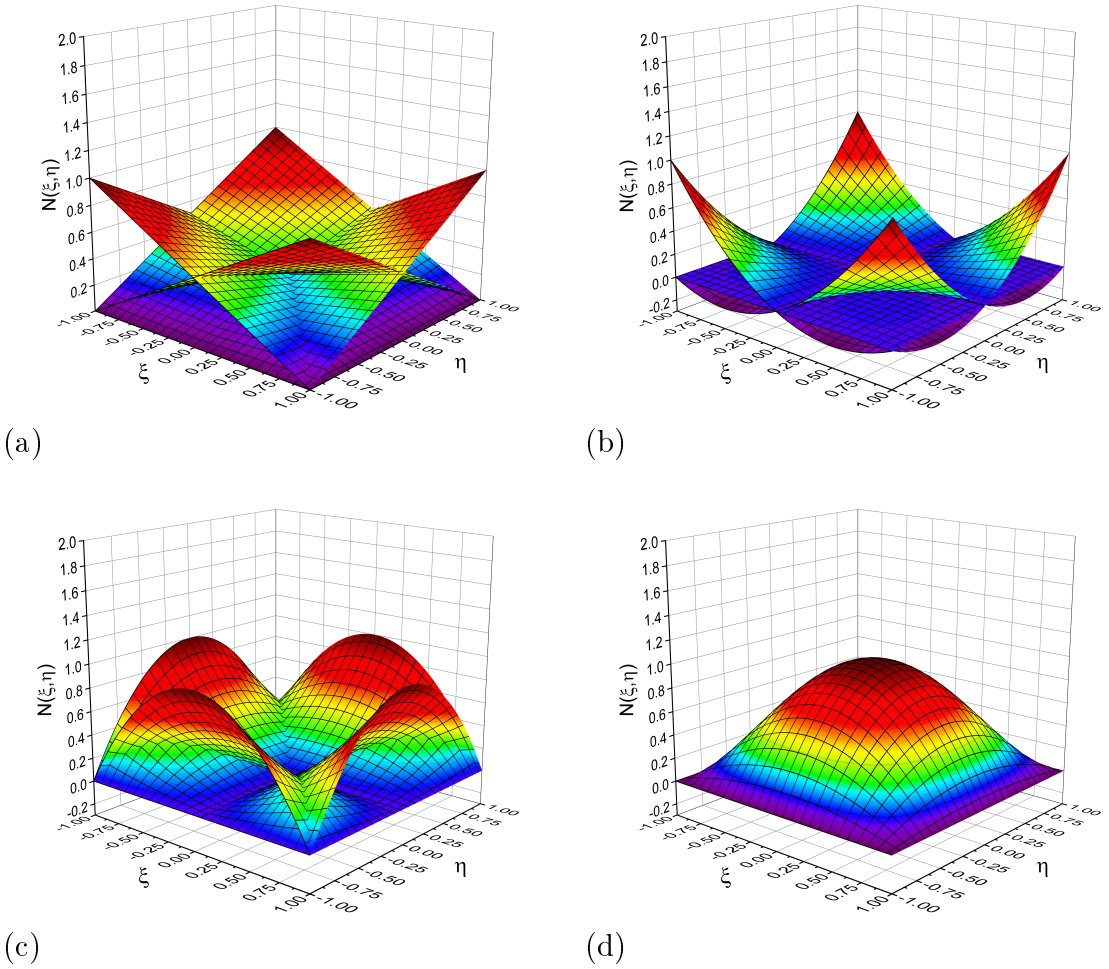

Figure 2.26.: Illustration of the first-order (a) and second-order (b)-(d) square quadrilateral Lagrange elements. The shape functions have a value one at the associated node and zero at all other nodes.

$$\mathbf{J} = \begin{bmatrix} \sum_{i=1}^{n_{nodes}} \frac{\partial N_{i;e}}{\partial \xi} R_{i;e} & \sum_{i=1}^{n_{nodes}} \frac{\partial N_{i;e}}{\partial \xi} Z_{i;e} \\ \sum_{i=1}^{n_{nodes}} \frac{\partial N_{i;e}}{\partial \eta} Z_{i;e} & \sum_{i=1}^{n_{nodes}} \frac{\partial N_{i;e}}{\partial \eta} R_{i;e} \end{bmatrix} = \begin{bmatrix} \frac{\partial N_1}{\partial \xi} & \frac{\partial N_2}{\partial \xi} & \frac{\partial N_3}{\partial \xi} & \frac{\partial N_4}{\partial \xi} \\ \frac{\partial N_1}{\partial \eta} & \frac{\partial N_2}{\partial \eta} & \frac{\partial N_3}{\partial \eta} & \frac{\partial N_4}{\partial \eta} \end{bmatrix} \begin{bmatrix} R_{1;e} & Z_{1;e} \\ R_{2;e} & Z_{2;e} \\ R_{3;e} & Z_{3;e} \\ R_{4;e} & Z_{4;e} \end{bmatrix} \tag{2.184}$$

The derivatives of the shape function in the entries of the stiffness matrix and the boundary vector are defined with respect to the global coordinates R and Z. The Jacobian matrix $\mathbf{J}$ can be used to express these derivatives with respect to the natural coordinates η and ξ:

$$\begin{bmatrix} \frac{\partial N_{i;e}}{\partial \xi} \\ \frac{\partial N_{i;e}}{\partial \eta} \end{bmatrix} = \underbrace{\begin{bmatrix} \frac{\partial R}{\partial \xi} & \frac{\partial Z}{\partial \xi} \\ \frac{\partial R}{\partial \eta} & \frac{\partial Z}{\partial \eta} \end{bmatrix}}_{\mathbf{J}} \begin{bmatrix} \frac{\partial N_{i;e}}{\partial R} \\ \frac{\partial N_{i;e}}{\partial Z} \end{bmatrix}; \qquad \begin{bmatrix} \frac{\partial N_{i;e}}{\partial R} \\ \frac{\partial N_{i;e}}{\partial Z} \end{bmatrix} = \underbrace{\frac{1}{det\mathbf{J}} \begin{bmatrix} \frac{\partial Z}{\partial \eta} & -\frac{\partial Z}{\partial \xi} \\ -\frac{\partial R}{\partial \eta} & \frac{\partial R}{\partial \xi} \end{bmatrix}}_{\mathbf{J}^{-1}} \begin{bmatrix} \frac{\partial N_{i;e}}{\partial \xi} \\ \frac{\partial N_{i;e}}{\partial \eta} \end{bmatrix}. \tag{2.185}$$

For a 2d-axisymmetric element, the area ratio between the global element (global coordinates) and the natural element (natural coordinates) equals the value of the Jacobin determinant.

It is noted, that for the volume and surface integration a transformation to the natural coordinates system is necessary. The integral can be converted via (see also section A.4.1):

$$\int_{\Omega_{0;e}} (\cdot)\, dV_0 = 2\pi \int_{\Omega_{0;e}} (\cdot)\, R\, dR\, dZ = 2\pi \int_{-1}^{1}\int_{-1}^{1} (\cdot)\, R(\xi,\eta)\big|J\big|\, \mathrm{d}\xi\, \mathrm{d}\eta \tag{2.186}$$

$$\int_{\partial\Omega_{0;e}} (\cdot)\, dA_0 = 2\pi \int_{\partial\Omega_{0;e}} (\cdot)\, R\, dS_0 = 2\pi \int_{-1}^{1} (\cdot)\, R(\xi,\eta) \sqrt{\frac{(\partial R)^2}{\partial(\xi,\eta)} + \frac{(\partial Z)^2}{\partial(\xi,\eta)}}\, \mathrm{d}(\xi,\eta) \tag{2.187}$$

here, $(\cdot)$ denotes an arbitrary function and $\mathrm{d}(\xi,\eta)$ is either a line integration over the coordinate $\mathrm{d}\xi$ or $\mathrm{d}\eta$.

Now, a semi-discrete formulation for a finite element can be derived. First, the matrices for each element will determined separately and then assembly to the global matrices is constructed.

Intensity space discretization

As described in the previous section (section 2.8.1), FEM is based essentially on weighted residual methods where the solution of a PDE is approached by the sum of weighted basis function. The variables can be approximated by a linear combination of basis function. Equation 2.188a and 2.188b show the discretization for the intensity and the trail function as a linear combination of basis function weighted by the coefficients $\mathbf{N}$ of the solution vector $\mathbf{u_I}$ and $\tilde{\mathbf{v}}$, respectively, for one element.

$$\mathbf{I}_e(R,Z) = \sum_{j=0}^{n_{nodes}} N_j(R,Z)\, u_{\mathbf{I};j} = \mathbf{N}\mathbf{u_I} \tag{2.188a}$$

$$\mathbf{v}_e(R,Z) = \sum_{i=0}^{n_{nodes}} N_i(R,Z)\, tildev_i = \mathbf{N}\tilde{\mathbf{v}} \tag{2.188b}$$

The shape function type was chosen as Lagrangian and the element order was quadratic in the material frame. According to the Galerkin approximation method the same function

may be used for the basis- and the trail function $\mathbf{N_i}(R,Z) = \mathbf{N_j}(R,Z)$. The space discretized FEM-intensity equation 2.26 fro one element then reads:

$$\int_{\Omega_{0;e}} (\boldsymbol{\nabla}\mathbf{N}\tilde{\mathbf{v}})^T \left(\boldsymbol{\nabla}\mathbf{N}\mathbf{u_I} + \alpha_{\mathbf{opt}}\mathbf{N}\mathbf{u_I}\right)\, \mathrm{d}V_0 = -\int_{\partial\Omega_{0;e}} \mathbf{N}\tilde{\mathbf{v}} \left[\left(\boldsymbol{\nabla}\mathbf{N}\mathbf{u_I} + \alpha_{\mathbf{opt}}\mathbf{N}\mathbf{u_I}\right)^T \mathbf{n}\right]\, \mathrm{d}A_0. \quad (2.189)$$

A common substitution is used to replace the gradient of the shape function by a so-called B-matrix $\mathbf{B} = \boldsymbol{\nabla}\mathbf{N}$. Further $\tilde{\mathbf{v}}$ vanishes in equation 2.189.

$$\int_{\Omega_{0;e}} \mathbf{B}^T \left(\mathbf{B} + \alpha_{\mathbf{opt}}\mathbf{N}\right)\, \mathrm{d}V_0\, \mathbf{u_I} = -\int_{\partial\Omega_{0;e}} \mathbf{N}^T \underbrace{\left[\left(\mathbf{B}\mathbf{u_I} + \alpha_{\mathbf{opt}}\mathbf{N}\mathbf{u_I}\right)^T \mathbf{n}\right]}_{q}\, \mathrm{d}A_0 \quad (2.190)$$

The integral of the right and left hand side in equation 2.190 can be rewritten in a compact form:

$$\mathbf{K}_{\mathbf{I};e} = \int_{\Omega_{0;e}} \mathbf{B}^T \left(\mathbf{B} + \alpha_{opt}\mathbf{N}\right)\, \mathrm{d}V_0 \quad (2.191a)$$

$$\mathbf{f}_{\mathbf{I};e} = \int_{\partial\Omega_{0;e}} \mathbf{N}^T\, q\, \mathrm{d}A_0 \quad (2.191b)$$

here, $\mathbf{K}_{\mathbf{I};e}$ is the stiffness matrix and $\mathbf{f}_{\mathbf{I};e}$ is the force vector. The force vector is non zero only if a element boundary contributes to the surface. The finial equation system can be expressed as:

$$\mathbf{K}_{\mathbf{I};e}\, \mathbf{u}_{\mathbf{I};e} = \mathbf{f}_{\mathbf{I};e} \quad (2.192)$$

Equation 2.191a mapped to the natural coordinate system can be found in section A.4.2. For the square quadrilateral Lagrange elements a local $n_{el} \times n_{el}$ stiffness matrix is produced. The solution vector $\mathbf{u}_{\mathbf{I};e}$ for a nine node element is defined by:

$$\mathbf{u}_{\mathbf{I};e} = \begin{bmatrix} N_1 & N_2 & \cdots & N_9 \end{bmatrix} \begin{bmatrix} u_{I;1} \\ u_{I;2} \\ \vdots \\ u_{I;9} \end{bmatrix} \quad (2.193)$$

For the 9 node finite element the stiffness matrix has a dimension of 9×9 and the solution and the force vector are both of dimension 9. The complete equation system for one finite element reads:

$$\begin{bmatrix} K_{11} & ... & K_{91} \\ K_{12} & ... & K_{29} \\ \vdots & \ddots & \vdots \\ K_{19} & ... & K_{99} \end{bmatrix} \begin{bmatrix} u_{I;1} \\ u_{I;2} \\ \vdots \\ u_{I;9} \end{bmatrix} = \begin{bmatrix} F_1 \\ F_2 \\ \vdots \\ F_9 \end{bmatrix} \tag{2.194}$$

Thermal heat transfer space discretization

The Temperature T_e and T_l and the weight function $\mathbf{v}$ can be approximated by a linear combination of shape functions $N_j(R,Z) = N_i(R,Z)$ according to Galerkin's approach. In addition, the time derivative of T_e and T_l may be approximated in the same way:

$$\mathbf{T}_{e,l;e}(R,Z) = \sum_{j=0}^{n_{node}} N_{ej,lj}(R,Z)\; u_{T_{e,l};j}(t) = \mathbf{N}\mathbf{u}_{\mathbf{T}_{e,l}}(t) \tag{2.195a}$$

$$\dot{\mathbf{T}}_{e,l;e}(R,Z) = \sum_{j=0}^{n_{node}} N_{ej,lj}(R,Z)\; \dot{u}_{T_{e,l};j}(t) = \mathbf{N}\dot{\mathbf{u}}_{\mathbf{T}_{e,l}}(t) \tag{2.195b}$$

$$\mathbf{v}_{e,l;e}(R,Z) = \sum_{i=0}^{n_{node}} N_i(R,Z)\tilde{v}_i = \mathbf{N}\tilde{\mathbf{v}}_{e,l}. \tag{2.195c}$$

In odrder to formulate the semi-discrete non-linear heat transfere equations, the temperautre depenency of the heat capacity and the heat conduction may be approximated similar:[120–122]

$$\rho_0 \int\limits_{\Omega_{0;e}} (\mathbf{N}_e\mathbf{v}_e)^T\; C_{p;e}(\mathbf{N}_e\mathbf{u}_{\mathbf{T}_e})\; \mathbf{N}_e\dot{\mathbf{u}}_{\mathbf{T}_e}\; \mathrm{d}V_0 + \int\limits_{\Omega_{0;e}} (\mathbf{N}_e\mathbf{v}_e)^T\, k_e(\mathbf{N}_e\mathbf{u}_{\mathbf{T}_e}, \mathbf{N}_l\mathbf{u}_{\mathbf{T}_l})\boldsymbol{\nabla}\mathbf{N}\; \mathrm{d}V_0\; \mathbf{u}_{\mathbf{T}_e} =$$
$$\int\limits_{\Omega_{0;e}} \mathbf{N}_e\mathbf{v}_e\left(Q - G\left(\mathbf{N}_e\mathbf{u}_{\mathbf{T}_e} - \mathbf{N}_l\mathbf{u}_{\mathbf{T}_l}\right)\right)\mathrm{d}V_0 + \int\limits_{\partial\Omega_0^e} \mathbf{N}_e\mathbf{v}_e \underbrace{\left(k_e(\mathbf{N}_e\,\mathbf{u}_{\mathbf{T}_e}, \mathbf{N}_l\,\mathbf{u}_{\mathbf{T}_l})\boldsymbol{\nabla}\mathbf{N}_e\mathbf{u}_{\mathbf{T}_e}\right)^T\mathbf{n}}_{\mathbf{q}_e}\mathrm{d}A_0 \tag{2.196a}$$

$$\rho_0 \int\limits_{\Omega_{0;e}} (\mathbf{N}_l\mathbf{v}_l)^T\; C_{p;l}(\mathbf{N}_l\mathbf{u}_{\mathbf{T}_l})\; \mathbf{N}_l\dot{\mathbf{u}}_{\mathbf{T}_l}\; \mathrm{d}V_0 + \int\limits_{\Omega_{0;e}} (\mathbf{N}_e\mathbf{v}_l)^T\, k_l\; \boldsymbol{\nabla}\mathbf{N}_l\; \mathrm{d}V_0\; \mathbf{u}_{\mathbf{T}_e} =$$
$$\int\limits_{\Omega_{0;e}} \mathbf{N}_e\mathbf{v}_l\; G\left(\mathbf{N}_e\mathbf{u}_{\mathbf{T}_e} - \mathbf{N}_l\mathbf{u}_{\mathbf{T}_l}\right)\; \mathrm{d}V_0 + \int\limits_{\partial\Omega_{0;e}} \mathbf{N}_e\mathbf{v}_l\; \underbrace{\left(k_l\; \boldsymbol{\nabla}\mathbf{N}_l\mathbf{u}_{\mathbf{T}_l}\right)^T\mathbf{n}}_{\mathbf{q}_l}\; \mathrm{d}A_0. \tag{2.196b}$$

The trail function $\mathbf{v}_{e,l}$ vanishes in the equation system 2.196. The gradient of the shape function can be replaced by the B-matrix $\mathbf{B}_{e,l} = \boldsymbol{\nabla}\mathbf{N}_{e,l}$ and the expression $\left(k_{e,l}\boldsymbol{\nabla}\mathbf{N}_{e,l}\mathbf{u}_{\mathbf{T}_{e;l}}\right)^T\mathbf{n}$ can be considered as the spacial discretized heat flux $\mathbf{q}_{e,l}$:

$$\rho_0 \int\limits_{\Omega_0^e} \mathbf{N}_e^T \, \mathbf{C}_{p;e}(\mathbf{N}_e \mathbf{u}_{\mathbf{T}_e}) \, \mathbf{N}_e \dot{\mathbf{u}}_{\mathbf{T}_e} \, \mathrm{d}V_0 + \int\limits_{\Omega_0^e} \mathbf{B}_e^T \mathbf{k}_e(\mathbf{N}_e \mathbf{u}_{\mathbf{T}_e}, \mathbf{N}_l \mathbf{u}_{\mathbf{T}_l}) \mathbf{B}_e \, \mathrm{d}V_0 \mathbf{u}_{\mathbf{T}_e} =$$
$$- \int\limits_{\Omega_0^e} \mathbf{N}_e^T \left(Q - G \left(\mathbf{N}_e \mathbf{u}_{\mathbf{T}_e} - \mathbf{N}_l \mathbf{u}_{\mathbf{T}_e} \right) \right) \mathrm{d}V_0 + \int\limits_{\partial\Omega} \mathbf{N}_e^T \mathbf{q}_e^T \mathbf{n} \mathrm{d}A_0 \tag{2.197a}$$

$$\rho_0 \int\limits_{\Omega_0^e} \mathbf{N}_l^T \, \mathbf{C}_{p;l}(\mathbf{N} \mathbf{u}_{\mathbf{T}_l}) \, \mathbf{N}_l \dot{\mathbf{u}}_{\mathbf{T}_l} \, \mathrm{d}V_0 + \int\limits_{\Omega_0^e} \mathbf{B}_l^T \mathbf{k}_l \, \mathbf{B}_l \, \mathrm{d}V_0 \mathbf{u}_{\mathbf{T}_l} =$$
$$- \int\limits_{\Omega_0^e} \mathbf{N}_l^T \, G \left(\mathbf{N}_e \mathbf{u}_{\mathbf{T}_e} - \mathbf{N}_l \mathbf{u}_{\mathbf{T}_l} \right) \mathrm{d}V_0 + \int\limits_{\partial\Omega_0^e} \mathbf{N}_l^T \mathbf{q}_l^T \mathbf{n} \mathrm{d}A_0 . \tag{2.197b}$$

By rearranging the equation system 2.197 the spacial discretized electron and lattice temperature $\mathbf{u}_{\mathbf{T_e}}$ and $\mathbf{u}_{\mathbf{T_l}}$ can be separated, respectively and the final spacial discretized weak form of the two coupled heat equations can be derived:

$$\overbrace{\rho_0 \int\limits_{\Omega_0^e} \mathbf{N}_e^T \, \mathbf{C}_{p;e}(\mathbf{N}_e \mathbf{u}_{\mathbf{T}_e}) \, \mathbf{N} \, \mathrm{d}V_0}^{\mathbf{C_e}} \dot{\mathbf{u}}_{\mathbf{T}_e} - \overbrace{\int\limits_{\Omega_0^e} \mathbf{B}_e^T \mathbf{k}_{\mathbf{e}}(\mathbf{N}_e \mathbf{u}_{\mathbf{T}_e}, \mathbf{N}_l \mathbf{u}_{\mathbf{T}_l}) \mathbf{B}_e + G \, \mathbf{N}_e \, \mathrm{d}V_0}^{K_{ee}} \mathbf{u}_{\mathbf{T}_e} -$$
$$\underbrace{\int\limits_{\Omega_0^e} G \, \mathbf{N}_l \, \mathrm{d}V_0}_{K_{el}} \mathbf{u}_{\mathbf{T}_l} = \underbrace{- \int\limits_{\Omega_0^e} \mathbf{N}_e Q \, \mathrm{d}V_0 + \int\limits_{\partial\Omega_0^e} \mathbf{N}_e^T \mathbf{q}_e^T \mathbf{n} \, \mathrm{d}A_0}_{\mathbf{f}_e} \tag{2.198a}$$

$$\overbrace{\rho_0 \int\limits_{\Omega_0^e} \mathbf{N}_l^T \, \mathbf{C}_{p;l}(\mathbf{N} \mathbf{u}_{\mathbf{T}_l}) \, \mathbf{N}_l \, \mathrm{d}V_0}^{\mathbf{C_l}} \dot{\mathbf{u}}_{\mathbf{T}_l} - \overbrace{\int\limits_{\Omega_0^e} \mathbf{B}_l^T \mathbf{k}_l \, \mathbf{B}_l - G \, \mathbf{N}_l \, \mathrm{d}V_0}^{K_{ll}} \mathbf{u}_{\mathbf{T}_l} +$$
$$\underbrace{\int\limits_{\Omega_0^e} G \, \mathbf{N}_e \, \mathrm{d}V_0}_{K_{le}} \mathbf{u}_{\mathbf{T}_e} = \underbrace{\int\limits_{\partial\Omega_0^e} \mathbf{N}_l^T \mathbf{q}_l^T \mathbf{n} \, \mathrm{d}A_0}_{\mathbf{f}_l} . \tag{2.198b}$$

The equation system 2.198 can be rewritten in a more compact form:

$$\mathbf{C}_e(\mathbf{u}_{\mathbf{T}_e}) \, \dot{\mathbf{u}}_{\mathbf{T}_e} - \mathbf{K}_{ee}(\mathbf{u}_{\mathbf{T}_e}, \mathbf{u}_{\mathbf{T}_l}) \, \mathbf{u}_{\mathbf{T}_e} - \mathbf{K}_{el} \, \mathbf{u}_{\mathbf{T}_e} + \mathbf{f}_e \left(\mathbf{u}_{\mathbf{T}_e}, \mathbf{u}_{\mathbf{T}_l} \right) = 0 \tag{2.199a}$$

$$\mathbf{C}_e(\mathbf{u}_{\mathbf{T}_l}) \, \dot{\mathbf{u}}_{\mathbf{T}_e} - \mathbf{K}_{ll} \, \mathbf{u}_{\mathbf{T}_l} - \mathbf{K}_{le} \, \mathbf{u}_{\mathbf{T}_e} + \mathbf{f}_l \left(\mathbf{u}_{\mathbf{u}} \right) = 0 \tag{2.199b}$$

It is worth noting, that besides the temperature dependency of the equation system 2.198 the lattice force vector $\mathbf{f}_l$ depends on the displacement $\mathbf{u}_{\mathbf{u}}$ due to the boundary condition from

table 2.8 and 2.9. Thanks to the thermal isolation of the electron sub system, the electron force vector $\mathbf{f}_e$ is equal to zero. Now, the equation system 2.199 can be written in a matrix form:

$$\underbrace{\begin{bmatrix}\mathbf{C}_e(\mathbf{u_{T}}_e, \mathbf{u_{T}}_l) & 0 \\ 0 & \mathbf{C}_l(\mathbf{u_{T}}_l)\end{bmatrix}}_{\mathbf{C}_T(\mathbf{u_{T}}_e, \mathbf{u_{T}}_l)} \underbrace{\begin{bmatrix}\dot{\mathbf{u}}_{\mathbf{T}_e} \\ \dot{\mathbf{u}}_{\mathbf{T}_l}\end{bmatrix}}_{\dot{\mathbf{u}}_\mathbf{T}} + \underbrace{\begin{bmatrix}\mathbf{K}_{ee}(\mathbf{u_{T}}_e, \mathbf{u_{T}}_l) & \mathbf{K}_{el} \\ \mathbf{K}_{le} & \mathbf{K}_{ll}\end{bmatrix}}_{\mathbf{K}_T(\mathbf{u_{T}}_e, \mathbf{u_{T}}_l)} \underbrace{\begin{bmatrix}\mathbf{u_{T}}_e \\ \mathbf{u_{T}}_l\end{bmatrix}}_{\mathbf{u_T}} - \underbrace{\begin{bmatrix}0 \\ \mathbf{f}_l(\mathbf{u_{T}}_l, \mathbf{u_u})\end{bmatrix}}_{\mathbf{f}_T(\mathbf{u_{T}}_l, \mathbf{u_u})} = 0 \tag{2.200}$$

Because of the time dependency of the equation system 2.198 a spacial semi-discrete first order ordinary differential equation in time is produced:[117,123]

$$\mathbf{C_T}\dot{\mathbf{u}}_\mathbf{T} + \mathbf{K_T}\mathbf{u_T} = \mathbf{f_T}. \tag{2.201}$$

Thermal expansion space discrtization

The displacement $\mathbf{u}$ and the virtual displacement $\delta\mathbf{u}$ may approximated by a linear combination of the same shape functions $N_j(R,Z) = N_i(R,Z)$ according to Galerkin's approach. In addition, the first and second time derivative of $\mathbf{u}$ may be approximated in the same way. According to the equation system 2.169 a mixed formulation was applied with the pressure as a new independent variable. Consequently, the pressure $\mathbf{p}$ and its variation $\delta\mathbf{p}$ has to be discretized by $\mathbf{u_p}$ and $\tilde{\mathbf{v}}_\mathbf{p}$, respectively.

$$\begin{aligned}
\mathbf{u}(R,Z) &\approx \sum_{j=0}^{n} N_j(R,Z)\; u_{u;j}(t) = \mathbf{N}\mathbf{u}_{\tilde{\mathbf{u}}}(t); \\
\dot{\mathbf{u}}(R,Z) &\approx \sum_{j=0}^{n} N_j(R,Z)\; \dot{u}_{u;j}(t) = \mathbf{N}\dot{\mathbf{u}}_{\tilde{\mathbf{u}}}(t); \qquad \mathbf{p}(R,Z) \approx \sum_{j=0}^{n} N_{p;j}(R,Z)\; p_{u;j}(t) = \mathbf{N}_p\mathbf{u_p}(t) \\
\ddot{\mathbf{u}}(R,Z) &\approx \sum_{j=0}^{n} N_j(R,Z)\; \ddot{u}_{u;j}(t) = \mathbf{N}\ddot{\mathbf{u}}_{\tilde{\mathbf{u}}}(t); \qquad \delta\mathbf{p}(R,Z) \approx \sum_{i=0}^{n} N_{p;i}(R,Z)\; p_{u;i} = \mathbf{N}_p\tilde{\mathbf{v}}_p \\
\underbrace{\delta\mathbf{u}(R,Z)}_{\mathbf{v}(R,Z)} &\approx \sum_{i=0}^{n} N_i(R,Z)\tilde{v}_{u;i} = \mathbf{N}\tilde{\mathbf{v}}
\end{aligned}$$

The gradient of $\mathbf{N}$ can be express as the B-matrix $\mathbf{B}$ and the strain $\mathbf{E}$ and its variation $\delta\mathbf{E}$ as the product of the B-matrix $\mathbf{B}$ and the displacement $\mathbf{u}$ and the variation of the displacement $\delta\mathbf{u}$, respectively.

$$\mathbf{B} = \boldsymbol{\nabla}\mathbf{N}; \qquad \mathbf{B}_p = \boldsymbol{\nabla}\mathbf{N}_p; \qquad \mathbf{E} = \mathbf{B}\mathbf{u}; \qquad \delta\mathbf{E} = \mathbf{B}\delta\mathbf{u}. \tag{2.202}$$

Equation 2.168 can now be spatially discretized by:

$$\rho_0 \int\limits_{\Omega_{0;e}} (\mathbf{N}\tilde{\mathbf{v}})^T \ \ddot{\mathbf{u}}_{\tilde{\mathbf{u}}}\, \mathbf{N}\, \mathrm{d}V_0 + \int\limits_{\Omega_{0;e}} \mathbf{S} : \boldsymbol{\nabla}\mathbf{N}\tilde{\mathbf{v}}\, \mathrm{d}V_0 - \int\limits_{\Omega_{0;e}} \mathbf{N}\tilde{\mathbf{v}}\, \mathbf{F}_V\, \mathrm{d}V_0 - \int\limits_{\partial\Omega_{0;e}} \mathbf{N}\tilde{\mathbf{v}}\, \tilde{\mathbf{t}} \cdot \mathbf{n}\, \mathrm{d}A_0 = 0. \tag{2.203}$$

By applying the substitution $\mathbf{S} = \mathbf{C}_{el}\, \mathbf{B}\, \mathbf{u}_{\tilde{\mathbf{u}}}$, equation 2.203 yields to:

$$\underbrace{\rho_0 \int\limits_{\Omega_{0;e}} \mathbf{N}^T\, \mathbf{N}\, \mathrm{d}V_0\, \ddot{\mathbf{u}}_{\tilde{\mathbf{u}}}}_{\delta W_{kin}} + \underbrace{\int\limits_{\Omega_{0;e}} \mathbf{B}^T\, \mathbf{C}_{el}\, \mathbf{B}\, \mathrm{d}V_0\, \mathbf{u}_{\tilde{\mathbf{u}}}}_{\delta W_{int}} - \underbrace{\int\limits_{\Omega_{0;e}} \mathbf{N}\, \mathbf{F}_V\, \mathrm{d}V_0 - \int\limits_{\partial\Omega_{0;e}} \mathbf{N}\, \tilde{\mathbf{t}} \cdot \mathbf{n}\, \mathrm{d}A_0}_{\delta W_{ext}} = 0. \tag{2.204}$$

The discretization of the mixed formulation (equation 2.169) then may reads:

$$\underbrace{\overbrace{\rho_0 \int\limits_{\Omega_{0;e}} \mathbf{N}^T\, \mathbf{N}\, \mathrm{d}V_0}^{\mathbf{A}}\, \ddot{\mathbf{u}}_{\tilde{\mathbf{u}}}}_{\mathbf{f}_{iner}} + \underbrace{\overbrace{\int\limits_{\Omega_{0;e}} \mathbf{B}^T : \mathbf{D}_d : \mathbf{B}\, \mathrm{d}V_0}^{\mathbf{B}}\, \mathbf{u}_{\tilde{\mathbf{u}}} + \overbrace{\int\limits_{\Omega_{0;e}} (\mathbf{N}_p\mathbf{I}) : \mathbf{B}\, \mathrm{d}V_0}^{\mathbf{C}}\, \mathbf{u}_p}_{\mathbf{f}_{int}} - \underbrace{\int\limits_{\Omega_{0;e}} \mathbf{N}^T\, \mathbf{F}_V\, \mathrm{d}V_0 \int\limits_{\partial\Omega_{0;e}} \mathbf{N}^T\, \tilde{\mathbf{t}} \cdot \mathbf{n}\, \mathrm{d}A_0}_{\mathbf{f}_{ext}} = 0 \tag{2.205a}$$

$$\underbrace{\int\limits_{\Omega_{0;e}} \mathbf{N}_p \mathbf{v}_p \left[\mathbf{I}^T\mathbf{B}\, \mathbf{u}_{\mathbf{u}} - \frac{\mathbf{N}_p\mathbf{u}_p}{K}\right] \mathrm{d}V_0}_{\mathbf{f}_{int}} = \overbrace{\int\limits_{\Omega_{0;e}} \mathbf{N}_p^T\mathbf{I}\mathbf{B}\, \mathrm{d}V_0}^{\mathbf{C}}\, \mathbf{u}_{\tilde{\mathbf{u}}} - \overbrace{\int\limits_{\Omega_{0;e}} \mathbf{N}_p^T \frac{1}{K}\mathbf{N}_p\, \mathrm{d}V_0}^{\mathbf{D}}\, \mathbf{u}_p = 0, \tag{2.205b}$$

here, the substitution $\mathbf{S} = \mathbf{D}_D : \mathbf{E}_{el} - \mathbf{D}_v : \mathbf{p}\mathbf{I} = \mathbf{D}_d : (\mathbf{E}_{GL} - \mathbf{E}_p - \mathbf{E}_{th}) - \left(\frac{1}{3} tr(\mathbf{D}_v : \mathbf{E}_{GL} - \mathbf{E}_{th})\right)\mathbf{I}$ is included.

The equation system 2.205 can now be written in a matrix form:

$$\underbrace{\begin{bmatrix}\mathbf{A} & 0\\ 0 & 0\end{bmatrix}}_{\mathbf{M_u}} \underbrace{\begin{bmatrix}\ddot{\mathbf{u}}_{\tilde{\mathbf{u}}}\\ \ddot{\mathbf{u}}_p\end{bmatrix}}_{\ddot{\mathbf{u}}_{\mathbf{u}}} + \underbrace{\begin{bmatrix}\mathbf{B} & \mathbf{C}\\ \mathbf{C}^T & \mathbf{D}\end{bmatrix}}_{\mathbf{K_u}} \underbrace{\begin{bmatrix}\mathbf{u}_{\tilde{\mathbf{u}}}\\ \mathbf{u}_p\end{bmatrix}}_{\mathbf{u}_{\mathbf{u}}} = \underbrace{\begin{bmatrix}\mathbf{f}_{ext}\\ 0\end{bmatrix}}_{f_{\mathbf{uu}}} \tag{2.206}$$

here, $\mathbf{u}_p$ appears as a so-called Lagrange multiplier. The Rayleigh damping model (see section 2.7.3) is may spatially discretized within a damping matrix $\mathbf{C_u}$ which is a linear combination of the mass matrix $\mathbf{M_u}$ and the stiffness matrix $\mathbf{K_u}$. $\mathbf{f}_{ext}$ is the vector of external

forces and $\mathbf{u_u}$ as the spatially discretized displacement vector. The superimposed single and double dots of $\mathbf{u_u}$ features its first and second time derivative which is the spatially discretized velocity and acceleration. The final semi-discretized thermal expansion equation (discretized in space and continuous in time) reads:

$$\mathbf{M_u}\ddot{\mathbf{u}}_\mathbf{u} + \mathbf{C_u}\dot{\mathbf{u}}_\mathbf{u} + \mathbf{K_u}\mathbf{u_u} = f_{\mathbf{u_u}}; \qquad \text{with} \quad \mathbf{C_u} = \alpha_{dM}\,\mathbf{M_u} + \beta_{dK}\,\mathbf{K_u}. \tag{2.207}$$

2.8.2. Numerical integration

The determination of the integral equations which arises in the spatially discretized weak forms was performed in the parent coordinate system. The integrals are solved by numerical integration in the framework of the Gauss quadrature.[115] The integrals are computed at discrete points, the so-called Gauss points which are not concentrically positioned with the mesh points. Figure 2.27 shows the position for a number of 4 (black solid circle) and 9 (red dashed circle) Gauss points n. For an arbitrary function $f(\xi,\eta)$ the volume integration in the axisymmetric case yields to:

$$\int\limits_{\Omega_{0;e}} f\,(R,Z)\;\mathrm{d}V_0 = \int\limits_{\Omega_{0;e}} f\,(R,Z)\,2\,\pi\,R\,\mathrm{d}R\,\mathrm{d}Z = \int\limits_{-1}^{1}\int\limits_{-1}^{1} f\,(\xi,\eta)\,2\,\pi\,R(\xi,\eta)\big|J\big|\,\mathrm{d}\xi\,\mathrm{d}\eta = \sum_{i=1}^{n}\sum_{j=1}^{n} f\,(\xi_i,\eta_j)\,2\,\pi\,R(\xi,\eta)\big|J\big|\,w_i\,w_j, \tag{2.208}$$

here, $w_{i;j}$ are the so-called weights.

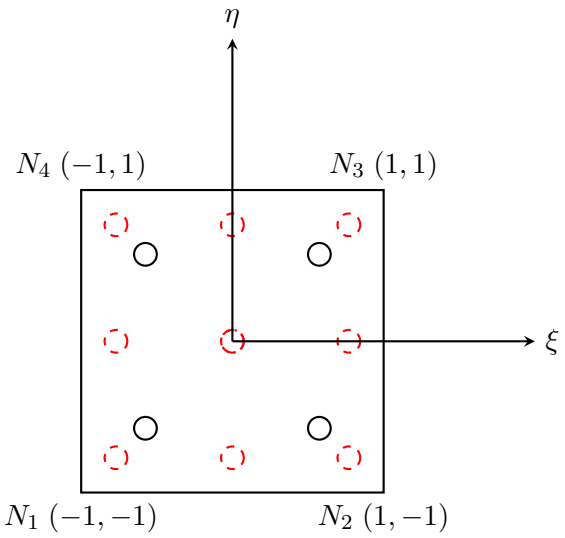

Figure 2.27.: Positions of the Gauss points in the (ξ,η)-plane within a finite element for a number of 4 (black solid circle) and 9 (red dashed circle). The Gauss points do not coincide with the position of the nodes.

The Gauss points position with respect to ξ_i and η_i in combination with the weights $w_{i;j}$ for a number of 4 and 9 are summarized in table 2.15.

Numbers of Gauss points	Gauss quadrature point	ξ_i	η_j	$w_{i;j}$
4	No.1	$-1/\sqrt{3}$	$-1/\sqrt{3}$	1
	No.2	$1/\sqrt{3}$	$-1/\sqrt{3}$	1
	No.3	$-1/\sqrt{3}$	$1/\sqrt{3}$	1
	No.4	$1/\sqrt{3}$	$1/\sqrt{3}$	1
9	No.1	$-\sqrt{3/5}$	$-\sqrt{3/5}$	25/81
	No.2	0	$-\sqrt{3/5}$	40/81
	No.3	$\sqrt{3/5}$	$-\sqrt{3/5}$	25/81
	No.4	$-\sqrt{3/5}$	0	40/81
	No.5	0	0	64/81
	No.6	$-\sqrt{3/5}$	0	40/81
	No.7	$-\sqrt{3/5}$	$-\sqrt{3/5}$	25/81
	No.8	0	$\sqrt{3/5}$	40/81
	No.9	$\sqrt{3/5}$	$\sqrt{3/5}$	25/81

Table 2.15.: Gauss quadrature points (ξ_i, η_j) and weights $w_{i;j}$ for quadrilateral element.

2.8.3. Assembly

In the previous chapter 2.8.1 the discretized mass, damping, stiffness matrix and force vector were introduced for one local finite element. To obtain a solution for the complete FEM domain a assembly procedure is necessary which contains all element contributions. In the one dimensional case, the governing integral equations of the weak form can be obtained by integration over each element and subsequent summation of the element integration:

$$\int_{\Omega_0} (\cdot)\ dV_0 = \sum_{n_{element}} \underbrace{\left(\int_{\Omega_{0;e}} (\cdot)\ dV_0 \right)}_{\sum_{i=1}^{n_{nodes}} (\cdot) w_i}. \tag{2.209}$$

For two and three dimensions the sum has to be replaced by the so-called element assembly operator $\mathbb{A}_{el}$ which produces a matrix with elements of each nodal integration. Finally, the global assembly operator $\mathbb{A}_g$ forms the global matrix from each element contribution:

$$\int_{\Omega_0} (\cdot)\ dV_0 \approx \mathop{\mathbb{A}}_{i=1}^{n_{el}} \left[\mathop{\mathbb{A}}_{i=1}^{n_{nodes}} \left(\underbrace{\int_{\Omega_0^e} (\cdot)\ dV_0}_{\sum_{i=1}^{n_{nodes}} \sum_{j=1}^{n_{nodes}} (\cdot) w_i\ w_j} \right) \right], \tag{2.210}$$

here, the volume integral is achieved by two sums for the Gauss quadrature in the axisymmetric case. The global assembly operator $\mathbb{A}_g$ finally merges the local element matrices formed by $\mathbb{A}_{el}$ to the global matrices:

$$\begin{aligned} \mathbf{M} &= \mathop{\mathbb{A}}_{e=1}^{n_{el}} \mathbf{M}_e & \mathbf{K} &= \mathop{\mathbb{A}}_{e=1}^{n_{el}} \mathbf{K}_e \\ \mathbf{C} &= \mathop{\mathbb{A}}_{e=1}^{n_{el}} \mathbf{C}_e & \mathbf{f} &= \mathop{\mathbb{A}}_{e=1}^{n_{el}} \mathbf{f}_e \end{aligned} \tag{2.211}$$

The dimension of the global FEM matrices depends on the number of nodes in each spacial direction. The assembly operators $\mathbb{A}_{el}$ and $\mathbb{A}_g$ are implemented in the FEM code by an algorithm.[84,117,124,125]

2.8.4. Equation coupling

By combing all spatially discretized finite element equation of intensity (equation 2.192), heat conduction of the electron and lattice subsystem (equation 2.201) and the mechanical motion due to thermal expansion (equation 2.207) within a fully coupled approach the following matrix system is produced:[126]

$$\begin{aligned} \overbrace{\begin{bmatrix} \mathbf{r}_i \\ \mathbf{r}_e \\ \mathbf{r}_l \\ \mathbf{r}_u \end{bmatrix}}^{\mathbf{r}} = & \overbrace{\begin{bmatrix} 0 & 0 & 0 & 0 \\ 0 & 0 & 0 & 0 \\ 0 & 0 & 0 & 0 \\ 0 & 0 & 0 & \mathbf{M_u} \end{bmatrix}}^{\mathbf{M}} \overbrace{\begin{bmatrix} \ddot{\mathbf{u}}_\mathbf{I} \\ \ddot{\mathbf{u}}_{\mathbf{T}_e} \\ \ddot{\mathbf{u}}_{\mathbf{T}_e} \\ \ddot{\mathbf{u}}_\mathbf{u} \end{bmatrix}}^{\ddot{\mathbf{u}}} + \overbrace{\begin{bmatrix} 0 & 0 & 0 & 0 \\ 0 & \mathbf{C}_e(\mathbf{u}_{\mathbf{T}_e}) & 0 & 0 \\ 0 & 0 & \mathbf{C}_l(\mathbf{u}_{\mathbf{T}_l}) & 0 \\ 0 & 0 & 0 & \mathbf{C_u}(\mathbf{u_u}) \end{bmatrix}}^{\mathbf{C_u}(\mathbf{u})} \overbrace{\begin{bmatrix} \dot{\mathbf{u}}_\mathbf{I} \\ \dot{\mathbf{u}}_{\mathbf{T}_e} \\ \dot{\mathbf{u}}_{\mathbf{T}_e} \\ \dot{\mathbf{u}}_\mathbf{u} \end{bmatrix}}^{\dot{\mathbf{u}}} \\ & + \underbrace{\begin{bmatrix} \mathbf{K_I} & 0 & 0 & 0 \\ 0 & \mathbf{K}_{ee}(\mathbf{u}_{\mathbf{T}_l}, \mathbf{u}_{\mathbf{T}_l}) & \mathbf{K}_{el} & 0 \\ 0 & \mathbf{K}_{le} & \mathbf{K}_{ll} & 0 \\ 0 & 0 & \mathbf{K}_{\mathbf{T_l};\mathbf{u}}(\mathbf{u}_u) & \mathbf{K}_u(\mathbf{u}_u, \mathbf{u}_{\mathbf{T}_l}) \end{bmatrix}}_{\mathbf{K}(\mathbf{u})} \underbrace{\begin{bmatrix} \mathbf{u_I} \\ \mathbf{u}_{\mathbf{T}_e} \\ \mathbf{u}_{\mathbf{T}_l} \\ \mathbf{u_u} \end{bmatrix}}_{\mathbf{u}} - \underbrace{\begin{bmatrix} \mathbf{f_I} \\ 0 \\ \mathbf{f}_{\mathbf{T}_l}(\mathbf{u_u}) \\ \mathbf{f_u} \end{bmatrix}}_{\mathbf{f}(\mathbf{u})} \end{aligned} \tag{2.212}$$

The thermal expansion is implemented in the elastic stiffness matrix $\mathbf{K_u}(\mathbf{u}_u, \mathbf{u}_{\mathbf{T}_l})$ and the thermal lattice load vector $\mathbf{f}_{\mathbf{T_l}}(\mathbf{u}_u)$ depends on the displacement vector $\mathbf{u}_u$ due to the boundary condition described in table 2.9. The coupled transient FEM formulation finally relaxes to a second order ordinary differential equation. It has the form of an equation of motion

with includes inertia, damping, a restoring force and an external force. The coupled equation system 2.212 with its initial condition can be finally expressed as:

$$\mathbf{r} = \mathbf{M}\ddot{\mathbf{u}} + \mathbf{C}(\mathbf{u})\dot{\mathbf{u}} + \mathbf{K}(\mathbf{u})\mathbf{u} - \mathbf{F}(\mathbf{u}); \qquad \mathbf{u}_0 = \mathbf{u}(t=0); \qquad \dot{\mathbf{u}}_0 = \dot{\mathbf{u}}(t=0), \tag{2.213}$$

with $\mathbf{r}$, $\mathbf{M}$, $\mathbf{C}$, and $\mathbf{K}$ as the global residual, mass, damping and stiffness matrix, respectively. $\mathbf{f}$, is the global load vector. $\mathbf{C}$, $\mathbf{K}$, and $\mathbf{f}$ are functions of the global unknown solution vectors $\mathbf{u}$. This equation is still a semi-discrete equation, which means it is discretized in space and continuous in time.

2.8.5. Time discretization

Particular attention had been payed to the section of time discretization since it determines the accuracy of the transient numerical solution. A common approach to discretize the time domain in the framework of FEM are achieved by the finite difference approximation. It is based on the assumption that the time derivatives of an arbritary variable $\mathbf{u}$ can approximated by its difference quotient:[127]

$$\begin{aligned} \frac{\partial \mathbf{u}}{\partial t} &= \lim_{\Delta t \to 0} \frac{\mathbf{u}_{t+\Delta t} - \mathbf{u}_t}{\Delta t} \approx \frac{\mathbf{u}_{t+\Delta t} - \mathbf{u}_t}{\Delta t} \\ \frac{\partial^2 \mathbf{u}}{\partial^2 t} &= \lim_{\Delta t \to 0} \frac{\mathbf{u}_{t+2\Delta t} - 2\mathbf{u}_{t+2\Delta t} + \mathbf{u}_t}{\Delta t^2} \approx \frac{\mathbf{u}_{t+2\Delta t} - 2\mathbf{u}_{t+2\Delta t} + \mathbf{u}_t}{\Delta t^2} \end{aligned} \tag{2.214}$$

These methods can be distinguished between explicit and implicit. Explicit methods are characterized by a computation where the solution can be computed directly from the solution at time t while implicit methods are attributed by an implicit solution via $t + \Delta t$. Implicit methods have the advatnge that they are more stable than in the explicit case and large time step sizes can be realized. As showed earlyer in figure 2.2 the timescale of physical processes initiated by the interaction of a ultra short laser pulse with matter ranges up to ten orders of magnited from the femtoseonds to microseconds.[59] Thus, an implicit time integration scheme with an adaptive time step was the method of choice for the present study. To meet the accuracy criterion, the time step has to be around 10^{-15} s in the initial phase where large gradients of intensity, temperature and displacement appears that may initiates shock waves. Because the temperature gradients are smoothed out and the shock waves are damped with the Rayleigh damping model, the time step increases up to 10^{-9} s during the calculation which make the computational costs of the simulation acceptable. Fluences larger than 0.55 J/cm^2 may requires more mesh elements and smaller time steps to achieve convergence and were not conducted in this investigation.

The software Comsol multiphysics™ enables the selection of three different time-dependent solvers: The implicite backward differentiation formulas (BDF),[128] the generalized-α method[129] which is a umbrella therm for the HHT-α,[130] the WBZ-α[?] and CH-α[129] method and the explicite Runge-Kutta method.[131–133] Each method has its unique advantages and disadvantages depending on the particular numerical problem. In this study, an implicite generalized-α method,[129] was applied which is based on Newmarks's method.[134] The major advantage of this time integration scheme is that it is assumed to be more stable for large time step than the BDF.

2.8.6. Newmark's method

First, Newmark's method is introduced which is based on the constant average acceleration scheme. This means that the acceleration changes linearly within a time step. The method is unconditionally stable for linear structural mechanics.

In the following sections, the time steps are denoted by the subscript n for the current time step $(\cdot)_n := (\cdot)(t_n)$ and $n+1$ for the subsequent time step $(\cdot)_{n+1} = (\cdot)(t_{n+1})$, respectively. Further, m are the total number of time steps $n \in [0, 1, ..., m-1]$. The second order ODE space discretizes equation **??** is now also discetrized in time by the time approximations:

$$\mathbf{u}_{n+1} \approx \mathbf{d}_{n+1}; \qquad \dot{\mathbf{u}}_{n+1} \approx \mathbf{v}_{n+1}; \qquad \ddot{\mathbf{u}}_{n+1} \approx \mathbf{a}_{n+1}. \tag{2.215}$$

With this consideration equation 2.207 yields to:

$$\mathbf{M}\mathbf{a}_{n+1} + \mathbf{C}\mathbf{v}_{n+1} + \mathbf{K}\mathbf{d}_{n+1} - \mathbf{F}_{n+1} = 0. \tag{2.216}$$

For the time integration, this equation is only solved at discrete time steps n. The basic idea is to determine the solution of $\mathbf{d_{n+1}}$, $\mathbf{v_{n+1}}$ and $\mathbf{a_{n+1}}$ from the known values of $\mathbf{d_n}$, $\mathbf{v_n}$ and $\mathbf{a_n}$.

The Newmark's method is formulated by a time approximation of $\mathbf{d_{n+1}}$ and $\mathbf{v_{n+1}}$:

$$\mathbf{d}_{n+1} = \mathbf{d}_n + \mathbf{v}_n \Delta t + \frac{1}{2}\left((1-2\,\beta)\,\mathbf{a}_n + 2\,\beta \mathbf{a}_{n+1}\right)\Delta t^2 \tag{2.217a}$$

$$\mathbf{v}_{n+1}(\mathbf{d}_{n+1}) = \mathbf{v}_n + \left((1-\gamma)\,\mathbf{a}_n + \gamma \mathbf{a}_{n+1}\right)\Delta t. \tag{2.217b}$$

The value for $\beta \in [0, 0.5]$ and $\gamma \in [0, 1]$ has to be initialized carefully for accuracy and stabilization. Table 2.16 summarizes values for β and γ for different Newmark's method. By rearranging equation 2.217a and 2.217b they can be expressed in terms of $\mathbf{v_{n+1}}$ and $\mathbf{a_{n+1}}$:

$$\mathbf{v}_{n+1}(\mathbf{d}_{n+1}) = \frac{\gamma}{\beta \Delta t}(\mathbf{d}_{n+1} - \mathbf{d}_n) - (\frac{\gamma}{\beta} - 1)\mathbf{v}_n + \Delta t(\frac{\beta - \frac{1}{2}\gamma}{\beta})\mathbf{a}_n, \tag{2.218a}$$

$$\mathbf{a}_{n+1}(\mathbf{d}_{n+1}) = \frac{1}{\beta \Delta t^2}(\mathbf{d}_{n+1} - \mathbf{d}_n) - \frac{1}{\beta \Delta t}\mathbf{v}_n - \frac{\beta - \frac{1}{2}}{\beta}\mathbf{a}_n. \tag{2.218b}$$

The initial condition for the first time step are defined as:

$$\mathbf{d}_0 = \mathbf{u}(t=0); \quad \mathbf{v}_0 = \mathbf{v}(t=0); \quad \mathbf{a}_0 = \mathbf{M}^{-1}(\mathbf{F}(t=0) - \mathbf{C}(\mathbf{d}_0)\mathbf{v}_0 - \mathbf{K}(\mathbf{d}_0)\mathbf{d}_0)). \tag{2.219}$$

Equation 2.218a and 2.218b can now be inserted into equation **??** and **??**, respectively. This yields to the following nonlinear algebraic equation:

Method	γ	β	Type
Linear acceleration	1/2	1/6	Implicit
Constant-average acceleration (Trapezoidal rule)	1/2	1/4	Implicit
Central difference	1/2	0	Explicit

Table 2.16.: Different Newmark's methods which are characterized by the values of γ and β

$$\overbrace{\mathbf{M}\frac{\gamma}{\beta\Delta t^2}(\mathbf{d}_{n+1}-\mathbf{d}_n)-\frac{1}{\beta\Delta t}\mathbf{v}_n-\frac{\beta-\frac{1}{2}}{\beta}\mathbf{a}_n}^{\mathbf{M}\mathbf{a}_{n+1}}$$
$$+\underbrace{\mathbf{C}\frac{\gamma}{\beta\Delta t}(\mathbf{d}_{n+1}-\mathbf{d}_n)-(\frac{\gamma}{\beta}-1)\mathbf{v}_n+\Delta t(\frac{\beta-\frac{1}{2}\gamma}{\beta})\mathbf{a}_n}_{\mathbf{C}\mathbf{v}_{n+1}}+\mathbf{K}\mathbf{d}_{n+1}=\mathbf{F}_{n+1} \tag{2.220}$$

The only remaining unknown variable in equation 2.220 is $\mathbf{d}_{n+1}$ and a solution can now be achieved.

The time dsicretization for a first order ODE can be written similar to equation 2.218a by canceling γ and last therm with $\mathbf{a}_n$:[135]

$$\mathbf{v}_{n+1}(\mathbf{d}_{n+1})=\frac{1}{\beta\Delta t}(\mathbf{d}_{n+1}-\mathbf{d}_n)-(\frac{1}{\beta}-1)\mathbf{v}_n. \tag{2.221}$$

This again yields to a nonlinear algebraic equation:

$$\underbrace{\mathbf{C}\frac{1}{\beta\Delta t}(\mathbf{d}_{n+1}-\mathbf{d}_n)-(\frac{1}{\beta}-1)\mathbf{v}_n}_{\mathbf{C}\mathbf{v}_{n+1}}+\mathbf{K}\mathbf{d}_{n+1}=\mathbf{F}_{n+1} \tag{2.222}$$

With this approach, the temperature time discretization can be obtained by approximate the variable $\mathbf{d}_{n;n+1}$ and $\mathbf{v}_{n;n+1}$ with the temperature $\mathbf{u}_{\mathbf{T};n;n+1}$ and the first time derivative of the temperature $\dot{\mathbf{u}}_{\mathbf{T};n;n+1}$, respectively.

For zero-order ODEs or algebraic equations no time integration algorithm is necessary and equation 2.222 relaxes to:

$$\mathbf{K}\mathbf{d}_{n+1}=\mathbf{F}_{n+1}. \tag{2.223}$$

From this solution, the time and space discrete intensity equation arises by approximate the intensity $\mathbf{d}_{n;n+1}$ with $\mathbf{u}_{\mathbf{I};n;n+1}$.

Method	α_m	α_f
Newmark	0	0
Hilber-Hughes-Taylor (HHT)	0	
Chung-Hulbert scheme (CH)	> 0	$\neq 0$
Wood-Bossak-Zienkiewicz scheme (WBZ)		0

Table 2.17.: Conditions of α_m and α_f for common time integration methods.

2.8.7. Generalized α-method

However, although Newmark's method has shown to be A-stable (unconditionally stable) for linear structural dynamics its behavior for non-linear structural dynamics may become unstable.[136,137] An extended improved version of Newmark's method is established by the so called general-α method or CH-α method.[129] The main idea of the generalized-α method is instead of determining a solution strict at the end points t_{n+1}, to determine a solution at intermediate points $t_{n+1-\alpha_{m;f}}$ within the time step interval $\Delta t = t_{n+1} - t_n$. The value of the weighting parameters α_m and α_f define the method solution algorithm (see table 2.17). The big advantage of this procedure is that high frequency damping can occurs while low frequency damping is supressed. Thus, nummerical convergence is supported and an accurate sulutions can be achieved. Even with high time step sizes, like it was nessesery for the solution of the present model, with a time scale range of approx. 10 orders of magnited, this algorythm is the mehtod of choise.[138]The general-α method can now be applied to the initial value problem for non-linear structural dynamics of equation 2.207. First, the general trapezoid rule is may applied to $\mathbf{d}$, $\mathbf{v}$ and $\mathbf{a}$:

$$\mathbf{d}_{n+1-\alpha_f} = (1-\alpha_f)\mathbf{d}_{n+1} + \alpha_f \mathbf{d}_n \tag{2.224a}$$
$$\mathbf{v}_{n+1-\alpha_f} = (1-\alpha_f)\mathbf{v}_{n+1} + \alpha_f \mathbf{v}_n \tag{2.224b}$$
$$\mathbf{a}_{n+1-\alpha_m} = (1-\alpha_m)\mathbf{a}_{n+1} + \alpha_m \mathbf{a}_n \tag{2.224c}$$

The general trapezoid rule is may also applied to the internal and external forces.

$$\mathbf{K}_{n+1-\alpha_f} = (1-\alpha_f)\mathbf{K}(\mathbf{d}_{n+1}) + \alpha_f \mathbf{K}\mathbf{d}_n \tag{2.225a}$$
$$\mathbf{F}_{n+1-\alpha_f} = (1-\alpha_f)\mathbf{F}(\mathbf{d}_{n+1}) + \alpha_f \mathbf{F}\mathbf{d}_n \tag{2.225b}$$

The internal forces may also approximated by the generalized mid-point-rule (MR) or the generalized energy-momentum rule (GEMR).[137] The parameter $\alpha_{m/f}$, β and γ are defined as:[136]

$$\alpha_m = \frac{2\rho_\infty - 1}{\rho_{\infty+1}}; \qquad \alpha_f = \frac{\rho_\infty}{1+\rho_\infty}; \quad \beta = \frac{1}{(1+\rho_\infty)^2}; \qquad \gamma = \frac{1}{2}\frac{3-\rho_\infty}{1+\rho_\infty}; \tag{2.226}$$

with the maximum spectral radius $\rho_\infty \in [0,1]$ which is a key factor since it controls the numerical dissipation. The spectral radius is in general defined as the maximum absolute eigenvalue of a square matrix or a bounded linear operator. With the case of $\rho_\infty = 0$ asymptotic annihilation of the high-frequency response is achieved and $\rho_\infty = 1$ corresponds to the

case of no algorithmic dissipation. In the present study ρ_∞ was set to 0.75 to achieve a good balance between high-frequency response and algorithmic dissipation.

The complete space and time disctretized equation for a second-order ODE according to the general-α method can be written as:

$$\mathbf{M}\mathbf{a}_{n+1-\alpha_m} + \mathbf{C}\mathbf{v}_{n+1-\alpha_f} + \mathbf{K}\mathbf{d}_{n+1-\alpha_f} = \mathbf{f}_{n+1-\alpha_f}, \tag{2.227}$$

By inserting equations 2.224 into equation 2.227, it yields to:

$$\begin{aligned}&(1-\alpha_m)\mathbf{M}\mathbf{a}_{n+1} + \alpha_m\, \mathbf{M}\mathbf{a}_n + \\ &(1-\alpha_f)\mathbf{C}(\mathbf{d}_{n+1})\mathbf{v}_{n+1} + \alpha_f\mathbf{C}(\mathbf{d}_n)\mathbf{v}_n + (1-\alpha_f)\mathbf{K}(\mathbf{d}_{n+1}) + \alpha_f\mathbf{K}(\mathbf{d}_n) - (1-\alpha_f)\mathbf{F} + \alpha_f\mathbf{F} = 0\end{aligned} \tag{2.228}$$

For a first-order ODE equation 2.227 and equation 2.228 relaxes to:

$$\mathbf{C}\mathbf{v}_{n+1-\alpha_m} + \mathbf{K}\mathbf{d}_{n+1-\alpha_f} = \mathbf{f}_{n+1-\alpha_f}, \tag{2.229}$$

and to:

$$(1-\alpha_m)\mathbf{C}(\mathbf{d}_{n+1})\mathbf{v}_{n+1} + \alpha_m\mathbf{C}(\mathbf{d}_n)\mathbf{v}_n + (1-\alpha_f)\mathbf{K}(\mathbf{d}_{n+1}) + \alpha_f\mathbf{K}(\mathbf{d}_n) - (1-\alpha_f)\mathbf{F} + \alpha_f\mathbf{F} = 0. \tag{2.230}$$

The general-α method applied to a zero-order ODE or algebraic equation like the time disretized intensity equation it may expands to:

$$\mathbf{K}\mathbf{d}_{n+1-\alpha_m} = \mathbf{f}_{n+1-\alpha_f} \tag{2.231}$$

The generalized-α method applied to the fully coupled equation 2.212 finally yields to:

$$\overbrace{\begin{bmatrix}\mathbf{r}_i\\ \mathbf{r}_e\\ \mathbf{r}_l\\ \mathbf{r}_u\end{bmatrix}}^{\mathbf{r}} = \overbrace{\begin{bmatrix}0&0&0&0\\0&0&0&0\\0&0&0&0\\0&0&0&\mathbf{M_u}\end{bmatrix}}^{\mathbf{M}}\overbrace{\begin{bmatrix}\mathbf{a_I}\\ \mathbf{a}_{\mathbf{T}_e}\\ \mathbf{a}_{\mathbf{T}_e}\\ \mathbf{a_u}\end{bmatrix}}^{\mathbf{a}} + \overbrace{\begin{bmatrix}0&0&0&0\\0&\mathbf{C}_e(\mathbf{d}_{\mathbf{T}_e})&0&0\\0&0&\mathbf{C}_l(\mathbf{d}_{\mathbf{T}_l})&0\\0&0&0&\mathbf{C_u}(\mathbf{d_u})\end{bmatrix}}^{\mathbf{C(v)}}\overbrace{\begin{bmatrix}\mathbf{v_I}\\ \mathbf{v}_{\mathbf{T}_e}\\ \mathbf{v}_{\mathbf{T}_e}\\ \mathbf{v_u}\end{bmatrix}}^{\mathbf{v}} + \underbrace{\begin{bmatrix}\mathbf{K_I}&0&0&0\\0&\mathbf{K}_{ee}(\mathbf{d}_{\mathbf{T}_l},\mathbf{d}_{\mathbf{T}_l})&\mathbf{K}_{el}&0\\0&\mathbf{K}_{le}&\mathbf{K}_{ll}&0\\0&0&\mathbf{K}_{\mathbf{T_l;u}}(\mathbf{d}_u)&\mathbf{K}_u(\mathbf{d}_u)\end{bmatrix}}_{\mathbf{K(d)}}\underbrace{\begin{bmatrix}\mathbf{d_I}\\ \mathbf{d}_{\mathbf{T}_e}\\ \mathbf{d}_{\mathbf{T}_l}\\ \mathbf{d_u}\end{bmatrix}}_{\mathbf{d}} - \underbrace{\begin{bmatrix}\mathbf{f_I}\\0\\ \mathbf{f}_{\mathbf{T}_l}(\mathbf{d_u})\\ \mathbf{f_u}(\mathbf{d}_{\mathbf{T}_l})\end{bmatrix}}_{\mathbf{f(d)}} \tag{2.232}$$

2.9. Solution algorithm: Newton-Raphson method

The Newton-Raphson method is a fundamental FEM algorithm for finding the roots of a real valued function $\mathbf{f}(\mathbf{x})$.[139] This function is linearized at a certain point $\mathbf{x}^i$ by its tangent. According to Taylor's theorem, this tangent $\mathbf{t}(\mathbf{x})$ can be expressed by neglecting second and higher order derivative therms denoted by $\mathcal{O}$:

$$\mathbf{t}(\mathbf{x}) = \mathbf{f}(\mathbf{x}^i) + \mathbf{f}'(\mathbf{x}^\mathbf{i})\big|_i(\mathbf{x} - \mathbf{x}^i) + \underbrace{\mathcal{O}}_{=0} \tag{2.233}$$

The iteration steps are denoted by the superscript i for the current iteration step $(\cdot)^i = (\cdot)(i)$ and $i+1$ for the subsequent iteration step $(\cdot)^{i+1} = (\cdot)(i+1)$, respectively. The iterations are performed within each time step $t_n; t_{n+1}$. Several iteration steps may has to be performed until convergence is reached. If a start value $\mathbf{x}^0$ is given, the function $\mathbf{f}(\mathbf{x}^0)$ and its derivative $\mathbf{f}'(\mathbf{x})\big|_0$ (with respect to $\mathbf{x}$) can be evaluated at this point. The iteration scheme is performed by finding the root of the tangent $\mathbf{t}(\mathbf{x})$ and using the corresponding $\mathbf{x}$ for the subsequent iteration step $i+1$. This can be achieved by setting $\mathbf{t}(\mathbf{x}) = 0$ and $\mathbf{x} = \mathbf{x}^{i+1}$. It is important to emphasis that the Newton-Raphson method only converges if the solution is differentiable and continuous. The iteration scheme then becomes:

$$\mathbf{x}^{i+1} = \mathbf{x}^i - \frac{\mathbf{f}(\mathbf{x}^i)}{\mathbf{f}'(\mathbf{x}^i)\big|_i} \tag{2.234}$$

Exemplary, the first six Newton-Rapshon iterations are illustrated in figure 2.28 for an arbitrary one-dimensional function $f(x) = -xe^x + 3$. With each increasing iteration step the root of the function converges.

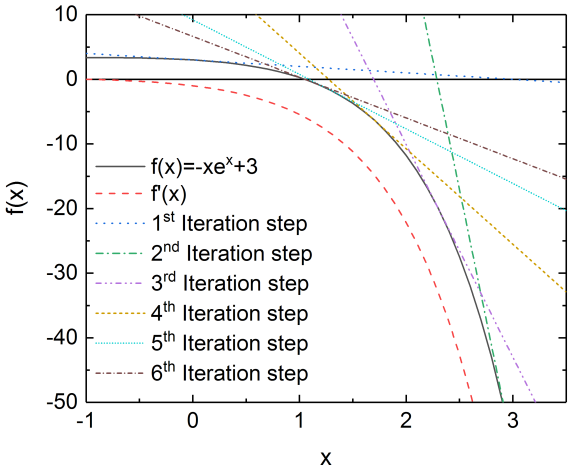

Figure 2.28.: Visualization of the Newton Raphson algorithm for a single degree of freedom system. An arbitrary chosen function $f(x) = -xe^x + 3$ is used to show six iteration steps.

The Newton-Raphson method is also applicable to multi-variable functions. Thus, the fully discretized nonlinear algebraic coupled equation system 2.232 was solved by this method. The global residual $\mathbf{r}(\mathbf{d}^i_{n+1})$ has the following form:

$$\mathbf{r}(\mathbf{d}^i_{n+1}) = \mathbf{M}\mathbf{a}^i_{n+1-\alpha_m} + \mathbf{C}\mathbf{v}^i_{n+1-\alpha_f} + \mathbf{K}\mathbf{d}^i_{n+1-\alpha_f} - \mathbf{f}_{n+1-\alpha_f} \tag{2.235}$$

The solution vector can be expanded in the following way:

$$\mathbf{d}^{i;i+1}_{n;n+1} = \begin{bmatrix} \mathbf{d}^{i;i+1}_{\mathbf{I};n;n+1} & \mathbf{d}^{i;i+1}_{\mathbf{T_e};n;n+1} & \mathbf{d}^{i;i+1}_{\mathbf{T_l};n;n+1} & \mathbf{d}^{i;i+1}_{\mathbf{u};n;n+1} \end{bmatrix}^T \tag{2.236}$$

The tangent $\mathbf{t}(\mathbf{d}_{n+1})$ of equation 2.235 is defined as:

$$\mathbf{t}(\mathbf{d}_{n+1}) = \mathbf{r}(\mathbf{d}^i_{n+1}) + \left.\frac{\partial \mathbf{r}(\mathbf{d}_{n+1})}{\partial \mathbf{d}_{n+1}}\right|^i (\mathbf{d}_{n+1} - \mathbf{d}^i_{n+1}) \tag{2.237}$$

Now, the tangent is set to zero $\mathbf{t}(\mathbf{d}^i_{n+1}) = 0$ and corresponding solution vector $\mathbf{d}^i_{n+1}$ is set as the value for the subsequent iteration $\mathbf{d}^{i+1}_{n+1}$. Equation 2.237 than becomes the well known Newton-Raphson iteration algorithm for multi-variable equations:

$$\mathbf{d}^{i+1}_{n+1} = \mathbf{d}^i_{n+1} - \frac{\mathbf{r}(\mathbf{d}^i_{n+1})}{\left\{\left.\frac{\partial \mathbf{r}(\mathbf{d}_{n+1})}{\partial \mathbf{d}_{n+1}}\right|^i\right\} \mathbf{K}_t(\mathbf{d}^i_{n+1})} \tag{2.238}$$

The derivative of $\mathbf{r}(\mathbf{d}_{n+1})$ with respect to $\mathbf{d}_{n+1}$ at i is the so called global tangent stiffness matrix $\mathbf{K}_t$, which is defined as:

$$\begin{aligned} &\mathbf{K}_t\left(\mathbf{d}^i_{n+1}\right) := \left.\frac{\partial \mathbf{r}(\mathbf{d}_{n+1})}{\partial \mathbf{d}_{n+1}}\right|^i = \\ &\underbrace{\frac{\partial \mathbf{M}\mathbf{a}^i_{n+1-\alpha_m}}{\partial \mathbf{d}^i_{n+1}}}_{\mathbf{K_M}} + \underbrace{\frac{\partial \mathbf{C}(\mathbf{d}^i_{n+1-\alpha_f})\mathbf{v}^i_{n+1-\alpha_f}}{\partial \mathbf{d}^i_{n+1}}}_{\mathbf{K_C}} + \underbrace{\frac{\partial \mathbf{K}(\mathbf{d}^i_{n+1-\alpha_f})\mathbf{d}^i_{n+1-\alpha_f}}{\partial \mathbf{d}^i_{n+1}}}_{\mathbf{K_K}} - \underbrace{\frac{\partial \mathbf{f}(\mathbf{d}^i_{n+1-\alpha_f})}{\partial \mathbf{d}^i_{n+1-\alpha_f}}}_{\mathbf{K_f}}. \end{aligned} \tag{2.239}$$

By applying the chain rule, the complete global tangent stiffness matrix expands to:

$$\mathbf{K}_t\left(\mathbf{d}_{n+1}^i\right) :=$$

$$\begin{bmatrix} \left.\frac{\partial \mathbf{r}_\mathbf{I}(\mathbf{d}_\mathbf{I})_{n+1}}{\partial \mathbf{d}_{\mathbf{I};n+1}}\right|^i & \left.\frac{\partial \mathbf{r}_\mathbf{I}(\mathbf{d}_\mathbf{I})_{n+1}}{\partial \mathbf{d}_{\mathbf{Te};n+1}}\right|^i & \left.\frac{\partial \mathbf{r}_\mathbf{I}(\mathbf{d}_\mathbf{I})_{n+1}}{\partial \mathbf{d}_{\mathbf{Tl};n+1}}\right|^i & \left.\frac{\partial \mathbf{r}_\mathbf{I}(\mathbf{d}_\mathbf{I})_{n+1}}{\partial \mathbf{d}_{\mathbf{u};n+1}}\right|^i \\ \left.\frac{\partial \mathbf{r}_{\mathbf{T_e}}(\mathbf{d}_{\mathbf{Te}},\mathbf{d}_{\mathbf{Tl}})_{n+1}}{\partial \mathbf{d}_{\mathbf{I};n+1}}\right|^i & \left.\frac{\partial \mathbf{r}_{\mathbf{T_e}}(\mathbf{d}_{\mathbf{Te}},\mathbf{d}_{\mathbf{Tl}})_{n+1}}{\partial \mathbf{d}_{\mathbf{Te};n+1}}\right|^i & \left.\frac{\partial \mathbf{r}_{\mathbf{T_e}}(\mathbf{d}_{\mathbf{Te}},\mathbf{d}_{\mathbf{Tl}})_{n+1}}{\partial \mathbf{d}_{\mathbf{Tl};n+1}}\right|^i & \left.\frac{\partial \mathbf{r}_{\mathbf{T_e}}(\mathbf{d}_{\mathbf{Te}},\mathbf{d}_{\mathbf{Tl}})_{n+1}}{\partial \mathbf{d}_{\mathbf{u};n+1}}\right|^i \\ \left.\frac{\partial \mathbf{r}_{\mathbf{T_l}}(\mathbf{d}_{\mathbf{Tl}},\mathbf{d}_{\mathbf{Te}})_{n+1}}{\partial \mathbf{d}_{\mathbf{I};n+1}}\right|^i & \left.\frac{\partial \mathbf{r}_{\mathbf{T_l}}(\mathbf{d}_{\mathbf{Tl}},\mathbf{d}_{\mathbf{Te}})_{n+1}}{\partial \mathbf{d}_{\mathbf{Te};n+1}}\right|^i & \left.\frac{\partial \mathbf{r}_{\mathbf{T_l}}(\mathbf{d}_{\mathbf{Tl}},\mathbf{d}_{\mathbf{Te}})_{n+1}}{\partial \mathbf{d}_{\mathbf{Tl};n+1}}\right|^i & \left.\frac{\partial \mathbf{r}_{\mathbf{T_l}}(\mathbf{d}_{\mathbf{Tl}},\mathbf{d}_{\mathbf{Te}})_{n+1}}{\partial \mathbf{d}_{\mathbf{u};n+1}}\right|^i \\ \left.\frac{\partial \mathbf{r}_{\mathbf{u}}(\mathbf{d}_{\mathbf{u}},\mathbf{d}_{\mathbf{Tl}})_{n+1}}{\partial \mathbf{d}_{\mathbf{I};n+1}}\right|^i & \left.\frac{\partial \mathbf{r}_{\mathbf{u}}(\mathbf{d}_{\mathbf{u}},\mathbf{d}_{\mathbf{Tl}})_{n+1}}{\partial \mathbf{d}_{\mathbf{Te};n+1}}\right|^i & \left.\frac{\partial \mathbf{r}_{\mathbf{u}}(\mathbf{d}_{\mathbf{u}},\mathbf{d}_{\mathbf{Tl}})_{n+1}}{\partial \mathbf{d}_{\mathbf{Tl};n+1}}\right|^i & \left.\frac{\partial \mathbf{r}_{\mathbf{u}}(\mathbf{d}_{\mathbf{u}},\mathbf{d}_{\mathbf{Tl}})_{n+1}}{\partial \mathbf{d}_{\mathbf{u};n+1}}\right|^i \end{bmatrix}. \tag{2.240}$$

Some entries of the global stiffness matrix relaxes to zero due to the missing variable dependency within its function:

$$\mathbf{K}_t\left(\mathbf{d}_{n+1}^i\right) :=$$

$$\begin{bmatrix} \left.\frac{\partial \mathbf{r}_\mathbf{I}(\mathbf{d}_\mathbf{I})_{n+1}}{\partial \mathbf{d}_{\mathbf{I};n+1}}\right|^i & 0 & 0 & 0 \\ 0 & \left.\frac{\partial \mathbf{r}_{\mathbf{T_e}}(\mathbf{d}_{\mathbf{Te}},\mathbf{d}_{\mathbf{Tl}})_{n+1}}{\partial \mathbf{d}_{\mathbf{Te};n+1}}\right|^i & \left.\frac{\partial \mathbf{r}_{\mathbf{T_e}}(\mathbf{d}_{\mathbf{Te}},\mathbf{d}_{\mathbf{Tl}})_{n+1}}{\partial \mathbf{d}_{\mathbf{Tl};n+1}}\right|^i & 0 \\ 0 & \left.\frac{\partial \mathbf{r}_{\mathbf{T_l}}(\mathbf{d}_{\mathbf{Tl}},\mathbf{d}_{\mathbf{Te}})_{n+1}}{\partial \mathbf{d}_{\mathbf{Te};n+1}}\right|^i & \left.\frac{\partial \mathbf{r}_{\mathbf{T_l}}(\mathbf{d}_{\mathbf{Tl}},\mathbf{d}_{\mathbf{Te}})_{n+1}}{\partial \mathbf{d}_{\mathbf{Tl};n+1}}\right|^i & 0 \\ 0 & 0 & \left.\frac{\partial \mathbf{r}_{\mathbf{u}}(\mathbf{d}_{\mathbf{u}},\mathbf{d}_{\mathbf{Tl}})_{n+1}}{\partial \mathbf{d}_{\mathbf{Tl};n+1}}\right|^i & \left.\frac{\partial \mathbf{r}_{\mathbf{u}}(\mathbf{d}_{\mathbf{u}},\mathbf{d}_{\mathbf{Tl}})_{n+1}}{\partial \mathbf{d}_{\mathbf{u};n+1}}\right|^i \end{bmatrix}. \tag{2.241}$$

The Newton-Raphson algortythm requires to compute the inverse of the global stiffness matrix $\mathbf{K}_t$ according to equation 2.238. This is commonly achieved in the FEM framework by the method LU decomposition.[140] With equation 2.238 a linear equation system can be produced.

$$\mathbf{K}_t(\mathbf{d}_{n+1}^i) \underbrace{\Delta \mathbf{d}_{n+1}^{i+1}}_{\mathbf{d}_{n+1}^{i+1}-\mathbf{d}_{n+1}^i} = -\mathbf{r}(\mathbf{d}_{n+1}^i) \tag{2.242}$$

The solution vector $\mathbf{d}_{n+1}^{i+1}$ can be computed from the sum of its previous iteration step $\mathbf{d}_{n+1}^i$ and the incremental solution vector $\Delta \mathbf{d}_{n+1}^{i+1}$:

$$\mathbf{d}_{n+1}^{i+1} = \mathbf{d}_{n+1}^i + \Delta \mathbf{d}_{n+1}^{i+1} \tag{2.243}$$

This linear equation system 2.242 was computed by the so-called parallel sparse direct linear solver MUMPS (**MU**ltifrontal **M**assively **P**arallel sparse direct **S**olver).[141] This solver supports multithreading and worked excellent for the present large DOF systems. Actually, the software Comsol Multiphysics™ uses an additional damping factor $\lambda \in [0,1]$ if the absolute value of a global residual solution is greater than those of the previous step ($\left|\mathbf{r}(\mathbf{d}_{n+1}^{i+1})\right| > \left|\mathbf{r}(\mathbf{d}_{n+1}^{i})\right|$). The advantage of this procedure is, that the computational costs are reduced by decreasing the iteration steps.[142,143] The damped solution vector is computed by:

$$\mathbf{d}_{n+1}^{damped} = \mathbf{d}_{n+1}^{i} + \lambda\, \Delta\mathbf{d}_{n+1}^{i+1} \tag{2.244}$$

If $\left|\mathbf{r}(\mathbf{d}_{n+1}^{damped})\right| > \left|\mathbf{r}(\mathbf{d}_{n+1}^{i})\right|$ then the damping factor λ is reduced and $\mathbf{d}_{n+1}^{damped}$ is recomputed until $\left|\mathbf{r}(\mathbf{d}_{n+1}^{damped})\right| < \left|\mathbf{r}(\mathbf{d}_{n+1}^{i})\right|$. Then, the iteration procedure is restated by setting the final damped solution as the new starting point $\mathbf{d}_{n+1}^{i,new} := \mathbf{d}_{n+1}^{damped}$.

$$\mathbf{d}_{n+1}^{i+1} = \mathbf{d}_{n+1}^{i,new} + \Delta\mathbf{d}_{n+1}^{i+1} \tag{2.245}$$

For the convergence criteria, the estimated error $\mathbf{E_r}$ is defined by the absolute value of the incremental solution vector $\left|\Delta\mathbf{d}_{n+1}^{i+1}\right|$ in the following way:

$$\mathbf{E_r} := \left|\Delta\mathbf{d}_{n+1}^{i+1}\right| = \left|\mathbf{d}_{n+1}^{i+1} - \mathbf{d}_{n+1}^{i}\right| \tag{2.246}$$

The convergence is reached and the iteration steps for a specific time step are completed if the relative error err is smaller or equal than the relative tolerance $\epsilon_{r;tol}$.

$$err = \sqrt{\left(\frac{1}{N}\sum_{i=1}^{N}\left(\frac{\left|\mathbf{E}_{n+1}^{i}\right|}{W_{n+1}^{i}}\right)^{2}\right)} \leq \epsilon_{r;tol}; \qquad \text{with} \quad W_{n+1}^{i} = max(\left|d_{n+1}^{i}\right|, S_{n+1}^{i}) \tag{2.247}$$

here, N is the number for the degree of freedom and S_{n+1}^{i} is a scale factor. The subsequent time steps can be performed by the same procedure as described in this section until the last time step m is computed and the complete solution is obtain. The explanation of the adaptive time stepping method for the generalized-α method is beyond the scope of this work and the interssting reader is refered to e.g.[144]

3. Results

3.1. Analytic model of confined laser ablation

Figure 3.1 shows a confocal microscopy image of the confined Mo-thin fim ablation on glass substarte with a picosecond laser sorce by Heise et al.[145] The bulging of the Mo-thin film is clearly visible by a stable blisters below the ablation threshold fluence. Above the ablation threshold fluence the ablated blisters can be recollected as intact domes. In the bottom of the trench, the damage free glass substrate is visible.

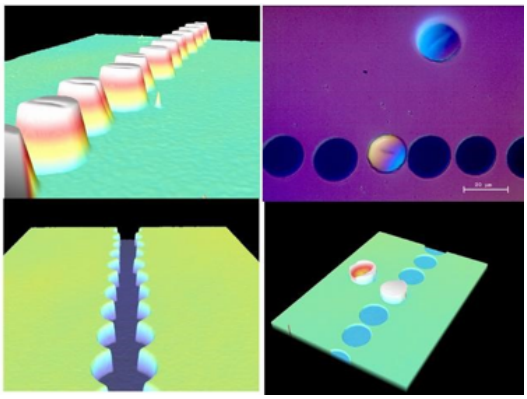

Figure 3.1.: Confocal microscopy images of a confined laser ablation of a Mo layer coated on glass subtrate with a laser pulse duration of 10 *ps* and a wavelength of 1064 *nm*. (Picture and caption obtained from Heise et. al[145]).

In previous works, laser lift-off or confined laser ablation with short and ultra-short laser pulses is reported as a gas expansion or "bubble blow up".[25,35,36] Figure 3.2 shows a schematic of the energy conversation model developed by Heise et al.[25] This model is based on the assumption that the laser energy is absorbed homogeneously in the Mo-layer within a depth in the order of the optical absorption length (few tens of nm), as shown in figure 3.2a. A part of this depth is then instantaneously evaporated to an ideal gas which occupies a cylindrical volume V_1 with a diameter of the ablated hole. The energy E_0 needed for the evaporation of the Volume V_1 is determined by:

$$E_0 = V_1 \rho \left(C_p * (T_V - T_0) + \Delta H_V \right) \tag{3.1}$$

with C_p as the heat capacity, ρ as the density and ΔH_V as the total evaporation enthalpy of Mo. T_V and T_0 are the evaporation temperature of Mo and the room temperature, respectively.

An arising gas pressure p_1 inside the evaporated volume V_1 initiates an adiabatic expansion of the Mo-layer as shown in figure 3.2b and results in a hydrostatic pressure p_2 within a volume V_2 as shown in figure 3.2c. This describs the formation process of the blister in the scope of the

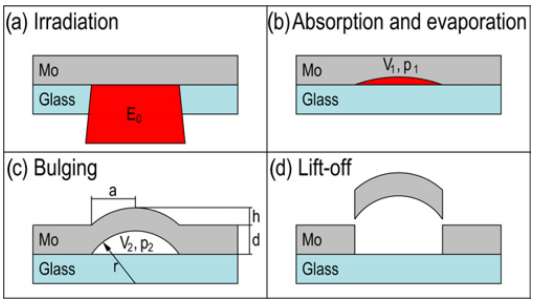

Figure 3.2.: "Model for the ablation mechanism of induced laser ablation. (a) A molybdenum layer is irradiated from the glass side at a defined pulse energy E0. (b) The pulse energy is absorbed within a thin interface layer of the molybdenum, whereupon instantaneous evaporation of the molybdenum interface initiates an ideal gas phase with volume V1 of bulk molybdenum (supercritical Mo state). (c) The molybdenum layer is bulged by an adiabatic expansion of the ideal gas up to volume V2, while the maximum of V2 is defined by the tensile stress limit. (d) If the deformation of the cap exceeds the stress limit, the molybdenum cap shears off and subsequently lifts off. No melting effects can be detected at the substrate and remaining side walls."(Figure and caption optained from Heise et. al.[25]).

model. The pressure p_1 is calculated by the ideal gas law in equation 3.2a and the pressure p_2 with means of the so-called hoop formula in equation 3.2b.[146] The volume V_2 in equation 3.2c is obtained by geometric considerations with data from profilometry measurements of the dome.

$$p_1 = \frac{\rho}{M_{Mo}} R_M T_V \tag{3.2a}$$

$$p_2 = \sigma_{shear} \frac{2d}{a} \tag{3.2b}$$

$$V_1 = \left(\frac{p_1}{p_2}\right)^{\varkappa} V_2. \tag{3.2c}$$

Here, M_{Mo} is the molar mass of Mo, R_M is the molar gas constant and $\varkappa$ is the adiabatic exponent; d and a is the film thickness and the dome radius, respectively according to figure 3.2c.

The criteria for ablation is defined when a shear stress limit σ_{shear} of 1 GPa is exceeded at the edged of the dome (see figure 3.2d). In the framework of this model, an energy of 0.25 μJ for the exceeding of this shear stress limit is predicted. The Energy E_0 is finally obtained by inserting the Volume V_1 in equation 3.1. By comparing the value of 0.25 μJ obtained from this model with the pulse energy threshold needed for a punched out dome of 1 μJ it turns out that the model underestimates the needed energy, however the values are in the same order of magnitude. In the introduced model thermal expansion was not implicated and it was not possible to include transient effects. In the present work the contribution of time-dependent effects including phase transitions and thermal expansions are explored by the means of numerical simulation.

3.2. Simulation model of confined laser ablation

As described in section 2.3, a multitime-scale simulation was necessary to take transient contributing effects into account. The complete simulation was done with three different laser peak fluences of 0.40, 0.50 and 0.55 J/cm^2. The center of the laser pulse was shifted to 30 ps in the time domain to implement the full contribution of its rising slope. The results are presented according to figure 2.3 with 4 different points of interests in the spacial domain: Point 1 is located at the Mo-glass interface and in the spacial center of the laser pulse. Point 2 is then vertically shifted of 435 nm to the Mo-bottom surface. Point 3 and 4 are each horizontally shifted with a distance of 30 μm with respect to point 1 and 2, respectively. The laser pulse had a beam radius of 21 μm (1/e^2 intensity level).

3.3. Absorption, electron heating, electron-phonon scattering, and phase transitions

Figure 3.3(a) contains data of the laser pulse intensity at the center point 1 in dependence on time. The shown intensity is plotted for three different laser peak fluences of 0.40, 0.50 and 0.55 J/cm^2. The solid lines represent the data from the calculation referring to equation 2.20 and the included symbols are data points obtained from the simulated intensity. The data of the calculation and the simulation matches perfectly which indicates the validity of the simulated intensity. It is worth mentioning that the intensity at point 3 drops down to 1.8 % of the initial maximum intensity at point 1.

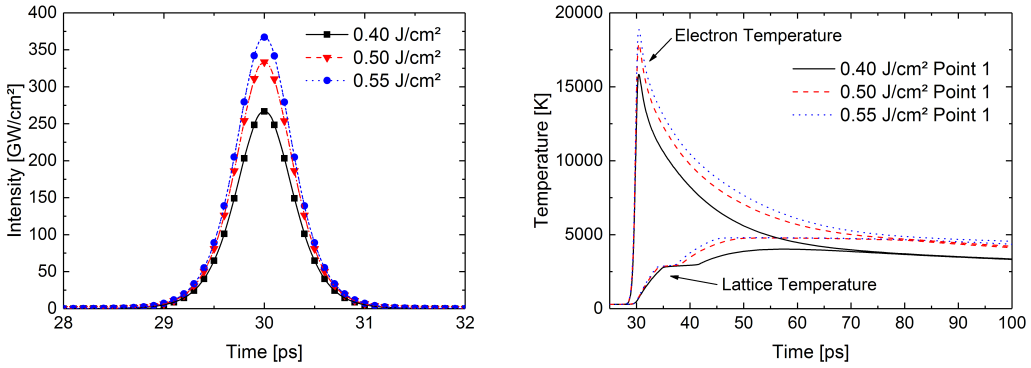

(a) (b)

Figure 3.3.: (a) Intensity of the laser pulse at the center point 10 for a peak fluences are 0.40, 0.50 and 0.55 J/cm^2, the pulse duration is 660 fs and the wavelength 1053 nm. (b) Electron and lattice temperature at the center point 1. Both temperatures have reached equilibrium after about 80 ps for all fluences.

Figure 3.3(b) shows the electron and lattice temperature in dependence on time during and after the laser pulse irradiation of the sample for a fluence of 0.40, 0.50 and 0.55 J/cm^2 at point 1. The photons of the laser pulse are absorbed by the nearly free electrons through inverse bemsstrahlung and increasing their energy level by interbandabsorption.[3] Here, a fully thermalized electron system was considered with a defined temperature distribution. The temperature of the electron subsystem increases rapidly during the laser pulse absorption to

a peak temperature of ∼19,000 K. The lattice subsystem is heated nearly instantaniously through electorn-phonon coupling. The electron and lattice subsystem reaches equilibrium at a time of 80 to 100 ps for all simulated fluences. At about 35 ps the rising latice temperature remains at a constant level for 3 to 5 ps. During this time period, the melting process is expected[68] and the thermal energy is used for the latent heat of melting during the phase transition while the temperature remains constant. A second range with no rise in temperature can be observed at about 50 ps[147,148] for a fluence of 0.50 and 0.55 J/cm^2 which originates from the latent heat of vaporization.

Figure 3.4(a) contains the lattice temperature at the points 1 to 4 versus the complete time scale of up to 10 μs for the simulation. The entire layer is resolidified after around 400 ps. This is indicated after a third time intervall of nearly constant temperature. At 1 ns the Mo-layer is almost in thermal equilibrium in the vertical direction between point 1 and 2. The resolidified Mo cools further down to the initial room temperature in the time frame of 1 ns to 10 μs. The points 3 and 4 are only slightly heated to 500 K during the hole process because of the spacial distance from the laser absorption center. This only slightly heating at the top of the dome is supported by previous works from Heise et al.[25] Here, a Mo-coated glass substrate was irradiated through the glass side with a flunece of 0.15 J/cm^2 by an ultra short laser pulse with 10 ps pulse duration and 1064 nm wavelength. A dome was produced and studied by means of atomic force microscopy (AFM). The measured mean grain size was around 40 nm, both on top of the dome and on the outer area (see Figure 3.4(b)).[25] This indicates that no thermal structure changes has occurred on top of the Mo-layer during the laser processing, like it is predicted in the present simulation results.

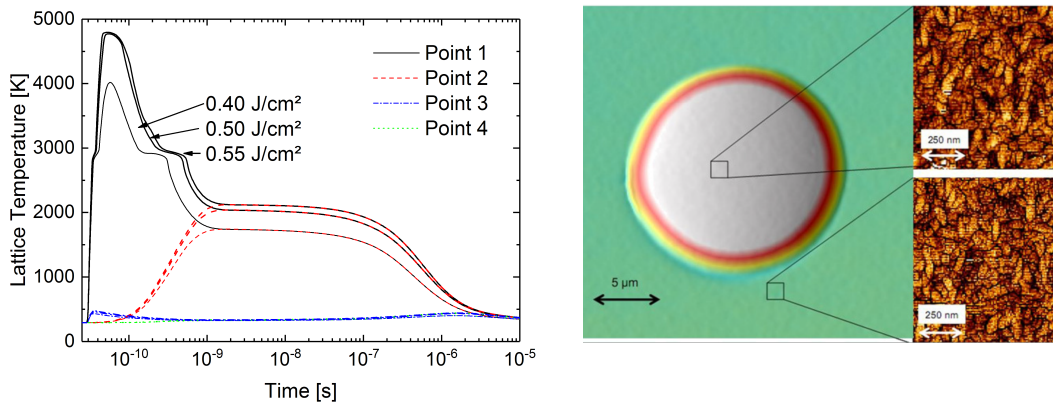

(a) (b)

Figure 3.4.: (a) Lattice temperature at the monitor points 1 to 4 at a fluence of 0.40, 0.50 and 0.55 J/cm^2. After around 400 ps the layer is solidifiedat point 1; this is indicated by the end of the temperature plateau. Time to reach a homogeneous temperature in vertical direction is about 1 ns. Outer points 3 and 4 are only slightly heated up to 500 K. Room temperature is reached after about 10 μs. (b) AFM-image of a Mo-dome produced with a fluence of 0.15 J/cm^2, 10 ps pulse duration and 1064 nm wavelength (Figure and caption optained from Heise et. al[25]). No deviations of the mean grain size of about 40 nm at the top of the dome (top right) and the outer area (bottom right) are observed which indicates no thermal structure changes.

3.4. Acceleration of the molybdenum layer and shock wave observation

The lattice temperature reaches the vaporization temperature at approx. 50 ps (see Figure 3.4(a), point 1 at 0.55 J/cm^2), and thus 20 ps after the intensity maximum of the laser pulse. If the vapor temperature is exceeded inside a certain Mo volume, a vapor pressure are able to arise. Figure 3.5 compares between the resulting vapor pressure, determined at the temperature of point 1 (left y-axis) by equation 2.2 in section d and the simulated mean vertical pressure, averaged over boundary $\partial\Omega_4$ inside the molybdenum film (right y-axis), for a fluence of 0.55 J/cm^2. The maximum vapor pressure of 75 kPa is reached at about 54 ps and nearly vanishes completely after about 150 ps due to recondensation. In contrast, at 40 ps the mean vertical pressure already reaches a minimum of -2 GPa, which is related to compressive stress, caused by the confined thermal expansion of the Mo near the Mo-glass interface during ultra-fast heating and melting. The heating rate is in the order of 10^{15} K/s and thus the thermal expansion occurs also on a ultra fast time scale, which evidently initiates a shock wave.

Figure 3.6 contains the average acceleration (averaged over the vertical direction from point 1 to 2) of the entire film thickness in dependence on time. The maximum acceleration was calculated to be $1.2{\cdot}10^{12}$ m/s^2, which corresponds to an acceleration of 10^{11} multiple of g (gravity of earth) at 40 ps. This results from thermal expansion during heating and from the phase transition during melting.

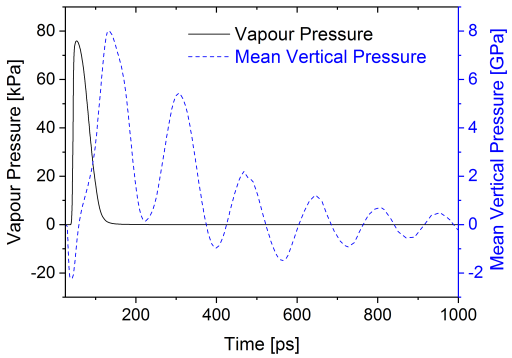

Figure 3.5.: Vapour pressure (determined at the temperature of point 1) and mean vertical stress component (averaged over the vertical direction from point 1 to 2) for a fluence of 0.55 J/cm^2. Vapor pressure does not exceed 75 kPa and has nearly vanished after 100 ps. The average vertical stress component is initially compressive (negative) and then reaches values up to 8 GPa. After the layer has detached from the substrate, the sign is alternating and is related to the thickness oscillation of the layer triggered by the expansion shock

The physical mechanisms that lead to the acceleration of the Mo-film are revealed in detail in Figure 3.7. The displacement of points 1 and 2 relative to its initial position is plotted versus the time. The Mo at point 1 is initially heated by the laser pulse at the center of the Mo-glass interface and starts to expand thermally. After about 100 ps, point 1 has propagated 10 nm into the glass substrate while point 2 is still at its initial position. The spring model at the mechanical boundary condition $\partial\Omega_4$ (see Figure 2.21 and table 2.12) which represents the adjacent glass domain creates a reset force due to the thermal expansion which results in an acceleration of point 1 in the opposite direction away from the substrate. As a result, the

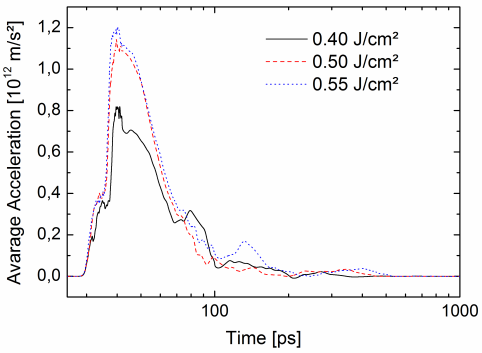

Figure 3.6.: Average acceleration (averaged over the vertical direction from point 1 to 2) in the centre for fluence of 0.40, 0.50 and 0.55 J/cm^2. First the layer accelerates by thermal expansion and the following backward impulse of the substrate in the order of 10^{11} multiple of g for all values of fluence. If the Mo layer is uncoupled from the glass substrate at 130 ps, the acceleration and therefore the external force is nearly zero.[15]

mean vertical pressure in Figure 3.5 indicates high compressive strain that increases up to 8 GPa. At ∼130 ps the Mo-layer is no longer coupled to the glass substrate in an area defined by the maximum melting radius. Simultaneously, the high heating rate with a magnitude of 10^{15} K/s and the resulting rapid thermal expansion initiates a shock wave which propagates with the speed of sound of about 5800 m/s through the entire molybdenum layer and displaces point 2 by about 10 nm towards the surrounded air. The shock wave is then reflected at the bottom side of the Mo and get back to point 1 at about 230 ps. It seems that point 1 shows no displacement for about 100 ps. As a matter of fact, the acceleration of the center of mass and thus of the entire Mo-layer was already finished after the detachment at around 130 ps and the entire layer was set in motion.

In the following, the oscillations of the moving layer are damped. The parameter of the damping, however, was chosen without affecting the initial acceleration and was not deduced from the parameter for plastic deformation. After about 1 ns points 1 and 2 have equal velocities for each fluence, which means the Mo layer is propagating nearly free at a constant speed.

The described shock wave is also shown in former simulation of ultra short laser material processing in dielectrics[149,150] and metals.[149,151,152] The evolution of the shock wave is described by a rapid decay in pressure in the order of 10^{11} Pa to 10^9 Pa within a few nanoseconds.

3.5. Ultrafast heating and melting as driving forces

As described before, the "lift-off" is initiated by ultra-fast heating and melting. The contribution of each effects to the bulging velocity of the dome can be analytically estimated. The initial velocity Δv_s that is caused by ultra-fast heating can be calculated from the change in length $l\alpha_{th}\Delta T_s$ due to the linear thermal expansion divided by the time interval for heating Δt_s:

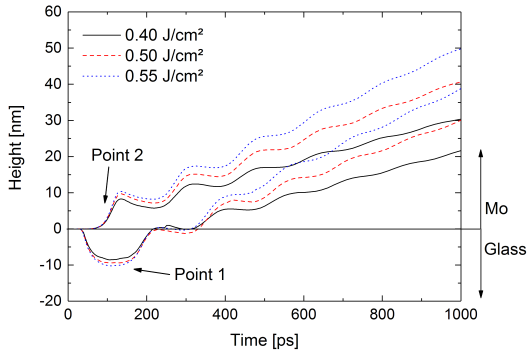

Figure 3.7.: (a) The displacement of points 1 and 2. The glass is only in contact with the molybdenum in the first 130 ps. Then the molybdenum is propagating free within the area of the melting diameter. A shockwave travels between the upper and lower boundary with the speed of sound of about 5800 m/s. This leads to a period of approx. 200 ps. We assumed a damping of the oscillation after the interaction with the substrate to model the observations and facilitate the multi-scale simulation. After about 1 ns points 1 and 2 have equal slopes for each fluence, indicating a different velocity for each fluence.

$$\Delta v_s = \frac{l_s \alpha_{th} \Delta T_s}{\Delta t_s}, \tag{3.3}$$

here, the temperature difference ΔT_s is 4,000 K, the heating time Δt_s is 20 ps, the heated layer thickness l_s is 100 nm and thermal expansion coefficient of Mo can be found in table 2.4. An expansion velocity of the layer of about 100 m/s was calculated. In addition, ultrafast melting causes a volume expansion at the phase transition from solid to a liquid, which has been determined to be 5 %[71] (Figure 2.4d). This expansion adds to the thermal expansion of the solid and accelerates the molybdenum layer further in axial direction. The velocity Δv_m due to melting can be determined by:

$$\Delta v_m = \frac{\Delta l_m \cdot 0.05}{\Delta t_m}. \tag{3.4}$$

For a melting depth Δl_m of 20 nm and a 5 % relative volume change with a melting time Δt_m of 5 ps, the resulting velocity is 200 m/s. This is twice the velocity from linear thermal expansion, caused by ultra-fast heating.

The sum of both thermal expansion effects is then 300 m/s in the direction towards the glass. The magnitude of this basic estimation is in excellent agreement with the simulated initial velocity of point 1 in the direction towards the glass, as shown in Figure 3.8. The figure shows also the velocity in point 2 which is directed away from the glass in response to the velocity in point 1. The relative velocity of point 1 in the direction towards the glass reaches an absolute maximum at the end of the acceleration which is caused by the Rayleigh damping.

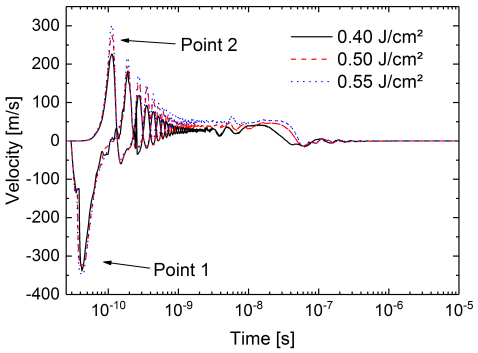

Figure 3.8.: Velocity over time in points 1 and 2 for fluence of 0.40, 0.50 and 0.55 J/cm^2. Point 1 travels with maximum speed into the glass, because of the assumed Rayleigh damping. Then points 1 and 2 oscillate inversely phased around the mean velocity

3.6. The bulging process and dome formation at low fluence

The ultrafast acceleration causes the molybdenum to bulge and results in a dome formation at low fluence, as shown in Figure 3.9. For the motion of the membrane itself, the averaged velocity in axial direction over the layer thickness is the quantity of interest. The average velocity (averaged over the vertical direction from point 1 to 2) is almost constant and directed away from the substrate during the last contact with the glass at about 130 ps until the motion slows down after 40 ns, as shown in Figure 3.10(a). The average velocity is much smaller than the peak velocities in the shock wave and is the result of the damped back-reaction of the substrate on the layer. The deviations of the average velocity from a constant value in the center are related to an oscillating motion of the moving membrane excited in several modes as well as membrane corrugation.

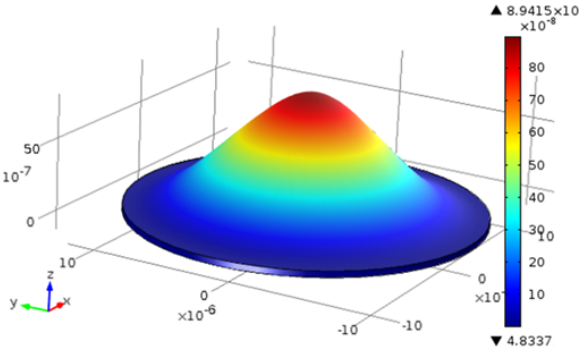

Figure 3.9.: Membrane height for 0.55 J/cm^2 during motion at 52 ns, measured from the Mo surface.

Figure 3.10(b) shows the center dome height, measured from the Mo-air interface (see Ω_2 in figure 2.21) as a function of time. The maximum height of 2.2 μm for a fluence of 0.55 J/cm^2 coincides with the time of deceleration of the membrane motion at about 40 ns. At the maximum height corrugation occurred, due to the strong initial shock-wave driven acceleration. After 400 ns, the frequency of the membrane oscillation is about 11 MHz, indicating a dynamic effect. The dome is shrinking with decreasing temperature. For a purely elastic material, the dome would be assumed to shrink to intial zero height. Thanks to the

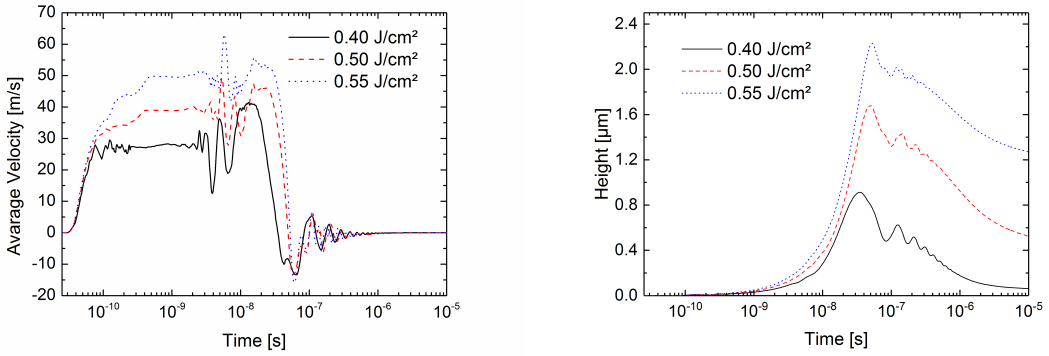

(a) (b)

Figure 3.10.: (a) Height of the dome for fluence of 0.40, 0.50 and 0.55 J/cm^2 , measured from the Mo surface. The layer expands at constant bulging velocity and starts to oscillate after the maximum is reached, due to inertial effects. At the end of the timescale the layer has an irreversible deformation, although it cools down to room temperature. This is an effect of the plastic deformation. (b) Average velocity (averaged over the vertical direction from point 1 to 2) for fluence of 0.40, 0.50 and 0.55 J/cm^2. In the first hundreds of picoseconds the layer accelerates to a constant velocity. The oscillations at around 10 ns are numerical discretization errors. The oscillation at 100 ns is observed also in our height experiments and can be interpreted as corrugation. After 1μs the mechanical motion has terminated.

plastic material in the presented model, a residual deformation was obtained, which defines the static height of the dome. As mentioned earlier in section g, the material properties of the sputtered molybdenum are not well characterized. The used plastic material model parameters have to be considered as estimates, which leads qualitatively to the observed dome height by Domke et al.[41]

The cooling of the film results in a shrinking of the layer. Hence, the thermal expansion in radial direction has a significant contribution to bulging. Assuming a circular dome geometry, the maximum static dome height h caused by thermal expansion can be estimated (see table 3.1).

The temperature is taken at the time of maximum dome height. However, this is only a static consideration without plastic deformation and dynamic effects. By comparing the dome height from the static estimation for a fluence of 0.55 J/cm^2 with the simulation result it appears that the contributes from radial thermal expansion to the bulging of the dome is only below 50 %. The remaining contribution is expected from plastic deformation and inertia overshoot.

Fluence [J/cm^2]	Δ T [K]	Maximum static Dome height h [nm]
0.40	1300	970
0.50	1490	1050
0.55	1585	1070

Table 3.1.: Estimated maximum static dome height by thermal expansion for a circular dome geometry.

3.7. Shearing from strain and threshold to ablation at high fluence

During the motion of the membrane away from the substrate stresses and strains are created in the layer. The implemented plastic deformation model causes stress relaxation with time. The strain values, however, are not reduced from plastic deformation and are a perfect parameter to identify the condition for fracture. Figure 3.11(a) and 3.11(b) presents the maximum values of radial strain over the radial position for different times with fluences of 0.40 and 0.55 J/cm^2. The maximum strain value is located at the melting radius and increases strongly with increasing fluence. It can be expected, that a critical value is exceeded for some fluence and that fracture of the layer occurs along the periphery, leading to the "lift-off" ablation with a layer fragment in form of a disk. In addition, the strain at the centre (radius of zero) also increases with increasing fluence. This could be a reasonable explanation for a crack on top of an ablated dome, as described by Heise et al.[25] (see figure 3.1).

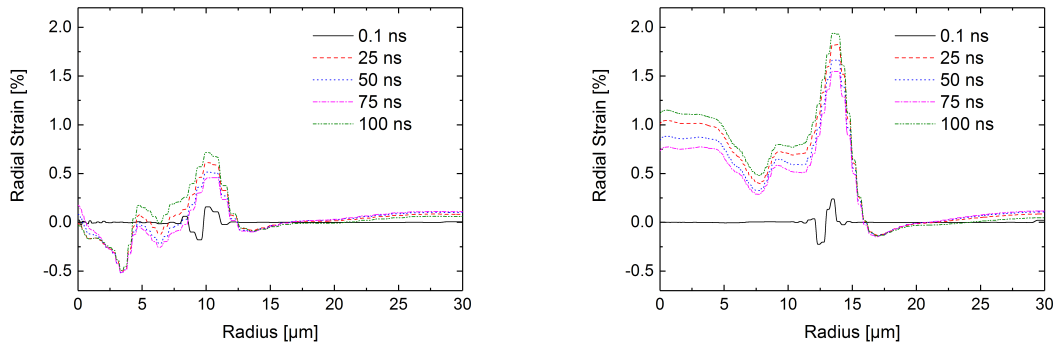

(a) (b)

Figure 3.11.: Maximum values for radial strain (a) for 0.40 J/cm2 and (b) for 0.55 J/cm2. The strain maximum appears at the edges of the confined melting radius. The strain level rises with higher fluence. Also a strain raise is visible at the centre, which can lead to a crack, as described by Heise et al.[25]

3.8. Front side irradiation

By using the material and method described before, results of a simulation for a front side ablation were obtained by using the laser pulse absorption model and thermal heat diffusion and phase change model, exclusively. A slightly modified laser wavelength of 1064 nm and a beam radius of 20 μm was applied for comparison with experimental results.[49] Figure 3.12 illustrates that the pulse was now applied from the front side. The aim of this study was to investigate the ablation efficiency in dependence on the pulse duration. For this purpose, the maximum melting and vapor volume was simulated. The applied laser peak fluences was set to 20 mJ/cm^2 while the pulse duration was varied over ranges from 5 fs to 100 ps. For the simulation of the vapor volume an elevated fluence of 4.9 J/cm^2 was needed for vapor generation of all pulse duration.

In figure 3.13(a) the comparison of the transient behavior of the electron temperature for different pulse duration is plotted. The laser intensity maximum is set to 30 ps as previously

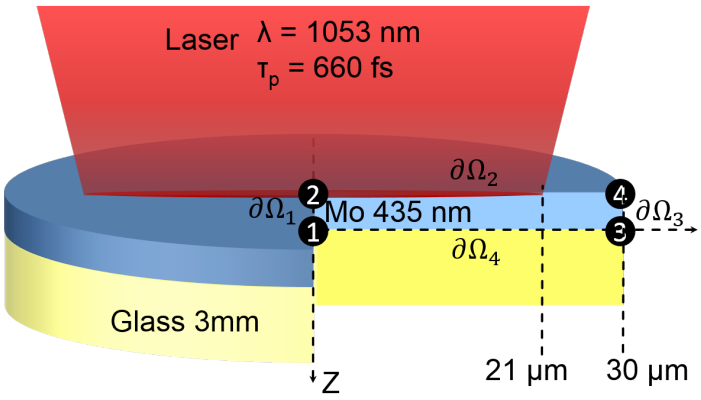

Figure 3.12.: The thin-film molybdenum layer is irradiated by a laser (wavelength 1053 nm, pulse duration 660 fs) through a transparent glass. Only the rectangular Mo-cross section is used in the axisymmetric model. Important points at the boundary of the simulation domain are numbered from 1 to 4. The maximum irradiated intensity is reached in the center at point 1. The distance from 1 to 3 is 30 μm and from 1 to 2 is 435 nm.

described in section 3.2. The highest electron temperatures of 23,000 K appears for the shortest pulse duration of 5 fs. As expected, the electron peak temperature decreases with increasing pulse duration, due to the decreasing peak intensity. A temporal shift of the maximum electron temperature for increasing pulse duration is visible.

Figure 3.13(b) shows the comparison of the lattice temperature for the different pulse duration. The absolute maximum of the lattice temperature of each pulse duration increases from 5 fs to a maximum at 10 ps and the drop then down to 100 ps. All pulse duration passes the melting temperature. In addition, the vapor temperature is slightly reached for the pulse duration of 10 ps which can be identified by a time interval with constant temperature.

Figure 3.13(c) illustrates the maximum melting volume as a function of the laser pulse duration. A maximum value of the achieved melting volume with 25 μm^3 appears at 10 ps. Besides this pulse duration the melting volume is monotonically decreasing. This observation can be explained as follows. In the case of shorter pulse duration, the electron heat capacity C_e is proportional to the electron temperature T_e according to table 2.3. Thus, for high electron temperatures more energy can be initially stored in the electron system. The initially locally narrowed strong heated volume at point 2 creates a high temperature gradient inside the Mo-layer which distributes the electron temperature very fast into the surrounded region and outside the melting area. This effect is may additionally driven by the rising of the electron conductivity k_e in the condition of high electron temperature and low lattice temperature. Thus the losses caused by electron heat diffusion are predominated. In the case of longer pulse duration the lattice temperature gradient distributes most of the thermal energy in the material such that is transferred outside the melting area.

A similar observation is shown in figure 3.13(d). Here, the vapor volume is plotted versus the pulse duration. A fluence of 4.9 J/cm^2 initiates a region with a maximum vapor volume of about 57 μm^3 between 10 to 50 ps. Due to the higher applied fluence the above described mechanism is extended to longer pulse duration. The dependence of the threshold peak fluence and thus the ablation efficiency for longer pulse duration is well known and is proportinal to the square root of the pulse duration:[153]

$$\Phi_{0,thr}(\tau_p) \sim \sqrt{\tau} \tag{3.5}$$

Summarized, the simulation results suggest that the maximum ablation efficiency for molybdenum can be achieved by a laser with a pulse duration of 10 to 50 ps.

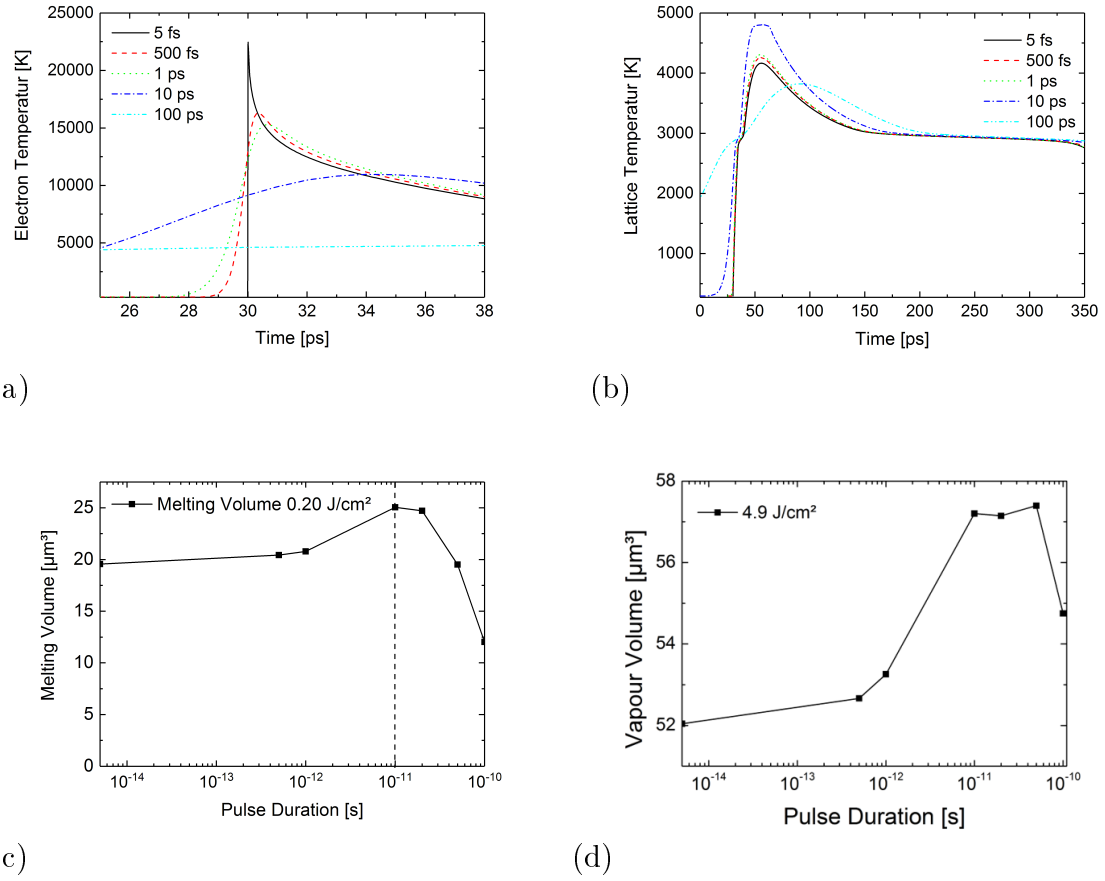

Figure 3.13.: (a) The electron temperature and (b) the lattice temperature for 5 fs to 100 ps laser pulse duration versus the time. (c) The maximum melting volume and (d) the maximum vapor volume versus the pulse duration. A logariythm x-axis is applied for bettter resolution. The laser wavelength is 1064 nm, the beam radius is 21 μm (@1/e^2) and the peak fluence is 0.20 J/cm^2; expect for the peak fluence of the vapor volume which is 4.9 J/cm^2. The maximum of the pulse is set to 30 ps. The lines are plottted as a guide to the eyes[54]

A recent study reports that indeed there is evidence for an efficient pulse duration range around 10 ps. Figure 3.14 shows data from Neuenschwander et. al.[49] The ablation threshold fluence of steel in dependence on the pulse duration which is measured after 256 pulses at the same spacial point is illustrated for each pulse duration. The experimental data are still under debate, but if the lowest threshold fluence is to be associated with the ablation efficiency a similar trend for pulse duration below 10 ps in relation to the present simulation results can be observed. It is further noted, that the front side ablation model is only a thermal model and neglect mechanical effects like shock waves and thermal expansion, which is likely to possible influence the results. This could be an explanation why the simulation

results show the maximum vapor volume up to 50 ps while the experimental results show a monotonic increase in the threshold fluence up to 50 ps. A very interesting observation can be made by comparing the the maximum melting volume from the simulation in figure 3.13(c) with the experimental results. Here, the trend of both curves are in much better agreement, which is an indication that melting plays a much more impotent role than evaporation in the mechanism for the front side ablation threshold process. This is supported by further results from literautre.[154, 155]

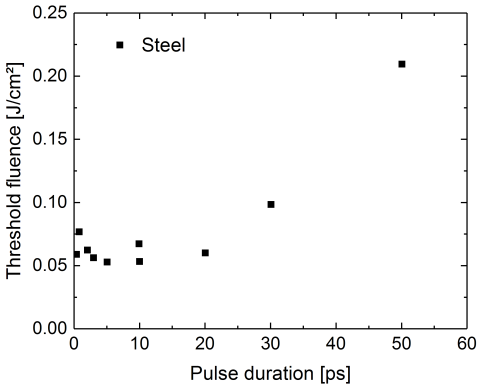

Figure 3.14.: Ablation threshold fluence of steel in dependence of the pulse duration which is measured after 256 pulses at the same spacial point on the probe surface for each measure point. (Picture and caption obtained from Neuenschwander et. al[49]).

4. Discussion

4.1. Analysis of the driving force for the initiation of the "lift-off"

Former studies show a variety of explanations for the driving forces that initiate the laser "lift-off" by confined ablation. Especially, the application of ultra-short pulse lasers suggest that ultrafast effects might also have a contribution.[37–41] Essentially four effects are considered in this simulation study:

(1) Expansion of gas under confinement

(2) Thermal expansion in axial direction driven by ultra fast heating

(3) Thermal expansion in axial direction driven by ultra fast melting during the phase transition from solid to liquid

(4) Thermal expansion of the heterogeneously heated film in radial direction

Expansion of gas under confinement is explained as the driving force for nanosecond laser ablation.[35] In the present simulation study, however, with the use of ultra-short pulses, the pressure generated by thermal expansion was 5 orders of magnitude above the pressure from gas expansion under confinement. This implies that the contribution of the gas pressure is negligible and there is a clear evidence that thermal expansion can be regarded as the driving force.

Consequently, the simulation suggests that the acceleration of the film is mainly driven by ultrafast heating and melting and not by partial evaporation and subsequent gas expansion, as assumed in the earlier analitc model[25] (see section 3.1). This implication is also supported by experimental observations of shock waves during confined laser ablation, which are initiated by ultrafast heating and melting.[156]

A shock wave is initiated by the ultra fast thermal expansion[10,41,157] which propagates from the Mo-glass interface $\partial\Omega 4$ to the Mo-air interface $\partial\Omega 2$ (Figure 3.12) and vice versa. The arose recoil pressure induces the delamination process of the Mo-film from the substrate within an area of the melting radius. During the time of the shock wave accelerated Mo-film, there is no relevant contribution from the radial thermal stress. The accelerate of the film to nearly constant velocity of about 30 to 50 m/s by a time of about 100 ps requires a value in the order of 10^{11} multiple of g. Thus, ultra fast expansion in axial direction is the predominately initial driving force. The results shows further that 1/3 of the impulse is generated by ultra fast heating and 2/3 by ultra fast melting.[158] This implies that "lift-off" is initiated although the layer is not molten completely. The simulation revealed that the maximum melting depth is only about 1/4 of the complete layer thickness (Figure 4.1).

In contrast, in case of nanosecond laser ablation, a larger volume is heated with a lower heating rate and thus a thermal expansion on a time scale 3 orders of magnitude lower occurs than in the case of ultra-short pulse ablation. The back reaction of the substrate is therefore

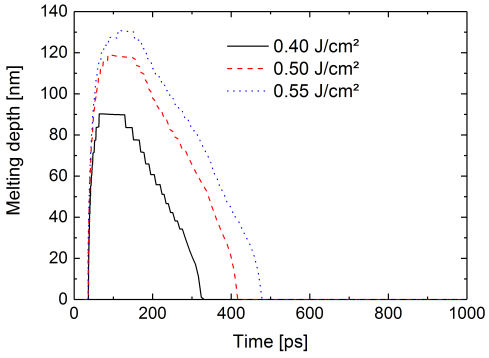

Figure 4.1.: Maximum melting depth of the Mo-layer by irradiation through the glass substrate with peak fluences of 0.40, 0.50 and 0.55 J/cm^2. The pulse duration was 660 fs and the wave length 1053 nm

too small to ablate the layer before melting and evaporation arises. Evaporation may take over the major role in confined nanosecond processing, because a larger fraction of the layer is melted and because the vapor can absorb energy directly from the laser irradiation. Thus, a high vapor pressure is may generated.

4.2. Comparison with experiment: ablation thresholds

The simulation has been conducted in accordance with the experimental parameters chosen in Ref.[41] The first validation compares the simulated ablation area with the experimental results, using the method of Liu et al.[159] This method is based on the assumption that the projection of the ablated area ($A_{abl} = \pi\ r_{alb}^2$) of a sample with a perfect threshold property is proportional to the logarithm of the irradiated peak fluence Φ_0.

$$\Phi(r,t) = \Phi_0\ e^{\frac{-2r^2}{w_0^2}} \Longleftrightarrow d^2 = 2\ w_0^2\ ln\ \frac{\Phi_{thr}}{\Phi_0} \tag{4.1}$$

where, d^2 is the square diameter of the bulged or ablated area, w_0 is the effective beam radius at $1/e^2$, Φ_{thr} is the bulging or ablation threshold, defined at a fluence level at the intersection of an extrapolated chart with the x-axis at zero diameter.

The experimental values for the bulged and ablated square diameter[41] are plotted against the logarithm of the fluence in figure 4.2 in comparison with the simulated data. It is apparent, according to the experimental values, that for peak fluences between about 0.3 and 0.5 J/cm^2 a bulging and therefore dome formation of the Mo-layer is discovered. For peak fluences above 0.5 J/cm^2 a "lift-off" ablation is observed. For the data from the simulation model, the calculated square of the melt diameter is plotted. As mentioned earlier in section c, within this diameter the Mo-layer is assumed to have lost its adhesive force with the substrate in such a way, that detachment is possible. The maximum strain values are found then at the fixed edges.

The bulged and ablated diameter data from the experiment[41] are in good agreement with the simulation data in terms of the calculated melt diameter. Both data sets exhibits a nearly perfect threshold characteristic. The main difference is a slightly systematic like deviation

which can be explained as follows. First, The melt diameter is influenced by the electron temperature model parameter, which are still under debate and not the scope of this study. Second, the temperature dependence of the light absorption coefficient has not been taken into account, due to the lack of unknown data. Indeed, the dielectric function also depends on the electron temperature.[82,83] With a possible higher optical energy coupling into the Mo-layer a larger slope of the melt diameter in the simulation results seems possible.[160] A strain value of 2 % for 0.55 J/cm^2 is exceeded in the simulation. This fluence value is the experimental ablation threshold and is set as the criteria for fracture in the simulation model.

The present study can be considered as an attempt to explain the fundamental mechanism of the confined laser ablation of thin films on transparent within the framework of ultra short laser pulse processing.

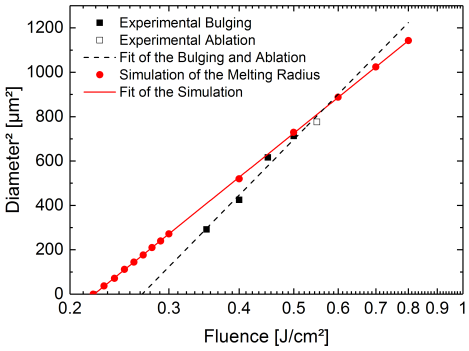

Figure 4.2.: Square diameter of the bulged or ablated area versus the laser peak fluence for the directly induced laser ablation which is plotted by the method of Liu et al.[159] The plot shows the experimental values from Domke et al.[41] (red dots) in comparison to the the present simulation study (black squares).

4.3. Comparison with experiment: pump-probe microscopy

4.3.1. Height measurement

A transient height measurement from experimental pump-probe microscopy[41] is presented (see Figure 4.3) in comparison with the simulated height, which are both measured from the center of the Mo-glass interface (Figure 3.12, point 1) to the center of the top of the dome. The overall agreement is very good. A constant velocity after 1 ns is clear visible due to the nearly straight line which indicates a direct proportionality of the height and the time with barely no acceleration. This matches with the data of the average acceleration in Figure 3.6. The experimental membrane velocity for 0.5 J/cm^2 has a value of 60 m/s and hence a slightly deviation to the 40 m/s predicted by the simulation. It can be further seen, that after the dome has exceeded its maximum height, a shrinking process appears. For fluences above 0.50 J/cm^2 the dome is ablated and no further height measurement was possible. The estimated maximum static dome height of 970 nm for 0.40 J/cm^2 (table 3.1) is consistent with the simulation and experimental results. For 0.50 and 0.60 J/cm^2 the estimation still fits to the experimental values, however the simulation height is lower, due to the imperfect plastic model parameters. The dome shrinking is correlated to the cooling and stops until

initial room temperature is achieved. Thanks to the plastic deformation model a stable dome was produced.

The comparison further shows that the bulging membrane velocity is lower for all fluences in the simulation case. The reason may be the simplification in the volume expansion model during melting, where the effect is smeared out over the melt volume instead of being localized and forming a shock front.

It seem plausible that the deviation in dome height at later times could be explained from the unknown plastic behavior of the sputtered molybdenum layer. Like all refractive vacuum coated metals, the material properties are not comparable with bulk and are probably very anisotropic. The plastic parameters have been estimated for the present model only to demonstrate qualitatively the mechanism of dome formation. A fitting for the exact reproduction of the pump probe data was not the focus of this work.

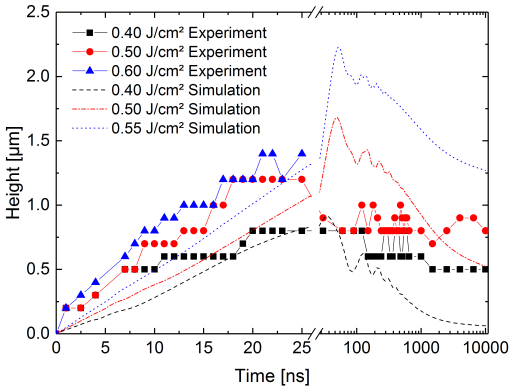

Figure 4.3.: Data of the dome height obtained from time resolved pump-probe investigations [32] compared with simulated results.

Figure 4.4(a) illustrates a dome from the FEM simulation in comparison to a confocal microscopy image from the experiment[41] with a fluence of 0.50 J/cm^2, respectively. The values for the height and the radius of the produced dome show good agreement between the simulation and the experiment.

4.3.2. Pressure waves

The evidence of pressure waves that is descibed in section 3.4 is supported by previous experimental work from Domke et al.[152] The same laser parameter of 660 fs pulse duration and 1053 nm wavelength in combination with nearly the same beam radius of 20 μm as well as the same Mo-layer thickness of 435 nm coated on a 1 mm glass substrate is used. A pump probe setup with a probe pulse of 532 nm wavelength is applied to time resolved pump-probe microscopy of the laser irradiated sample. The complete setup is descirbed in a previous work.[161]

With means of this time resolved pump-probe microscopy setup, a transient reflectivity model is introduced which considers the transient reflectivity signal R_1 of the probe beam from the Mo-glass interface during its changes of states from solid to liquid and gas. A second transient reflectivity model is included which take the reflectivity R_2 of the probe beam from a glass pressure wave into account (see figure 4.5(a)). Both transient reflectivity models are combined to calculate the overall transient reflectivity signal obtained from the interference of the two probe beams in figure 4.5(b).

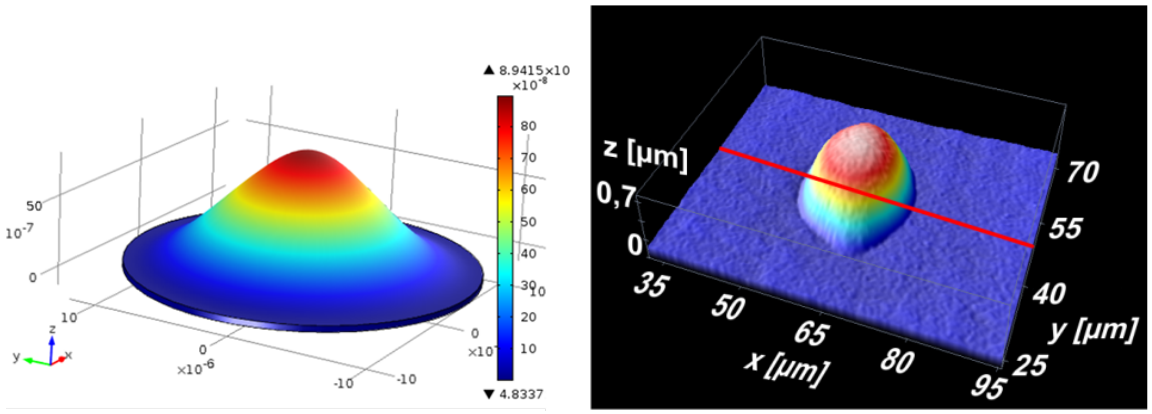

(a) (b)

Figure 4.4.: (a) Simulated dome of a glass side irradiated Mo-film with a laser pulse duration of 660 fs and a fluence of 0.50 J/cm^2,[15] (b) Confocal microscopy image of an experimental result with comparable parameters.[41]

It is assumed that the generated pressure wave is initiated in a time frame of a few picoseconds. It is further concluded by comparison of the below bulging fluence and the above bulging fluence, that the pressure wave is launched during heating and melting. In addition, pressure waves are found below the bulging threshold in the fluence range where evaporation is insufficient. These findings are in very good agreement with the present simulation results when a pressure wave towards the Mo-layer was initiated at about 5 ps during the melting process. For fluences sufficient for evaporation, no deviations in the oscillations signal in figure 4.5(b) are found in the time frame when evaporation was calculated in the present simulation model and there is no indication of a contribution of a confined gas to the film bulging.[152] Further shock-wave observation is reported in literature by the lift-off of thin-Mo-films on glass substrate irradiation with ultra short laser pulses.[156]

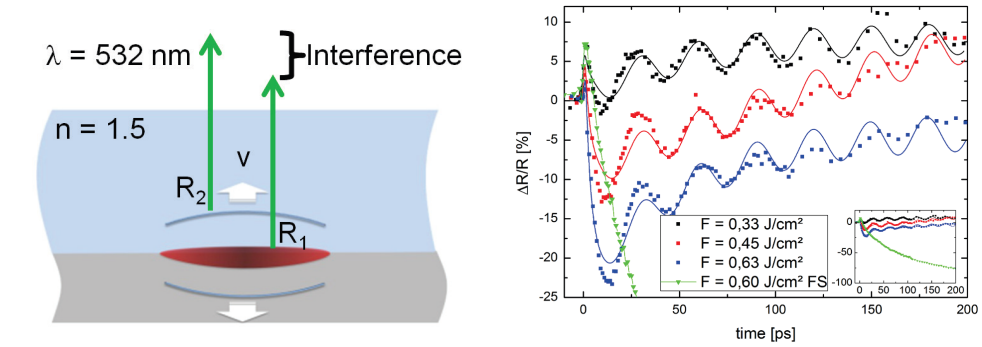

(a) (b)

Figure 4.5.: (a) The laser-induced ultrafast thermal expansion at the Mo-glass interface generates pressure waves in the transparent and in the absorbing layers. The pressure wave can be regarded as a moving interface with the reflectivity R_2 that propagates towards the probe-pulse with a velocity v. The distance of this interface determines the phase shift between the reflected wave fronts from the pressure wave (R_2) and the laser-matter interaction zone (R_1). The interference of both reflections lead to an oscillation in the time-resolved reflectivity signal. (b) Relative reflectivity from the interference of the two probe laser pulses.(Figure and caption obtain from Domke et. al.[152])

5. Conclusion

Prior works have demonstrated a suggestion for the mechanism of "lift-off" with short[34–36] and ultra short[20,37–40] laser pulses. Although, these studies have shown reliable models of "lift-off" for short pulse laser ablation, only simplified static model have been established for the case of ultra short laser pulses. In this dissertation a multiphysics and multi-time scale FEM simulation model was introduced for the description of the driving mechanisms for confined ultra short laser ablation of metal thin film on a transparent substrate by the example of a Mo-layer on a glass substrate. A "big-picture" of the whole ablation process was created by combining multiphysics with multi-time scale modeling. Within the multiphysics model, it was possible to implement the optical, thermal and mechanical physics. These different physical aspects all appear on different time scales ranging from the femtosecond to the microsecond scale and are interconnected to each other. Thanks to the additional multi-time scale approach, this led to a very powerful simulation model.

It was demonstrated that the initial driving force for ultra short pulse laser ablation of thin Mo films on glass substrate is identified as ultra fast thermal expansion in axial direction caused by ultra fast heating and melting. The further dome formation is supported by heating of the thin Mo-film in radial direction. A surprising outcome of this study is that these mechanisms are fundamentally different from those which are found by short pulse laser ablation with pulse duration in the nanosecond regime. The results were used for reliable predictions which were comparable to those of related experimental work.[41] The bulging velocity and the dome height were able to be reproduced in a qualitative manner. The model was further applied to the prediction for the mechanism of front side ablation of Mo with ultra short laser pulses.

The presented model extend those from Heise et al.[25] by investigating the vapor pressure and the thermal expansion in a transient 3d axisymmetric model to identify a variety of predominating effects that can have a contribution on the driving force. This simulation study has further motivate studies in the field of ultrashort laser ablation at spacial confined of thin films.[152,162–179,179–189] Because the laser energy is deposited ultra fast in a localized region near the interface, the Mo-layer expands thermally fast and produces a shock wave which initiates the ablation process. The expansion of the Mo-layer into the substrate produces a backward impulse and creates large enough forces and strain for film bulging and ablation. Thermal expansion of both, heating and melting, must be assumed to get the right value for the "lift-off". The gas pressure from evaporation is not sufficient to contribute to the mechanism and is also only observed during a very short time period. The insight gained in this investigation concerns the fundamental role of the backward impulse generated by the substrate. This impulse produces a sufficiently high acceleration to set the layer in motion in the opposite direction to the substrate. The effect is therefore purely mechanical and the characterization is therefore a so-called "cold ablation". In this model, the process and material parameters may be varied and investigated systematically as they are: The electronic and optic parameter of the materials, the elastic parameter of layer and substrate. The model assumptions can explain all observed phenomena and magnitudes. In such a way, the "directly induced" laser ablation process could may be improved. At the same time, the experimental validation could be improved using the discovered dependencies in the present investigation.

In the present study, a deep insight had been made possible to increase the understanding of "lift-off" with ultra short laser pulses and therefore contributes and benefits to the global understanding in the field of laser matter interaction. To the author knowledge, this is the first time that a simulation model was created which explains the dome formation with means of confined ultra short laser ablation and gave a qualitative description of its driving force. The results can deepen the understanding of ultra short laser material processing and are capable to optimize industrial processes. The used layer system is preferred used as a back-contact for copper indium gallium (di)selenide (CIGS) thin-film solar cell. The new know-how is may beneficial for the improvement of laser processes for these solar cells in terms of energy efficiency, product quality and production costs.

However, some imperfections are worth noting. Although the model was able to give a excellent qualitative description, better known material parameter are necessary for accurate quantitative results. These parameters are those for the absorption and the two-temperature model which are virtually all temperature depended. In addition, the elasto-plastic material parameters need to be derived for the thin film which may consists of anisotropies that differs from the balk ones and may depends also on the fabrication method. The introduced model is not limited to the present used materials of Mo and glass. Both, the thin film and the substrate can be substituted by any materials where the material data are well-known. For the case of non-metal thin films the absorption and two-temperature model need to be modified like it is suggested in literature.[190,191] Multi-pulse simulation could be performed too within the framework of this model, however the simulation time consumption will growth with every additional pulse. It is also concievable to add a crack analysis to focus on the shear of the layer.[192]

A. Appendix for Methodology

A.1. Appendix for the Laser pulse absorption model

A.1.1. Crul operator for the wave equation

$$\begin{aligned}
&\boldsymbol{\nabla} \times (\boldsymbol{\nabla} \times \mathbf{E}) = \boldsymbol{\nabla} (\boldsymbol{\nabla} \cdot \mathbf{E}) - \boldsymbol{\nabla}^2 \mathbf{E} = -\boldsymbol{\nabla} \times \dot{\mathbf{B}} \\
&\boldsymbol{\nabla} \times \dot{\mathbf{B}} = \tilde{\mu}\tilde{\epsilon}\ddot{\mathbf{E}} + \tilde{\mu}\sigma_{el}\dot{\mathbf{E}} \\
\Rightarrow &\boldsymbol{\nabla}^2 \mathbf{E} - \tilde{\mu}\tilde{\epsilon}\ddot{\mathbf{E}} - \tilde{\mu}\sigma_{el}\dot{\mathbf{E}} = 0
\end{aligned} \tag{A.1}$$

A.1.2. Squared hyperbolic secant

$$sech^2(x) = \frac{1}{cosh^2(x)} = \frac{4}{(e^x + e^{-x})^2} = \frac{4}{e^{2x} + e^{-2x}} = \frac{4e^{2x}}{e^{4x} + 1} \tag{A.2}$$

A.1.3. Mean laser power

The peak laser power P_0 is obtained by taking the integral of the intensity over its area:

$$\begin{aligned}
P_0 = \int_{-\infty}^{\infty} I(x,y)\, dA = \int_{-\infty}^{\infty} e^{\frac{-2(x^2+y^2)}{w_0^2}}\, dx\, dy = \frac{I_0}{2} \int_0^{2\pi} \int_0^{\infty} e^{\frac{-2(R^2)}{w_0^2}}\, R\, dR\, d\Theta \\
\rightarrow \quad P_0 = \frac{I_0\, \pi\, w_0^2}{2}.
\end{aligned} \tag{A.3}$$

The peak fluence Φ_0 is utilized by by taking the integral of the intensity over time and then substituting the peak intensity I_0 of equation A.3 with the peak laser power P_0:

$$\begin{aligned}
\Phi_0 = I_0 \int_{-\infty}^{\infty} I(t)\, dt = I_0 \int_{-\infty}^{\infty} sech^2(\frac{1.76t}{\tau})\, dt = I_0 \frac{2\tau}{1.76} = \\
\rightarrow \quad \Phi_0 = \frac{2\, P_0}{\pi\, w_0^2} \frac{2\, \tau}{1.76}
\end{aligned} \tag{A.4}$$

The peak laser power P_0 is related with the mean laser power $\bar{P}$ through the pulse duration τ_p and the laser repetition rate f_{rep}. Finally, the peak fluence Φ_0 can be expressed in terms of the mean laser power $\bar{P}$ with equation A.4.

$$\frac{P_0\, 2\, \tau_p}{1.76} = \frac{\bar{P}}{f_{rep}} \quad \rightarrow \quad P_0 = \frac{\bar{P}\, 1.76}{f_{rep}\, 2\, \tau} \quad \Rightarrow \quad \Phi_0 = \frac{2\, \bar{P}}{\pi\, \omega_0^2\, f_{rep}} \tag{A.5}$$

A.1.4. Intensity volume integral

$$-\int_{\Omega_0} (\boldsymbol{\nabla}\mathbf{v})^T \left(\boldsymbol{\nabla}\mathbf{I} + \alpha_{opt}\mathbf{I}\right)\, \mathrm{d}V_0 = \int_{\Omega_0} -\frac{\partial \mathbf{v}}{\partial R}\frac{\partial \mathbf{I}}{\partial R} - \frac{\partial \mathbf{v}}{\partial Z}\left(\frac{\partial \mathbf{I}}{\partial Z} + \alpha_{opt}\,\mathbf{I}\right)\, \mathrm{d}V_0 \tag{A.6}$$

A.2. Appendix for the Thermal heat diffusion and phase change model

A.2.1. Divergence of the temperature gradient

$$\nabla \cdot (k_l \nabla T) = \frac{1}{R}\frac{\partial}{\partial R}\left(R k_l \frac{\partial T}{\partial R}\right) + \frac{1}{R}\frac{\partial}{\partial \Theta}\left(\frac{k_l}{R}\frac{\partial T}{\partial \Theta}\right) + \frac{\partial}{\partial Z}\left(k_l \frac{\partial T}{\partial Z}\right) \tag{A.7}$$

A.2.2. Second-order identity tensor

$$\mathbf{1} = \mathbf{e}_i \mathbf{e}_j \delta_{ij} = \begin{bmatrix} 1 & 0 & 0 \\ 0 & 1 & 0 \\ 0 & 0 & 1 \end{bmatrix} \tag{A.8}$$

here, $\mathbf{e}_{i;j}$ are the two components of the second-order identity tensor.

A.3. Appendix for the Thermal expansion model

A.3.1. Deformation gradient in cylindrical coordinates

$$F = \begin{bmatrix} 1 & 0 & 0 \\ 0 & 1 & 0 \\ 0 & 0 & 1 \end{bmatrix} + \begin{bmatrix} \frac{\partial u}{\partial R} & 0 & \frac{\partial u}{\partial Z} \\ 0 & \frac{u}{R} & 0 \\ \frac{\partial w}{\partial R} & 0 & \frac{\partial w}{\partial Z} \end{bmatrix} = \begin{bmatrix} 1+\frac{\partial u}{\partial R} & 0 & \frac{\partial u}{\partial Z} \\ 0 & 1+\frac{u}{R} & 0 \\ \frac{\partial w}{\partial R} & 0 & 1+\frac{\partial w}{\partial Z} \end{bmatrix} \tag{A.9}$$

A.3.2. The Cauchy-Green deformation tensor

The right Cauchy-Green deformation tensor in cylindrical coordinates can be written as:

$$\mathbf{C} = \mathbf{F}^T\mathbf{F} = \begin{bmatrix} 1+\dfrac{\partial u}{\partial R} & 0 & \dfrac{\partial w}{\partial R} \\ 0 & 1+\dfrac{u}{R} & 0 \\ \dfrac{\partial u}{\partial Z} & 0 & 1+\dfrac{\partial w}{\partial Z} \end{bmatrix} \begin{bmatrix} 1+\dfrac{\partial u}{\partial R} & 0 & \dfrac{\partial u}{\partial Z} \\ 0 & 1+\dfrac{u}{R} & 0 \\ \dfrac{\partial w}{\partial R} & 0 & 1+\dfrac{\partial w}{\partial Z} \end{bmatrix} =$$

$$\begin{bmatrix} \left(1+\dfrac{\partial u}{\partial R}\right)^2 + \left(\dfrac{\partial w}{\partial R}\right)^2 & 0 & \left(\dfrac{\partial u}{\partial Z}\right)\left(1+\dfrac{\partial u}{\partial R}\right) + \left(\dfrac{\partial w}{\partial R}\right)\left(1+\dfrac{\partial w}{\partial Z}\right) \\ 0 & \left(1+\dfrac{u}{R}\right)^2 & 0 \\ \left(\dfrac{\partial u}{\partial Z}\right)\left(1+\dfrac{\partial u}{\partial R}\right) + \left(\dfrac{\partial w}{\partial R}\right)\left(1+\dfrac{\partial w}{\partial Z}\right) & 0 & \left(\dfrac{\partial u}{\partial Z}\right)^2 + \left(1+\dfrac{\partial w}{\partial Z}\right)^2 \end{bmatrix} \tag{A.10}$$

A.3.3. Voigt notation

In Voigt notation the symmetric second order stress tensor can be rewritten in the following simplified way:

$$\sigma = \begin{bmatrix} \sigma_{11} & \sigma_{12} & \sigma_{13} \\ \sigma_{21} & \sigma_{22} & \sigma_{23} \\ \sigma_{31} & \sigma_{32} & \sigma_{33} \end{bmatrix} = \begin{bmatrix} \sigma_{11} & \sigma_{12} & \sigma_{13} \\ \cdot & \sigma_{22} & \sigma_{23} \\ \cdot & \cdot & \sigma_{33} \end{bmatrix} = \begin{bmatrix} \sigma_{11} \\ \sigma_{22} \\ \sigma_{33} \\ \sigma_{23} \\ \sigma_{12} \\ \sigma_{13} \end{bmatrix} \tag{A.11}$$

A.3.4. Divergence operator

$$div\ \mathbf{A} = \boldsymbol{\nabla} \cdot\ \mathbf{A} = \begin{bmatrix} \dfrac{A_{11}}{X_1} & \dfrac{A_{21}}{X_2} & \dfrac{A_{31}}{X_3} \\ \dfrac{A_{12}}{X_1} & \dfrac{A_{22}}{X_2} & \dfrac{A_{32}}{X_3} \\ \dfrac{A_{13}}{X_1} & \dfrac{A_{23}}{X_2} & \dfrac{A_{33}}{X_3} \end{bmatrix} \tag{A.12}$$

A.3.5. Double dot product

$$\begin{aligned} \mathbf{A} : \mathbf{B} = \sum_j \sum_i A_{ij} B_{ij} = \\ A_{11}B_{11} + A_{12}B_{21} + A_{13}B_{31} + \\ A_{21}B_{12} + A_{22}B_{22} + A_{23}B_{32} + \\ A_{31}B_{13} + A_{32}B_{23} + A_{33}B_{33} \end{aligned} \tag{A.13}$$

A.3.6. Fourth-order identity tensor

$$\mathbf{I} = \mathbf{e}_i \mathbf{e}_j \delta_{ij} \delta_{kl} \mathbf{e}_k \mathbf{e}_l = \begin{bmatrix} 1 & 0 & 0 & 0 & 0 & 0 & 0 & 0 & 0 \\ 0 & 1 & 0 & 0 & 0 & 0 & 0 & 0 & 0 \\ 0 & 0 & 1 & 0 & 0 & 0 & 0 & 0 & 0 \\ 0 & 0 & 0 & 0 & 1 & 0 & 0 & 0 & 0 \\ 0 & 0 & 0 & 1 & 0 & 0 & 0 & 0 & 0 \\ 0 & 0 & 0 & 0 & 0 & 0 & 1 & 0 & 0 \\ 0 & 0 & 0 & 0 & 0 & 1 & 0 & 0 & 0 \\ 0 & 0 & 0 & 0 & 0 & 0 & 0 & 1 & 1 \\ 0 & 0 & 0 & 0 & 0 & 0 & 0 & 1 & 1 \end{bmatrix} \tag{A.14}$$

here, $\mathbf{e}_{i;j;k;l}$ are the four components of the fourth-order identity tensor.

A.3.7. Tensor product

$$\mathbf{A} \otimes \mathbf{B} = \begin{bmatrix} A_{11}B_{11} & A_{11}B_{12} & A_{11}B_{13} & A_{12}B_{11} & A_{12}B_{12} & A_{12}B_{13} & A_{13}B_{11} & A_{13}B_{12} & A_{13}B_{13} \\ A_{11}B_{21} & A_{11}B_{22} & A_{11}B_{23} & A_{12}B_{21} & A_{12}B_{22} & A_{12}B_{23} & A_{13}B_{21} & A_{13}B_{22} & A_{13}B_{23} \\ A_{11}B_{31} & A_{11}B_{32} & A_{11}B_{33} & A_{12}B_{31} & A_{12}B_{32} & A_{12}B_{33} & A_{13}B_{31} & A_{13}B_{32} & A_{13}B_{33} \\ A_{21}B_{11} & A_{21}B_{12} & A_{21}B_{13} & A_{22}B_{11} & A_{22}B_{12} & A_{22}B_{13} & A_{23}B_{11} & A_{23}B_{12} & A_{23}B_{13} \\ A_{21}B_{21} & A_{21}B_{22} & A_{21}B_{23} & A_{22}B_{21} & A_{22}B_{22} & A_{22}B_{23} & A_{23}B_{21} & A_{23}B_{22} & A_{23}B_{23} \\ A_{21}B_{31} & A_{21}B_{32} & A_{21}B_{33} & A_{22}B_{31} & A_{22}B_{32} & A_{22}B_{33} & A_{23}B_{31} & A_{23}B_{32} & A_{23}B_{33} \\ A_{31}B_{11} & A_{31}B_{12} & A_{31}B_{13} & A_{32}B_{11} & A_{32}B_{12} & A_{32}B_{13} & A_{33}B_{11} & A_{33}B_{12} & A_{33}B_{13} \\ A_{31}B_{21} & A_{31}B_{22} & A_{31}B_{23} & A_{32}B_{21} & A_{32}B_{22} & A_{32}B_{23} & A_{33}B_{21} & A_{33}B_{22} & A_{33}B_{23} \\ A_{31}B_{31} & A_{31}B_{32} & A_{31}B_{33} & A_{32}B_{31} & A_{32}B_{32} & A_{32}B_{33} & A_{33}B_{31} & A_{33}B_{32} & A_{33}B_{33} \end{bmatrix} \tag{A.15}$$

A.3.8. Partial integration

Two differentiable functions $f(x)$ and $g(x)$ can be partially integrated within the interval a and b by:

$$\int_a^b f(x)' \, g(x) = [f(x) \; g(x)] \Big|_a^b - \int_a^b f(x) \; g(x)' \tag{A.16}$$

here, $f(x)'$ and $g(x)'$ is the first derivative of $f(x)$ and $g(x)$, respectively.

A.4. Appendix for the Space and time discretization

A.4.1. Integral tranformation

The integral of a function $g(x)$ within the interval a and b can be transformed into the normalized interval -1 and 1 with a function $f(t)$ in the following way:

$$\int_a^b g(x)dx = \int_{-1}^{1} f(t)dt \qquad \text{with} \quad t \in [-1,1] -> x = a + \frac{b-a}{2}(t+1) \in [a,b]$$
$$\Rightarrow \int_a^b g(x)dx = \frac{b-a}{2} \int_{-1}^{1} g\left(a + \frac{b-a}{2}(t+1)\right) dt \tag{A.17}$$

A.4.2. Inentsity discretization

The intensity stiffness matrix equation 2.191a mapped to the natural coordinate system can be expressed as:

$$K_{\mathbf{I};ij;e} = \int_{\Omega_{0;e}} \left[-\left(\mathbf{J}^{-1}_{11;e}\frac{\partial N_i(\xi,\eta)}{\partial \xi} + \mathbf{J}^{-1}_{12;e}\frac{\partial N_i(\xi,\eta)}{\partial \eta}\right)\left(\mathbf{J}^{-1}_{11;e}\frac{\partial N_j(\xi,\eta)}{\partial \xi} + \mathbf{J}^{-1}_{12;e}\frac{\partial N_j(\xi,\eta)}{\partial \eta}\right) \right.$$
$$\left. -\left(\mathbf{J}^{-1}_{21;e}\frac{\partial N_i(\xi,\eta)}{\partial \xi} + \mathbf{J}^{-1}_{22;e}\frac{\partial N_i(\xi,\eta)}{\partial \eta}\right)\left(\mathbf{J}^{-1}_{21;e}\frac{\partial N_j(\xi,\eta)}{\partial \xi} + \mathbf{J}^{-1}_{22;e}\frac{\partial N_j(\xi,\eta)}{\partial \eta} + \alpha N_j\right)\right]$$
$$2\,\pi\, R(\xi,\eta)\big|J\big|\,\mathrm{d}\xi\,\mathrm{d}\eta \tag{A.18}$$

Bibliography

[1] B. N. Chichkov, C. Momma, S. Nolte, F. von Alvensleben, and A. Tuennermann, "Femtosecond, picosecond and nanosecond laser ablation of solids," *Applied Physics A Materials Science & Processing*, vol. 63, no. 2, pp. 109–115, 1997.

[2] X. Liu, D. Du, and G. Mourou, "Laser ablation and micromachining with ultrashort laser pulses," *IEEE Journal of Quantum Electronics*, vol. 33, pp. 1706–1716, Oct 1997.

[3] C. Momma, S. Nolte, B. N. Chichkov, F. v. Alvensleben, and A. Tünnermann, "Precise laser ablation with ultrashort pulses," *Applied Surface Science*, vol. 109-110, pp. 15 – 19, 1997.

[4] S. Nolte, C. Momma, H. Jacobs, A. Tünnermann, B. N. Chichkov, B. Wellegehausen, and H. Welling, "Ablation of metals by ultrashort laser pulses," *J. Opt. Soc. Am. B*, vol. 14, pp. 2716–2722, Oct 1997.

[5] K. Sokolowski-Tinten, J. Bialkowski, A. Cavalleri, Von Der Linde, D., A. Oparin, J. Meyer-Ter-Vehn, and S. I. Anisimov, "Transient states of matter during short pulse laser ablation," *Physical Review Letters*, vol. 81, no. 1, pp. 224–227, 1998.

[6] Von Der Linde, D. and K. Sokolowski-Tinten, "Physical mechanisms of short-pulse laser ablation," *Applied Surface Science*, vol. 154, pp. 1–10, 2000.

[7] J. Bonse, S. Baudach, J. Krüger, W. Kautek, and M. Lenzner, "Femtosecond laser ablation of silicon–modification thresholds and morphology," *Applied Physics A Materials Science & Processing*, vol. 74, no. 1, pp. 19–25, 2002.

[8] E. G. Gamaly, A. V. Rode, B. Luther-Davies, and V. T. Tikhonchuk, "Ablation of solids by femtosecond lasers: Ablation mechanism and ablation thresholds for metals and dielectrics," *Physics of Plasmas*, vol. 9, no. 3, pp. 949–957, 2002.

[9] A. Vogel and V. Venugopalan, "Mechanisms of pulsed laser ablation of biological tissues," *Chemical Physics*, vol. 103, no. 2, pp. 577–644, 2003.

[10] E. G. Gamaly, "The physics of ultra-short laser interaction with solids at non-relativistic intensities," *Physics Reports*, vol. 508, no. 4-5, pp. 91–243, 2011.

[11] S. Zoppel, H. Huber, and G. Reider, "Selective ablation of thin mo and tco films with femtosecond laser pulses for structuring thin film solar cells," *Applied Physics A Materials Science & Processing*, vol. 89, no. 1, pp. 161–163, 2007.

[12] A. D. Compaan, I. Matulionis, and S. Nakade, "Laser scribing of polycrystalline thin films," *Optics and Lasers in Engineering*, vol. 34, no. 1, pp. 15–45, 2000.

[13] J. Hermann, M. Benfarah, G. Coustillier, S. Bruneau, E. Axente, J.-F. Guillemoles, M. Sentis, P. Alloncle, and T. Itina, "Selective ablation of thin films with short and ultrashort laser pulses," *Applied Surface Science*, vol. 252, no. 13, pp. 4814–4818, 2006.

[14] G. Heise, J. Konrad, S. Sarrach, J. Sotrop, H. P. Huber, A. Heisterkamp, J. Neev, and S. Nolte, "Directly induced ablation of metal thin films by ultrashort laser pulses</title>," *Proceedings of SPIE - The International Society for Optical Engineering*, vol. 7925, pp. 792511–792511–8, 2011.

[15] J. Sotrop, A. Kersch, M. Domke, G. Heise, and H. P. Huber, "Numerical simulation of ultrafast expansion as the driving mechanism for confined laser ablation with ultrashort laser pulses," *Applied Physics A Materials Science & Processing*, vol. 113, no. 2, pp. 397–411, 2013.

[16] H. P. Huber, M. Englmaier, C. Hellwig, A. Heiss, T. Kuznicki, M. Kemnitzer, H. Vogt, R. Brenning, and J. Palm, "High speed structuring of cis thin-film solar cells with picosecond laser ablation," in *Commercial and Biomedical Applications of Ultrafast Lasers IX*, vol. 7203, p. 72030R, International Society for Optics and Photonics, 2009.

[17] H. P. Huber, M. Englmaier, C. Hellwig, G. Heise, A. Heiss, M. Kemnitzer, T. Kuznicki, R. Brenning, H. Vogt, and J. Palm, "Structuring of cis thin-film solar cells by ultrafast laser pulses with industrial relevant process speed," *Proc. of SPIE*, vol. post deadline papers, pp. 1–6, 2009.

[18] G. Heise, C. Hellwig, T. Kuznicki, S. Sarrach, C. Menhard, A. Heiss, H. Vogt, J. Palm, and H. P. Huber, "Monolithic interconnection of cigsse solar cells by picosecond laser structuring," *Proc. of SPIE*, vol. 7585, pp. 0U1,0U12, 2010.

[19] H. Vogt, A. Heiss, J. Palm, F. Karg, H. P. Huber, and G. Heise, "All laser patterning serial interconnection for highly efficient cigsse modules," *21th EUPVSEC*, vol. 3DV.2.9, pp. 2947–2950, 2011.

[20] G. Heise, A. Heiss, C. Hellwig, T. Kuznicki, H. Vogt, J. Palm, and H. P. Huber, "Optimization of picosecond laser structuring for the monolithic serial interconnection of cis solar cells," *Progress in Photovoltaics: Research and Applications*, vol. 21, pp. 681–692, 2012.

[21] G. Heise, M. Dickmann, J. Konrad, I. Richter, S. Sarrach, A. Heiss, H. Vogt, and H. P. Huber, "Application of induced laser ablation with ultra short pulse lasers for high speed thin film solar cell processing," *ICALEO 2006 Congress Proceedings*, vol. 103, pp. 1199–1205, 2012.

[22] D. Bartl, A. Michalowski, M. Hafner, A. Letsch, S. Nolte, and A. Tünnermann, "Time-resolved study of back side ablated molybdenum thin films by ultrashort laser pulses," *Applied Physics A Materials Science & Processing*, vol. 110, no. 1, pp. 227–233, 2013.

[23] W. S. Wong, T. Sands, N. W. Cheung, M. Kneissl, D. P. Bour, P. Mei, L. T. Romano, and N. M. Johnson, "Inxga1-xn light emitting diodes on si substrates fabricated by pd-in metal bonding and laser lift-off," *Applied Physics Letters*, vol. 77, no. 18, pp. 2822–2824, 2000.

[24] G. Heise, M. Dickmann, M. Domke, A. Heiss, T. Kuznicki, J. Palm, I. Richter, H. Vogt, and H. P. Huber, "Investigation of the ablation of zinc oxide thin films on copper–indium-selenide layers by ps laser pulses," *Applied Physics A Materials Science & Processing*, vol. 104, pp. 387–393, Jul 2011.

[25] G. Heise, M. Domke, J. Konrad, S. Sarrach, J. Sotrop, and H. P. Huber, "Laser lift-off initiated by direct induced ablation of different metal thin films with ultra-short laser pulses," *Journal of Physics D: Applied Physics*, vol. 45, p. 315303, jul 2012.

[26] J. Bohandy, B. F. Kim, F. J. Adrian, and A. N. Jette, "Metal deposition at 532 nm using a laser transfer technique," *Journal of Applied Physics*, vol. 63, no. 4, pp. 1158–1162, 1988.

[27] V. Schultze and M. Wagner, "Laser-induced forward transfer of aluminium," *Applied Surface Science*, vol. 52, no. 4, pp. 303–309, 1991.

[28] T. V. Kononenko, P. Alloncle, V. I. Konov, and M. Sentis, "Laser transfer of diamond nanopowder induced by metal film blistering," *Applied Physics A Materials Science & Processing*, vol. 94, no. 3, pp. 531–536, 2009.

[29] V. Menezes, K. Takayama, T. Ohki, and J. Gopalan, "Laser-ablation-assisted microparticle acceleration for drug delivery," *Applied Physics Letters*, vol. 87, no. 16, pp. 1–3, 2005.

[30] G. Heise, D. Trappendreher, F. Ilchmann, R. S. Weiss, B. Wolf, and H. P. Huber, "Rapid prototyping of biocompatible sensor chips by picoseconds laser structuring of a platinum/ tantalum pentoxide thin film layer system," *Proc. of SPIE*, vol. 8247, p. 82470X, 2012.

[31] S. Hermann, N. P. Harder, R. Brendel, D. Herzog, and H. Haferkamp, "Picosecond laser ablation of sio2 layers on silicon substrates," *Applied Physics A Materials Science & Processing*, vol. 99, no. 1, pp. 151–158, 2010.

[32] P. Engelhart, N. P. Harder, R. Grischke, A. Merkle, R. Meyer, and R. Brendel, "Laser structuring for back junction silicon solar cells," *Progress in Photovoltaics: Research and Applications*, vol. 15, no. 3, pp. 237–243, 2007.

[33] S. Rapp, M. Domke, M. Schmidt, and H. P. Huber, "Physical mechanisms during fs laser ablation of thin sio2 films," *Physics Procedia*, vol. 41, pp. 734–740, 2013.

[34] R. Fabbro, J. Fournier, P. Ballard, D. Devaux, and J. Virmont, "Physical study of laser-produced plasma in confined geometry," *Journal of Applied Physics*, vol. 68, no. 2, pp. 775–784, 1990.

[35] F. J. Adrian, J. Bohandy, B. F. Kim, A. N. Jette, and P. Thompson, "A study of the mechanism of metal deposition by the laser-induced forward transfer process," *Journal of Vacuum Science & Technology B: Microelectronics and Nanometer Structures*, vol. 5, no. 5, pp. 1490–1494, 1987.

[36] N. T. Kattamis, M. S. Brown, and C. B. Arnold, "Finite element analysis of blister formation in laser-induced forward transfer," *Journal of Materials Research*, vol. 26, no. 18, pp. 2438–2449, 2011.

[37] T. E. Itina, J. Hermann, P. Delaporte, and M. Sentis, "Modeling of metal ablation induced by ultrashort laser pulses," *Thin Solid Films*, vol. 453-454, pp. 513–517, 2004.

[38] D. Ivanov, B. Rethfeld, G. O'Connor, T. Glynn, A. Volkov, and L. Zhigilei, "The mechanism of nanobump formation in femtosecond pulse laser nanostructuring of thin metal films," *Applied Physics A Materials Science & Processing*, vol. 92, no. 4, pp. 791–796, 2008.

[39] M. V. Shugaev and N. M. Bulgakova, "Thermodynamic and stress analysis of laser-induced forward transfer of metals," *Applied Physics A Materials Science & Processing*, vol. 101, pp. 103–109, 2010.

[40] I. Zergioti, D. G. Papazoglou, A. Karaiskou, C. Fotakis, E. Gamaly, and A. Rode, "A comparative schlieren imaging study between ns and sub-ps laser forward transfer of cr," *Applied Surface Science*, vol. 208-209, no. 1, pp. 177–180, 2003.

[41] M. Domke, S. Rapp, M. Schmidt, and H. P. Huber, "Ultra-fast movies of thin-film laser ablation," *Applied Physics A Materials Science & Processing*, vol. 109, no. 2, pp. 409–420, 2012.

[42] M. Domke, S. Rapp, M. Schmidt, and H. Huber, "Ultrafast pump-probe microscopy with high temporal dynamic range," *Optics Express*, vol. 20, pp. 10330–10338, 2012.

[43] M. Domke, S. Rapp, and H. Huber, "Ultra-fast movies resolve ultra-short pulse laser ablation and bump formation on thin molybdenum films," *Physics Procedia*, vol. 39, no. 0, pp. 717–725, 2012.

[44] M. Domke, S. Rapp, G. Heise, and H. P. Huber, "Time and space resolved microscopy of induced ablation with ultra-short laser pulses," *Proc. of SPIE*, vol. 8243, p. 824308, 2012.

[45] A. P. Alloncle, R. Bouffaron, J. Hermann, and M. Sentis, "Experimental study of front and back ablation of metal thin film using ultrashort laser pulses," *Proc. of SPIE*, vol. 6261, 2006.

[46] S. Beyer, V. Tornari, and D. Gornicki, "Comparison of laser induced front- and rear side ablation," *Proc. of SPIE*, vol. 5063, pp. 202–207, 2003.

[47] Q. Bian, X. Yu, B. Zhao, Z. Chang, and S. Lei, "Femtosecond laser patterning of mo thin film on flexible substrate for cigs solar cells," *ICALEO*, pp. 869–874, 2011.

[48] S. Preuss, A. Demchuk, and M. Stuke, "Sub-picosecond uv laser ablation of metals," *Applied Physics A Materials Science & Processing*, vol. 61, no. 1, pp. 33–37, 1995.

[49] B. Neuenschwander, B. Jaeggi, M. Schmid, V. Rouffiange, and P.-E. Martin, "Optimization of the volume ablation rate for metals at different laser pulse-durations from ps to fs," *Proc. of SPIE*, vol. 8243, p. 824307, 2012.

[50] A. Einstein, "Zur quantentheorie der strahlung," *Physikalische Zeitschrift*, vol. 18, pp. 121–128, 1917.

[51] T. H. Maiman, "Stimulated Optical Radiation in Ruby," *Nature*, vol. 187, pp. 493–494, Aug. 1960.

[52] A. L. Schawlow and C. H. Townes, "Infrared and optical masers," *Physical Review*, vol. 112, pp. 1940–1949, Dec 1958.

[53] C. Rulliere *et al.*, *Femtosecond laser pulses.* Springer, 2005.

[54] J. Sotrop, M. Domke, A. Kersch, and H. P. Huber, "Simulation of the melting volume in thin molybdenum films as a function of the laser pulse duration," *Physics Procedia*, vol. 41, pp. 520–523, 2013.

[55] R. D. Lide, *CRC handbook of chemistry and physics: A ready-reference book of chemical and physical data*. Boca Raton: CRC Press, 84th ed. ed., 2003.

[56] J. Colvin, A. Shestakov, J. Stölken, and R. Vignes, "The role of radiation transport in the thermal response of semitransparent materials to localized laser heating," *Journal of Applied Physics*, vol. 109, no. 5, p. 053506, 2011.

[57] M. Rubin, "Optical properties of soda lime silica glasses," *Solar Energy Materials*, vol. 12, no. 4, pp. 275 – 288, 1985.

[58] M. Domke, *Hocheffiziente Dünnschichtablation mit ultrakurzen Laserpulsen: Transiente Untersuchung der physikalischen Mechanismen der eingeschlossenen Laserablation*. Dissertation, 2014.

[59] S. K. Sundaram and E. Mazur, "Inducing and probing non-thermal transitions in semiconductors using femtosecond laser pulses," *Nature Materials*, vol. 1, no. 4, pp. 217–224, 2002.

[60] M. Domke, S. Rapp, G. Heise, and H. P. Huber, "Ultrafast movies of thin metal film ablation with ultra-short laser pulses," *International Congress on Applications of Lasers & Electro-Optics*, vol. 2012, no. 1, pp. 866–870, 2012.

[61] J. Byskov-Nielsen, J.-M. Savolainen, M. S. Christensen, and P. Balling, "Ultra-short pulse laser ablation of copper, silver and tungsten: experimental data and two-temperature model simulations," *Applied Physics A Materials Science & Processing*, vol. 103, pp. 447–453, May 2011.

[62] M. Colina, C. Molpeceres, M. Morales, F. Allens-Perkins, G. Guadaño, and J. L. Ocaña, "Laser ablation modelling of aluminium, silver and crystalline silicon for applications in photovoltaic technologies," *Surface Engineering*, vol. 27, no. 6, pp. 414–423, 2011.

[63] M. Fox and G. F. Bertsch, *Optical Properties of Solids*, vol. 70. 2002.

[64] S. I. Anisimov, B. L. Kapeliovich, and T. L. Perelman, "Electron emission from metal surfaces exposed to ultrashort laser pulses," *Zhurnal Eksperimentalnoi i Teoreticheskoi Fiziki*, vol. 66, pp. 776–781, Aug. 1974.

[65] J. G. Fujimoto, J. M. Liu, E. P. Ippen, and N. Bloembergen, "Femtosecond laser interaction with metallic tungsten and nonequilibrium electron and lattice temperatures," *Physical Review Letters*, vol. 53, no. 19, pp. 1837–1840, 1984.

[66] B. Rethfeld, A. Kaiser, M. Vicanek, and G. Simon, "Ultrafast dynamics of nonequilibrium electrons in metals under femtosecond laser irradiation," *Physical Review B - Condensed Matter and Materials Physics*, vol. 65, no. 21, 2002.

[67] M. M. Kirillova, L. V. Nomerovannaya, and M. M. Noskov, "Optical Properties of Molybdenum Single Crystals," *Soviet Journal of Experimental and Theoretical Physics*, vol. 33, p. 1210, 1971.

[68] B. Rethfeld, K. Sokolowski-Tinten, Von Der Linde, D., and S. Anisimov, "Ultrafast thermal melting of laser-excited solids by homogeneous nucleation," *Physical Review B - Condensed Matter and Materials Physics*, vol. 65, no. 9, 2002.

[69] P. Lorazo, L. Lewis, and M. Meunier, "Short-pulse laser ablation of solids: From phase explosion to fragmentation," *Physical Review Letters*, vol. 91, no. 22, 2003.

[70] P. Lorazo, L. Lewis, and M. Meunier, "Thermodynamic pathways to melting, ablation, and solidification in absorbing solids under pulsed laser irradiation," *Physical Review B - Condensed Matter and Materials Physics*, vol. 73, no. 13, 2006.

[71] Hixson R. S. and Winkler M. A., "Thermophysical properties of molybdenum and rhenium," *International Journal of Thermophysics*, vol. Vol. 13, No. 3, 1992.

[72] É. Clapeyron, "Mémoire sur la puissance motrice de la chaleur," *Journal de l'École polytechnique*, vol. 14, pp. 153–190, 1834.

[73] R. Clausius, "Ueber die bewegende kraft der wärme und die gesetze, welche sich daraus für die wärmelehre selbst ableiten lassen," *Annalen der Physik*, vol. 155, no. 4, pp. 500–524, 1850.

[74] S.-S. Wellershoff, J. Hohlfeld, J. Güdde, and E. Matthias, "The role of electron-phonon coupling in femtosecond laser damage of metals," *Applied Physics A Materials Science & Processing*, vol. 69, no. S1, pp. 99–107, 1999.

[75] M. Born and E. Wolf, *Principles of optics: electromagnetic theory of propagation, interference and diffraction of light*. Elsevier, 2013.

[76] C. J. Powell, "Analysis of optical- and inelastic-electron-scattering data. parametric calculations∗†," *Journal of the Optical Society of America*, vol. 59, pp. 738–743, Jun 1969.

[77] M. A. Ordal, R. J. Bell, R. W. Alexander, L. A. Newquist, and M. R. Querry, "Optical properties of Al, Fe, Ti, Ta, W, and Mo at submillimeter wavelengths," *Applied Optics*, vol. 27, pp. 1203–1209, Mar 1988.

[78] R. Loudon, "The propagation of electromagnetic energy through an absorbing dielectric," *Journal of Physics A: General Physics*, vol. 3, no. 3, p. 233, 1970.

[79] A. Cavalleri, C. Tóth, C. W. Siders, J. Squier, F. Ráksi, P. Forget, and J. Kieffer, "Femtosecond structural dynamics in vo 2 during an ultrafast solid-solid phase transition," *Physical review letters*, vol. 87, no. 23, p. 237401, 2001.

[80] K. Sokolowski-Tinten, J. Bialkowski, and D. von der Linde, "Ultrafast laser-induced order-disorder transitions in semiconductors," *Physical Review B*, vol. 51, no. 20, p. 14186, 1995.

[81] O. S. Heavens, "Optical properties of thin films," *Reports on Progress in Physics*, vol. 23, pp. 1–65, jan 1960.

[82] Y. Ren, J. K. Chen, and Y. Zhang, "Optical properties and thermal response of copper films induced by ultrashort-pulsed lasers," *Journal of Applied Physics*, vol. 110, no. 11, p. 113102, 2011.

[83] Y. Ren, J. K. Chen, Y. Zhang, and J. Huang, "Ultrashort laser pulse energy deposition in metal films with phase changes," *Applied Physics Letters*, vol. 98, no. 19, p. 191105, 2011.

[84] O. C. Zienkiewicz, R. L. Taylor, O. C. Zienkiewicz, and R. L. Taylor, *The finite element method*, vol. 3. McGraw-hill London, 1977.

[85] J. Hohlfeld, S. S. Wellershoff, J. Güdde, U. Conrad, V. Jähnke, and E. Matthias, "Electron and lattice dynamics following optical excitation of metals," *Chemical Physics*, vol. 251, no. 1-3, pp. 237–258, 2000.

[86] P. B. Corkum, F. Brunel, N. K. Sherman, and T. Srinivasan-Rao, "Thermal response of metals to ultrashort-pulse laser excitation," *Physical Review Letters*, vol. 61, pp. 2886–2889, Dec 1988.

[87] J. Güdde, J. Hohlfeld, J. Müller, and E. Matthias, "Damage threshold dependence on electron-phonon coupling in au and ni films," *Applied Surface Science*, vol. 127, pp. 40–45, 1998.

[88] J. K. Chen, J. E. Beraun, L. E. Grimes, and D. Y. Tzou, "Modeling of femtosecond laser-induced non-equilibrium deformation in metal films," *International Journal of Solids and Structures*, vol. 39, no. 12, pp. 3199–3216, 2002.

[89] J. K. Chen, D. Y. Tzou, and J. E. Beraun, "A semiclassical two-temperature model for ultrafast laser heating," *International Journal of Heat and Mass Transfer*, vol. 49, no. 1-2, pp. 307–316, 2006.

[90] B. H. Christensen, K. Vestentoft, and P. Balling, "Short-pulse ablation rates and the two-temperature model," *Applied Surface Science*, vol. 253, no. 15, pp. 6347–6352, 2007.

[91] J. Chen and J. Beraun, "Numerical study of ultrashort laser pulse interactions with metal films," *Numerical Heat Transfer: Part A: Applications*, vol. 40, no. 1, pp. 1–20, 2001.

[92] A. Kanavin, I. Smetanin, V. Isakov, Y. V. Afanasiev, B. Chichkov, B. Wellegehausen, S. Nolte, C. Momma, and A. Tünnermann, "Heat transport in metals irradiated by ultrashort laser pulses," *Physical Review B*, vol. 57, no. 23, p. 14698, 1998.

[93] S. Wang, Y. Ren, C. Cheng, J. Chen, and D. Tzou, "Micromachining of copper by femtosecond laser pulses," *Applied Surface Science*, vol. 265, pp. 302–308, 2013.

[94] M. Kaganov, E. Lifshitz, and L. Tanatarov, "Relaxation between electrons and the crystalline lattice," *Journal of Experimental and Theoretical Physics*, vol. 4, pp. 173–178, 1957.

[95] M. Kaganov, I. Lifshits, and L. Tanatarov, "Teoriya radiatsionnykh izmenenii v metallakh," *Atom. Energ*, vol. 6, p. 391, 1959.

[96] V. Ginzburg and V. Shabanskii, "Kineticheskaya temperatura elektronov v metallakh i anomalnaya elektronnaya emissiya," *Doklady Akademii Nauk SSSR*, vol. 100, no. 3, pp. 445–448, 1955.

[97] A. Ibrahimbegović, *Nonlinear solid mechanics: Theoretical formulations and finite element solution methods*, vol. 160 of *Solid mechanics and its applications, 0925-0042*. Dordrecht and London: Springer, 2009.

[98] J. Bonet and R. D. Wood, *Nonlinear continuum mechanics for finite element analysis*. Cambridge University Press, 2008.

[99] J. C. Simo and T. J. Hughes, *Computational inelasticity*, vol. 7. Springer Science & Business Media, 1998.

[100] E. A. de Souza Neto, D. Peric, and D. R. Owen, *Computational methods for plasticity: theory and applications*. John Wiley & Sons, 2008.

[101] "Comsol multiphysics™ structural mechanics module User's Guide Version 4.2a."

[102] J. Clayton and J. Rencis, "Numerical integration in the axisymmetric finite element formulation," *Advances in Engineering Software*, vol. 31, no. 2, pp. 137 – 141, 2000.

[103] "Comsol multiphysics™ User's Guide Version 4.2a."

[104] K.-J. Bathe, E. Ramm, and E. L. Wilson, "Finite element formulations for large deformation dynamic analysis," *International Journal for Numerical Methods in Engineering*, vol. 9, no. 2, pp. 353–386, 1975.

[105] R. B. Farraro, R.and Mclellan, "Temperature dependence of the young's modulus and shear modulus of pure nickel, platinum, and molybdenum," *Metallurgical Transactions A*, vol. 8, no. 10, pp. 1563–1565, 1977.

[106] H. W. Kuhn and A. W. Tucker, "Nonlinear programming," in *Proceedings of the Second Berkeley Symposium on Mathematical Statistics and Probability*, pp. 481–492, University of California Press, 1951.

[107] R. v. Mises, "Mechanik der festen körper im plastisch-deformablen zustand," *Nachrichten von der Gesellschaft der Wissenschaften zu Göttingen, Mathematisch-Physikalische Klasse*, vol. 1913, pp. 582–592, 1913.

[108] W. Prager, "Recent developments in the mathematical theory of plasticity," *Journal of Applied Physics*, vol. 20, no. 3, pp. 235–241, 1949.

[109] M. L. Wilkins, "Calculation of elastic-plastic flow," tech. rep., California Univ Livermore Radiation Lab, 1963.

[110] J. Simo and R. Taylor, "A return mapping algorithm for plane stress elastoplasticity," *International Journal for Numerical Methods in Engineering*, vol. 22, no. 3, pp. 649–670, 1986.

[111] A. E. Green and P. M. Naghdi, "A general theory of an elastic-plastic continuum," *Archive for rational mechanics and analysis*, vol. 18, no. 4, pp. 251–281, 1965.

[112] P. Wriggers, *Nonlinear finite element methods*. Springer Science & Business Media, 2008.

[113] A. Srikanth and N. Zabaras, "A computational model for the finite element analysis of thermoplasticity coupled with ductile damage at finite strains," *International Journal for Numerical Methods in Engineering*, vol. 45, no. 11, pp. 1569–1605, 1999.

[114] A. G. Holzapfel, *Nonlinear solid mechanics II*. John Wiley & Sons, Inc., 2000.

[115] O. Zienkiewicz, R. Taylor, and J. Zhu, *The Finite Element Method: its Basis and Fundamentals (Seventh Edition)*. Oxford: Butterworth-Heinemann, seventh edition ed., 2013.

[116] T. Belytschko, W. K. Liu, B. Moran, and K. Elkhodary, *Nonlinear Finite Elements for Continua and Structures*. John Wiley & Sons, Incorporated, 2013.

[117] T. J. Hughes, *The finite element method: linear static and dynamic finite element analysis*. Courier Corporation, 2012.

[118] J. R. Shewchuk, "Triangle: Engineering a 2d quality mesh generator and delaunay triangulator," in *Workshop on Applied Computational Geometry*, pp. 203–222, Springer, 1996.

[119] I. Taig, *Structural analysis by the matrix displacement method*. English Electric Aviation Limited, 1962.

[120] E. Fonseca and P. Vila Real, "Finite element modelling of thermo-elastoplastic behaviour of hot-rolled steel profiles submitted to fire," in *IV Congresso de Métodos Numéricos en Ingeniería*, 1999.

[121] K.-J. Bathe and M. R. Khoshgoftaar, "Finite element formulation and solution of nonlinear heat transfer," *Nuclear Engineering and Design*, vol. 51, no. 3, pp. 389 – 401, 1979.

[122] G. Aguirre-Ramirez and T. J. Oden, "Finite element technique applied to heat conduction in solids with temperature dependent thermal conductivity," *International Journal for Numerical Methods in Engineering*, vol. 7, no. 3, pp. 345–355, 1973.

[123] V. P. Nguyen, "Finite elements for large deformation solid mechanics problems," 08 2008.

[124] J. N. Reddy, *An introduction to the finite element method*. McGraw-Hill New York, USA, 1993.

[125] A. Logg, K.-A. Mardal, and G. Wells, *Automated solution of differential equations by the finite element method: The FEniCS book*, vol. 84. Springer Science & Business Media, 2012.

[126] P. K. Kythe and M. R. Schäferkotter, *Handbook of computational methods for integration*. Chapman and Hall/CRC, 2004.

[127] V. Thomée, "From finite differences to finite elements: A short history of numerical analysis of partial differential equations," *Journal of Computational and Applied Mathematics*, vol. 128, no. 1, pp. 1 – 54, 2001.

[128] R. K. Brayton, F. G. Gustavson, and G. D. Hachtel, "A new efficient algorithm for solving differential-algebraic systems using implicit backward differentiation formulas," *Proceedings of the IEEE*, vol. 60, no. 1, pp. 98–108, 1972.

[129] J. Chung and G. Hulbert, "A time integration algorithm for structural dynamics with improved numerical dissipation: the generalized-α method," *Journal of Applied Mechanics*, vol. 60, no. 2, pp. 371–375, 1993.

[130] H. M. Hilber, T. J. Hughes, and R. L. Taylor, "Improved numerical dissipation for time integration algorithms in structural dynamics," *Earthquake Engineering & Structural Dynamics*, vol. 5, no. 3, pp. 283–292, 1977.

[131] C. Runge, "Über die numerische auflösung von differentialgleichungen," *Mathematische Annalen*, vol. 46, no. 2, pp. 167–178, 1895.

[132] W. Kutta, *Beitrag zur näherungweisen Integration totaler Differentialgleichungen*. 1901.

[133] J. Butcher and J. Sanz-Serna, "The number of conditions for a Runge-Kutta method to have effective order p," *Applied Numerical Mathematics*, vol. 22, no. 1-3, pp. 103–111, 1996.

[134] N. M. Newmark *et al.*, "A method of computation for structural dynamics," *Journal of the Engineering Mechanics Division*, vol. 85, no. 3, pp. 67–94, 1959.

[135] K. E. Jansen, C. H. Whiting, and G. M. Hulbert, "A generalized-α method for integrating the filtered Navier-Stokes equations with a stabilized finite element method," *Computer methods in applied mechanics and engineering*, vol. 190, no. 3-4, pp. 305–319, 2000.

[136] S. Erlicher, L. Bonaventura, and O. S. Bursi, "The analysis of the generalized-α method for non-linear dynamic problems," *Computational Mechanics*, vol. 28, no. 2, pp. 83–104, 2002.

[137] D. Kuhl and M. Crisfield, "Energy-conserving and decaying algorithms in non-linear structural dynamics," *International Journal for Numerical Methods in Engineering*, vol. 45, no. 5, pp. 569–599, 1999.

[138] G. M. Hulbert and I. Jang, "Automatic time step control algorithms for structural dynamics," *Computer Methods in Applied Mechanics and Engineering*, vol. 126, no. 1-2, pp. 155–178, 1995.

[139] A. Galántai, "The theory of Newton's method," *Journal of Computational and Applied Mathematics*, vol. 124, no. 1, pp. 25 – 44, 2000.

[140] W. H. Press, S. A. Teukolsky, W. T. Vetterling, and B. P. Flannery, *Numerical recipes in C*, vol. 1. 1988.

[141] "MUMPS (**MU**ltifrontal **M**assively **P**arallel sparse direct **Solver**)." `http://mumps.enseeiht.fr/`.

[142] "Comsol multiphysics™ Reference Guide Version 4.2a."

[143] "Solving Nonlinear Static Finite Element Problems." `https://www.comsol.de/blogs/solving-nonlinear-static-finite-element-problems`.

[144] J. Rang, "Adaptive timestep control for the generalised-α method," in *VI Conference on Adaptive Modeling and Simulations, ADMOS*, vol. 2013, 2013.

[145] G. Heise, M. Dickmann, J. Konrad, I. Richter, S. Sarrach, A. Heiss, H. Vogt, and H. P. Huber, "Application of induced laser ablation with ultra short pulse lasers for high speed thin film solar cell processing," *International Congress on Applications of Lasers & Electro-Optics*, vol. 2010, no. 1, pp. 1199–1205, 2010.

[146] E. I. Bromley, J. N. Randall, D. C. Flanders, and R. W. Mountain, "A technique for the determination of stress in thin films," *Journal of Vacuum Science & Technology B: Microelectronics Processing and Phenomena*, vol. 1, no. 4, pp. 1364–1366, 1983.

[147] C. W. Siders, A. Cavalleri, K. Sokolowski-Tinten, C. Toth, T. Guo, M. Kammler, M. Horn Von Hoegen, K. R. Wilson, D. Von Der Linde, and C. Barty, "Detection of nonthermal melting by ultrafast x-ray diffraction," *Science*, vol. 286, no. 5443, pp. 1340–1342, 1999.

[148] A. Barty, S. Boutet, M. J. Bogan, S. Hau-Riege, S. Marchesini, K. Sokolowski-Tinten, N. Stojanovic, R. Tobey, H. Ehrke, A. Cavalleri, S. Duesterer, M. Frank, S. Bajt, B. W. Woods, M. M. Seibert, J. Hajdu, R. Treusch, and H. N. Chapman, "Ultrafast single-shot diffraction imaging of nanoscale dynamics," *Nature Photonics*, vol. 2, no. 7, pp. 415–419, 2008.

[149] A. Rubenchik, M. Feit, M. Perry, and J. Larsen, "Numerical simulation of ultra-short laser pulse energy deposition and bulk transport for material processing1," *Applied Surface Science*, vol. 127, pp. 193–198, 1998.

[150] M. Perry, B. Stuart, P. Banks, M. Feit, V. Yanovsky, and A. Rubenchik, "Ultrashort-pulse laser machining of dielectric materials," *Journal of Applied Physics*, vol. 85, no. 9, pp. 6803–6810, 1999.

[151] S.-S. Wellershoff, *Untersuchungen zur Energierelaxationsdynamik in Metallen nach Anregung mit ultrakurzen Laserpulsen.* Dissertation, 2000.

[152] M. Domke, D. Felsl, S. Rapp, J. Sotrop, H. P. Huber, and M. Schmidt, "Evidence of pressure waves in confined laser ablation," *Journal of Laser Micro/Nanoengineering*, vol. 10, no. 2, pp. 119–123, 2015.

[153] B. C. Stuart, M. D. Feit, S. Herman, A. M. Rubenchik, B. W. Shore, and M. D. Perry, "Nanosecond-to-femtosecond laser-induced breakdown in dielectrics," *Physical Review B*, vol. 53, pp. 1749–1761, Jan 1996.

[154] L. V. Zhigilei, Z. Lin, and D. S. Ivanov, "Atomistic modeling of short pulse laser ablation of metals: connections between melting, spallation, and phase explosion," *The Journal of Physical Chemistry C*, vol. 113, no. 27, pp. 11892–11906, 2009.

[155] B. J. Demaske, V. V. Zhakhovsky, N. A. Inogamov, and I. I. Oleynik, "Ablation and spallation of gold films irradiated by ultrashort laser pulses," *Physical Review B*, vol. 82, no. 6, p. 064113, 2010.

[156] M. Domke, J. Sotrop, S. Rapp, M. Börger, D. Felsl, and H. P. Huber, "Transient temperature modeling and shock wave observation in confined laser ablation of thin molybdenum films," *Proc. of SPIE*, p. 86111B, 2013.

[157] A. Mermillod-Blondin, A. Rosenfeld, R. Stoian, and E. Audouard, "Formation dynamics of femtosecond laser-induced phase objects in transparent materials," *Proc. of SPIE*, vol. 8247, 2012.

[158] B. Rethfeld, "Unified model for the free-electron avalanche in laser-irradiated dielectrics," *Physical Review Letters*, vol. 92, no. 18, p. 187401, 2004.

[159] J. M. Liu, "Simple technique for measurements of pulsed gaussian-beam spot sizes," *Optics Letters*, vol. 7, no. 5, pp. 196–198, 1982.

[160] J. Sotrop, J. Winter, S. Rapp, and H. P. Huber, "Understanding laser ablation efficiency," *SPIE Newsroom*, 2015.

[161] M. Domke, S. Rapp, M. Schmidt, and H. P. Huber, "Ultrafast pump-probe microscopy with high temporal dynamic range," *Optics Express*, vol. 20, no. 9, pp. 10330–10338, 2012.

[162] R. Moser, D. Seiler, H. P. Huber, and G. Marowsky, "Observation of a spot diameter dependency in confined laser ablation of zinc oxide on copper-indium-diselenide," *Physics Procedia*, vol. 56, pp. 1034–1040, 2014.

[163] M. Domke, L. Nobile, S. Rapp, S. Eiselen, J. Sotrop, H. P. Huber, and M. Schmidt, "Understanding thin film laser ablation: The role of the effective penetration depth and the film thickness," *Physics Procedia*, vol. 56, pp. 1007–1014, 2014.

[164] P. Gečys, E. Markauskas, J. Dudutis, and G. Račiukaitis, "Interaction of ultra-short laser pulses with cigs and cztse thin films," *Applied Physics A Materials Science & Processing*, vol. 114, no. 1, pp. 231–241, 2014.

[165] N. Adamovic, A. Zimmermann, and W. Brenner, "The FP7 NMP project Solardesign: On-the-fly alterable Thin-film solar modules for design driven applications," *Conference Proceedings - 14th International Conference of the European Society for Precision Engineering and Nanotechnology*, vol. 1, pp. 55–58, 2014.

[166] E. T. Karim, M. Shugaev, C. Wu, Z. Lin, R. F. Hainsey, and L. V. Zhigilei, "Atomistic simulation study of short pulse laser interactions with a metal target under conditions of spatial confinement by a transparent overlayer," *Journal of Applied Physics*, vol. 115, no. 18, p. 183501, 2014.

[167] G. Heise, A. Börner, M. Dickmann, M. Englmaier, A. Heiss, M. Kemnitzer, J. Konrad, R. Moser, J. Palm, H. Vogt, and H. Huber, "Demonstration of the monolithic interconnection on cis solar cells by picosecond laser structuring on 30 by 30 cm2 modules," *Progress in Photovoltaics: Research and Applications*, vol. 23, no. 10, pp. 1291–1304, 2015.

[168] V. Probst, A. Jasenek, C. Sandfort, A. Letsch, I. Koetschau, T. Hahn, J. Feichtinger, and H. Eschrich, "Innovative front end processing for next generation CIS module production," *Japanese Journal of Applied Physics*, vol. 54, p. 08KC12, jul 2015.

[169] T. Peschel, S. Nolte, R. Eberhardt, and A. Tünnermann, "Simulation of laser structuring of thin-film solar cells," *Journal of Laser Micro Nanoengineering*, vol. 10, no. 3, pp. 284–290, 2015.

[170] S. Rapp, G. Heinrich, M. Wollgarten, H. P. Huber, and M. Schmidt, "Physical mechanisms of SiNx layer structuring with ultrafast lasers by direct and confined laser ablation," *Journal of Applied Physics*, vol. 117, p. 105304, mar 2015.

[171] W. Brenner and N. Adamovic, "Thin-film CIGS solar modules for design driven applications in the frame of the FP7 NMP project SolarDesign," in *2015 38th International Convention on Information and Communication Technology, Electronics and Microelectronics (MIPRO)*, IEEE, May 2015.

[172] H. W. Kang and A. J. Welch, "Enhanced coupling of optical energy during liquid-confined metal ablation," *Journal of Applied Physics*, vol. 118, p. 153101, oct 2015.

[173] M. Olbrich, E. Punzel, P. Lickschat, S. Weißmantel, and A. Horn, "Investigation on the ablation of thin metal films with femtosecond to picosecond-pulsed laser radiation," *Physics Procedia*, vol. 83, pp. 93–103, 2016.

[174] D. Scorticati, G. Römer, A. Huis in't Veld, and D. De Lange, "Modeling of temperature cycles induced by pico- and nanosecond laser pulses in zinc oxide and molybdenum thin films," *Journal of Heat Transfer*, vol. 138, no. 3, 2016.

[175] M. Olbrich, E. Punzel, R. Roesch, R. Oettking, B. Muhsin, H. Hoppe, and A. Horn, "Case study on the ultrafast laser ablation of thin aluminum films: dependence on laser parameters and film thickness," *Applied Physics A Materials Science & Processing*, vol. 122, no. 3, 2016.

[176] P. D. Gupta and G. M. O'Connor, "Comparison of ablation mechanisms at low fluence for ultrashort and short-pulse laser exposure of very thin molybdenum films on glass," *Applied Optics*, vol. 55, p. 2117, mar 2016.

[177] E. T. Karim, M. V. Shugaev, C. Wu, Z. Lin, H. Matsumoto, M. Conneran, J. Kleinert, R. F. Hainsey, and L. V. Zhigilei, "Experimental characterization and atomistic modeling of interfacial void formation and detachment in short pulse laser processing of metal surfaces covered by solid transparent overlayers," *Applied Physics A Materials Science & Processing*, vol. 122, mar 2016.

[178] M. Feinaeugle, D. J. Heath, B. Mills, J. A. Grant-Jacob, G. Z. Mashanovich, and R. W. Eason, "Laser-induced backward transfer of nanoimprinted polymer elements," *Applied Physics A Materials Science & Processing*, vol. 122, mar 2016.

[179] S. Rapp, M. Schmidt, and H. P. Huber, "Selective femtosecond laser structuring of dielectric thin films with different band gaps: a time-resolved study of ablation mechanisms," *Applied Physics A Materials Science & Processing*, vol. 122, nov 2016.

[180] S. Krause, P.-T. Miclea, G. Seifert, and C. Hagendorf, "Layer-selective lift-off processing in a tco/si thin film system by ultra-short (ps, fs) laser pulses," *Conference Record of the IEEE Photovoltaic Specialists Conference*, vol. 2016-November, pp. 3057–3061, 2016.

[181] E. Markauskas, P. Gečys, I. Repins, C. Beall, and G. Račiukaitis, "Laser lift-off scribing of the CZTSe thin-film solar cells at different pulse durations," *Solar Energy*, vol. 150, pp. 246–254, jul 2017.

[182] J. Winter, S. Rapp, M. Schmidt, and H. P. Huber, "Ultrafast laser processing of copper: A comparative study of experimental and simulated transient optical properties," *Applied Surface Science*, vol. 417, pp. 2–15, sep 2017.

[183] J. Winter, S. Rapp, M. Schmidt, and H. Huber, "Ultrafast laser energy deposition in copper revealed by simulation and experimental determination of optical properties with pump-probe ellipsometry," *Proc. of SPIE*, vol. 10091, 2017.

[184] F. S. Lim, X. Wang, K. A. Yaacob, A. K. Soh, and W. S. Chang, "Effect of indirect irradiation on surface morphology of au film by nanosecond laser," *Applied Physics A Materials Science & Processing*, vol. 123, sep 2017.

[185] L. Kotsedi, K. Kaviyarasu, X. Fuku, S. Eaton, E. Amara, F. Bireche, R. Ramponi, and M. Maaza, "Two temperature approach to femtosecond laser oxidation of molybdenum and morphological study," *Applied Surface Science*, vol. 421, pp. 213–219, nov 2017.

[186] M. Shugaev, M. He, S. Lizunov, Y. Levy, T.-Y. Derrien, V. Zhukov, N. Bulgakova, and L. Zhigilei, "Insights into laser-materials interaction through modeling on atomic and macroscopic scales," *Springer Series in Materials Science*, vol. 274, pp. 107–148, 2018.

[187] L. Pabst, F. Ullmann, R. Ebert, and H. Exner, "Selective rear side ablation of thin nickel–chromium-alloy films using ultrashort laser pulses," *Applied Physics A Materials Science & Processing*, vol. 124, feb 2018.

[188] S. Krause, P.-T. Miclea, G. Seifert, and C. Hagendorf, "Layer-selective lift-off processing in a tco/si thin film system by ultra-short (ps, fs) laser pulses," *2017 IEEE 44th Photovoltaic Specialist Conference, PVSC 2017*, pp. 1–5, 2018.

[189] K. Kiran Kumar, G. Samuel, and M. Shunmugam, "Theoretical and experimental investigations of ultra-short pulse laser interaction on ti6al4v alloy," *Journal of Materials Processing Technology*, vol. 263, pp. 266–275, 2019.

[190] H. S. Sim, S. H. Lee, and J. S. Lee, "Numerical analysis of crater formation and ablation depth in thin silicon films heated by ultrashort pulse train lasers," *Journal of Mechanical Science and Technology*, vol. 21, no. 11, pp. 1847–1854, 2007.

[191] A. Rämer, O. Osmani, and B. Rethfeld, "Laser damage in silicon: Energy absorption, relaxation, and transport," *Journal of Applied Physics*, vol. 116, no. 5, p. 53508, 2014.

[192] C. Duarte, O. Hamzeh, T. Liszka, and W. Tworzydlo, "A generalized finite element method for the simulation of three-dimensional dynamic crack propagation," *Computer Methods in Applied Mechanics and Engineering*, vol. 190, no. 15-17, pp. 2227–2262, 2001.

Acknowledgments

I would like to thank the Munich School of Engineering (MSE) at the Technical University of Munich for financial support in form of a scholarship in the framework of the 'TUM Applied Technology Forum', the European Commission for financial support within the Seventh Framework Programme project 'Solardesign', the German Research Foundation within the Project 'Modelling in Nanostructure Technology' and all the people there who made this possible.

I would like to express my thanks to all those who supported me during the period of my dissertation. I want particularly thank Prof. Dr. Paolo Lugli and Prof. Dr. Thomas Hamacher for their supervision, their trust, guidance through each stage of the process and for giving me the opportunity to create this thesis. Further thank to the chairman of the examination committee Prof. Dr. Michael Drews. For coordination and organizational support I want to thank Dr. Christiane Hamacher and the team at the MSE.

Special thanks to my mentor Prof. Dr. Alfred Kersch for inspiring my interest in simulation studies and for extraordinary fruitful discussions and sharing his expertise with me.

Thanks to the past and present members of the Lasercenter at the Munich University of Applied Sciences namely Prof. Dr. Heinz P. Huber, Dr. Gerhard Heise, Dr. Matthias Domke, Dr. Stephan Rapp, Regina Moser, Jan Winter and all coworkers and students for the numerous beneficial scientific and non-scientific discussions, their extraordinary experimental work and for supporting me.

Thanks to Dr. Jàn Minàr and Dr. Stephan Borek from the Faculty of Chemistry and Pharmacy at the Ludwig-Maximilians-University (LMU) for enriching FEM simulation with ab initio calculation.

Finally, I want to thank and dedicate this work to my family for supporting me during the time of my work.

Thank you!